

Transport coefficients in the hadronic medium

Dissertation

zur Erlangung des Doktorgrades
“Doctor philosophiae naturalis”
der Naturwissenschaften

vorgelegt beim Fachbereich 13 - Physik
der Johann Wolfgang Goethe - Universität
in Frankfurt am Main
von

Jean-Bernard Rose

aus Montreal

Frankfurt (2019)
(D 30)

Vom Fachbereich Physik der
Johann Wolfgang Goethe - Universität als Dissertation angenommen.

Dekan:

- Prof. Dr. Michael Lang
Physikalisches Institut

Gutachter:

- Prof. Dr. Hannah Elfner
Institut für theoretische Physik
- Prof. Dr. Marcus Bleicher
Institut für theoretische Physik

Datum der Disputation:

Contents

Zusammenfassung	i
1 Introduction	1
1.1 The field of heavy ion collisions	3
1.2 Transport coefficients in the hadron gas	7
1.2.1 Shear viscosity	7
1.2.2 Bulk viscosity	9
1.2.3 Cross-conductivity	10
1.2.4 Jet quenching parameters	11
1.3 Structure of the thesis	13
2 Theory of transport coefficients	14
2.1 The Green-Kubo formalism	15
2.1.1 Linear response theory	16
2.1.2 Cross-conductivity	19
2.1.3 Shear and bulk viscosity	21
2.2 The Chapman-Enskog formalism	27
2.2.1 Shear Viscosity	32
2.2.2 Bulk Viscosity	32
2.2.3 Cross-Conductivity	33
3 Modeling the hadron gas: SMASH	34
3.1 Collision criterion	34
3.2 Initialization	35
3.3 SMASH and the Boltzmann equation	37
3.4 Particle properties	41
3.4.1 Degrees of freedom	41
3.4.2 Resonance widths, lifetimes and decays	41
3.5 Scatterings	45
3.5.1 $2 \rightarrow 1$ processes	45
3.5.2 Elastic collisions	46
3.5.3 Inelastic $2 \rightarrow 2$ processes	46

3.5.4	Detailed balance	48
3.5.5	2-particle final state	48
3.5.6	Strings	49
3.5.7	Additive Quark Model	53
3.5.8	Transition region	54
3.6	Equilibrium and thermodynamics in SMASH	55
3.7	A note on versioning	58
4	Hadronic transport coefficients	59
4.1	Technical considerations and calibration of Green-Kubo calculations . .	59
4.2	Shear Viscosity	66
4.2.1	$\pi - \rho$ system	66
4.2.2	Full hadron gas	68
4.2.3	Discussion and comparison	70
4.3	Bulk Viscosity	78
4.3.1	Elastic pion gas	79
4.3.2	Full hadron gas	82
4.3.3	Discussion and comparison	85
4.4	Cross-conductivity	88
4.4.1	Simple systems	89
4.4.2	Exploring the parameter space	91
4.4.3	Electric conductivity theory comparison	95
5	Jets in the hadronic phase	98
5.1	Energy loss in the hadronic medium	99
5.2	Jet Shapes	104
6	Summary	108
	Bibliography	111
	Acknowledgements	131
	Curriculum Vitae	132

Zusammenfassung

Die Quantenchromodynamik (QCD) ist die Feldtheorie, die die starke Wechselwirkung von Materie beschreibt, wobei die fundamentalen Freiheitsgrade (oder äquivalent Felder) die fermionischen Quarks sind, die durch die bosonischen Gluonen interagieren. Interessanterweise und im Gegensatz zum Rest des Standardmodells enthält dieser Formalismus nichtlineare Beiträge, die wiederum die Quelle des Begriffs "Farbeinschluss" sind. Diese Eigenschaft ist eines der bestimmenden Merkmale von QCD. Insbesondere heißt es, dass es für freie Teilchen strikt unmöglich ist, eine Nettofarbladung zu haben. Dies ist der Grund, warum in der Außenwelt niemals einzelne Quarks oder Gluonen beobachtet werden: Sie existieren alle in gebundenen Zuständen innerhalb der stabileren und Farb-neutralen Hadronen wie Protonen, Neutronen oder Pionen. Man kann Baryonen unterscheiden, die sich aus drei Valenzquarks mit einer Nettofarbladung von Null zusammensetzen (z. B. besteht ein Neutron aus einem Up-Quark mit einer elektrischen Ladung $+2/3$ und zwei Down-Quarks mit jeweils einer elektrischen Ladung $-1/3$; dies wird manchmal als udd geschrieben) und Mesonen, die gebundene Zustände von Quarks und Anti-Quarks mit entgegengesetzten Farbladungen sind (z. B. $u\bar{d}$, wenn positiv, $\bar{u}d$, wenn negativ, oder eine Überlagerung von beiden, wenn neutral, $(u\bar{d} + \bar{u}d)/\sqrt{2}$).

In dieser Arbeit interessieren wir uns für das Verhalten von Bulk-Fermionen oder "QCD-Materie". Das Farbeinschluss-Phänomen ist, wie bereits erwähnt, ein Niedrigenergie-Phänomen. Bei hohen Energiedichten sagt QCD aufgrund der starken Kopplung ein Deconfinement der Farbladung voraus, was das Vorhandensein mehrerer Phasen der QCD-Materie impliziert. Bei sehr hoher Energie (d. h. bei hohen Temperaturen oder Dichten) wird erwartet, dass QCD-Materie aus einem Gas von Quarks und Gluonen besteht; diese thermodynamische Phase der Materie wird als Quark-Gluon-Plasma (QGP) bezeichnet. Bei niedrigeren Energien unterhalb der Farbeinschlusschwelle sollte die jetzt aus Hadronen zusammengesetzte QCD-Materie als ein Gas von Hadronen (auch als Hadronenresonanzgas bekannt) wirken. Obwohl dies nicht das Hauptthema dieser Arbeit sein wird, wird daher erwartet, dass irgendwann ein Phasenübergang bei einer kritischen Temperatur zwischen dem QGP und dem Hadronenresonanzgas stattfindet. Die Schwierigkeiten, die bei der Lösung von QCD aufgrund der Gluon-Selbstwechselwirkungen auftreten, machten es erforderlich, eine

Reihe effektiver Modelle zu entwickeln, die genaue Beschreibungen der QCD-Materie in bestimmten Anwendungsbereichen liefern können.

Es wird angenommen, dass sogenannte Transportmodelle, die sich mit statistischen Ensembles von Partikeln und ihren Wechselwirkungen untereinander befassen, eine gute Beschreibung der QCD-Materie liefern, insbesondere in der Hadronengasphase, die den Schwerpunkt dieser Arbeit bildet. In einem System, in dem sich Teilchen einer Spezies i mit Verteilungsfunktion f_i ausbreiten und interagieren, liefern Transportansätze Lösungen für die relativistische Boltzmann-Gleichung, auf der sie basieren:

$$p^\mu \frac{\partial f_i}{\partial x^\mu} + m_i \frac{\partial(\mathcal{F}^\mu f_i)}{\partial p^\mu} = \sum_j^N C[f_i, f_j], \quad (1)$$

wobei \mathcal{F}^μ eine externe Kraft und $C[f_i, f_j]$ der Kollisionsterm ist, der die Wechselwirkungen mit einer anderen Teilchenart (oder möglicherweise mit sich selbst) einschließt; für ein System mit N Freiheitsgraden erhält man dann entsprechend N solcher Gleichungen. Dieses große Gleichungssystem wird dann mithilfe von Monte-Carlo-Simulationen gelöst, bei denen sich Teilchen gemäß der linken Seite der Gleichungen ausbreiten und über die Wirkungsquerschnitte interagieren, die im Kollisionsintegrale auf der rechten Seite eine Rolle spielen. Diese Methode kann im Prinzip für eine beliebige Anzahl von Freiheitsgraden angewendet werden, sei es partonisch oder hadronisch, solange die zuvor genannten Bedingungen erfüllt sind. Transportansätze haben den Vorteil, dass das System nicht im Gleichgewicht sein muss. Andererseits bedeutet die exponentielle Kombinatorik der Erhöhung der Anzahl der Freiheitsgrade, dass sehr große Mengen phänomenologischer Daten erforderlich sind, um sinnvolle Ergebnisse zu erzielen. Schwerionenkollisionen bei niedrigen Strahlenergien, bei denen die Erzeugung eines Quark-Gluon-Plasmas unwahrscheinlich ist, können durch ein solches Modell ebenfalls angemessen beschrieben werden.

Insbesondere verwenden wir in dieser Arbeit das hadronische Transportmodell SMASH (Simulating Many Accelerated Strongly-interacting Hadrons). Die Hauptmerkmale des Modells werden erläutert, z. B. das Kollisionskriterium, die berücksichtigten Freiheitsgrade und die spezifische Art und Weise, in der die Teilchen mikroskopisch miteinander interagieren. Es wurde nachgewiesen, dass SMASH die Ergebnisse der Boltzmann-Gleichung in einem expandierenden Universums reproduziert und somit die Äquivalenz dieses Transportmodelles und der damit verbundenen kinetischen Theorie-Ergebnisse zeigt. Besonderes Augenmerk wird darauf gelegt, wie mit SMASH ein thermischer und chemischer Gleichgewichtszustand erreicht und beschrieben werden kann, der für die Gültigkeit unserer weiteren Berechnungen erforderlich ist.

Das Hauptziel dieser Arbeit sind sogenannte lineare Antwort-Transportkoeffizienten, die die Relaxation einer Störung in einem gegebenen System beschreiben. Diese makroskopischen Größen kodieren die mikroskopische QCD-Physik wie die Wech-

selwirkungsstärke von Bestandteilen und ihre relativen Häufigkeiten und Ladungen vollständig und eignen sich hervorragend zur Charakterisierung des Mediums. Typischerweise können sie so ausgedrückt werden, dass

$$\mathbf{J}_k = \nu_k \mathbf{X}_k, \quad (2)$$

wobei \mathbf{J}_k ein Fluss ist, der mit einer Eigenschaft k zusammenhängt, ν_k der Transportkoeffizient ist und \mathbf{X}_k ein Gradient ist, der auf die Eigenschaft k einwirkt. Die Untersuchung dieser Transportkoeffizienten der heißen und dichten Kernmaterie ist eines der Hauptziele der Schwerionenphysik, da sie die Nichtgleichgewichtsentwicklung des expandierenden Feuerballs steuern. Daher haben sich viele Anstrengungen auf diesem Gebiet auf die Einschränkung ihrer möglichen Werte konzentriert, um sowohl QCD-Materie zu charakterisieren als auch robuste Inputs für ein weiteres erfolgreiches effektives Modell, das der Hydrodynamik, zu liefern. Insbesondere konzentrieren wir uns auf das Niedrigenergieregime, das dem Hadrongas entspricht, da die Eigenschaften dieses Bereichs des Phasendiagramms noch relativ unbekannt sind und die vorhandenen Berechnungen für die Transportkoeffizienten entweder knapp, widersprüchlich oder in gewissen Umfang begrenzt sind. Das Hauptziel dieser Arbeit ist es daher, dies durch neue unabhängige Berechnungen dieser Größen zu beleuchten.

Um die Transportkoeffizienten zu berechnen, untersuchen wir im Detail den bekannten Green-Kubo-Formalismus, der Selbstkorrelationen dissipativer Fluktuationen mit den Transportkoeffizienten in Beziehung setzt. Dieser Formalismus ist sowohl hinsichtlich der theoretischen Grundlagen sehr robust als auch hinsichtlich der Rechenanforderungen relativ vernünftig, selbst für hochkomplexe Systeme mit vielen Freiheitsgraden. Daher wird dieser Formalismus verwendet, um die meisten der in dieser Arbeit vorgestellten Ergebnisse zu liefern. Parallel diskutieren wir auch den Chapman-Enskog-Formalismus, der darauf abzielt, die Boltzmann-Gleichung zu linearisieren, um semianalytische Schätzungen der verschiedenen Transportkoeffizienten zu erhalten. Obwohl diese Methode im Prinzip eine der einfachsten und genauesten Methoden zur Berechnung dieser Koeffizienten ist, steigen die Komplexität und die Anforderungen an die Berechnung mit zunehmendem Schwierigkeitsgrades der Systeme exponentiell an, so dass es in der Regel nicht praktikabel ist, sie für mehr als relativ einfache Systeme zu verwenden (d. h. mit sehr wenigen Teilchen-Arten und Resonanzen). Die Tatsache, dass man ein halbanalytisches Ergebnis erhält, macht es jedoch zu einem guten Vergleichs- und Kalibrierungswerkzeug für die Abschätzung des systematischen Fehlers des Green-Kubo-Formalismus.

Die Hauptergebnisse dieser Arbeit sind die Berechnung von drei Transportkoeffizienten, nämlich der Scherviskosität η , der Volumenviskosität ζ und der neu definierten Querleitfähigkeit ($\sigma^{QQ}, \sigma^{QB}, \sigma^{QS}$); letzteres ist eine Kombination aus der bekannten elektrischen Leitfähigkeit und zwei neuen Leitfähigkeiten, insbesondere der baryonisch-

elektrischen und der seltsam-elektrischen, die Kreuzwirkungen zwischen verschiedenen Arten von Elementarladungen quantifizieren. Die endgültigen Ausdrücke, die aus dem Green-Kubo-Formalismus für die Scherviskosität, die Volumenviskosität und die Querleitfähigkeit erhalten werden, sind gegeben durch

$$\begin{aligned}\eta &= \frac{V}{T} \int_0^\infty dt' \langle \pi^{xy}(0), \pi^{xy}(t') \rangle_l, \\ \zeta &= \frac{V}{T} \int_0^\infty dt' \langle p(0), p(t') \rangle_l, \\ \sigma_{QQ, QB, QS} &= \frac{V}{T} \int_0^\infty \langle j_{Q,B,S}^x(0), j_x^Q(t') \rangle_l dt',\end{aligned}\tag{3}$$

wobei

$$\langle A(t), B(t') \rangle_l \equiv \langle (A(t) - \langle A \rangle_l)(B(t') - \langle B \rangle_l) \rangle_l,\tag{4}$$

V und T sind das Volumen und die Temperatur des Systems, π^{xy} ist eine nicht diagonale Komponente des Scherspannungstensors (der dem gleichen Element des Energieimpulstensors im Ruhezustand entspricht), p ist der Druck des Systems, wie durch die Spur des räumlichen Teils des Energie-Impuls-Tensors gegeben, und $j_{Q,B,S}^x$ ist eine Komponente entweder des elektrischen, baryonischen oder seltsamen Teilchenstroms. Der Einfachheit halber definieren wir die Autokorrelations- (oder einfach nur Korrelations-) Funktionen $C^{xy} \equiv \langle \pi^{xy}(0), \pi^{xy}(t) \rangle_l$, $C^\Pi \equiv \langle p(0), p(t) \rangle_l$ und $C_j^{QQ, QB, QS} \equiv \langle j_{Q,B,S}^x(0), j_x^Q(t) \rangle_l$. Es ist zu beachten, dass diese Formeln erfordern, dass sich das System in einem Gleichgewichtszustand befindet, um anwendbar zu sein, da die Temperatur und die gemittelten Schwankungen über lange Zeiträume definiert und konstant sein müssen.

Wie man aus Gl. (3) erkennt, erfordert die Berechnung der Transportkoeffizienten die Integration der verschiedenen Korrelations-Funktionen von Null bis Unendlich, was numerisch ziemlich schwierig ist, da der relative Fehler einer numerischen Berechnung der Korrelationsfunktion für jede Zeit t notwendigerweise ziemlich schnell zunimmt und schließlich einen Zustand reines Rauschens erreicht. Um diese Einschränkung zu umgehen, wird eine gewisse Annahme über die analytische Form der Korrelationsfunktion getroffen. Es wird allgemein angenommen, dass es sich bei verdünnten Systemen um ein abklingendes Exponential handelt, beispielsweise bei der Scherviskosität,

$$C^{xy}(t) = C^{xy}(0) e^{-\frac{t}{\tau}},\tag{5}$$

dabei ist τ die Relaxationszeit des Systems. Es folgt dass

$$\eta = \frac{C^{xy}(0)V\tau}{T},\tag{6}$$

und ähnlich für die anderen Transportkoeffizienten. Man sollte beachten, dass die

Verwendung dieses Ansatzes und die Charakterisierung des Gleichgewichts, in dem sich das System befindet, einige systematische Unsicherheiten mit sich bringen, die in dieser Arbeit diskutiert werden.

Nach vollständigen systematischen Untersuchungen werden die Scherviskosität η , die Volumenviskosität ζ und die Querleitfähigkeiten ($\sigma^{QQ}, \sigma^{QB}, \sigma^{QS}$) im Vergleich zu früheren Berechnungen berechnet und Anmerkungen zu den Eigenschaften der Transportkoeffizienten und deren Abhängigkeiten gemacht. Es wird gezeigt, dass die detaillierte mikroskopische Art und Weise, wie Wechselwirkungen zwischen Teilchen in verschiedenen Modellen durchgeführt werden, einen großen Einfluss auf einige Koeffizienten haben kann. Insbesondere erscheint die Implementierung von Resonanzlebensdauern für die geeignete Behandlung der Scherviskosität sehr relevant, während wir sehen, dass die Volumenviskosität Massenänderungsprozesse (beispielsweise durch Ausbreitung von Resonanzen, aber nicht darauf beschränkt) erfordert, um vollständig konsistent zu sein. Interessanterweise zeigen die Leitfähigkeiten eine viel geringere Empfindlichkeit gegenüber der Behandlung von Resonanzen; es wird gezeigt, dass die Erhöhung der Anzahl der Freiheitsgrade zu Unterschieden in der Temperaturabhängigkeit der Leitfähigkeiten führt, sodass zukünftige Berechnungen dieser Größen auf dem Gitter dazu beitragen könnten, einige Eigenschaften von Hadronentransportansätzen einzuschränken.

In unserem letzten Kapitel nähern wir uns der Beschreibung der Hadronengaseigenschaften mit einem etwas anderen Ansatz, indem wir Teilchen mit hohem Impuls p_T durch ein Hadronengas schießen, um zum ersten Mal ein hadronisches Äquivalent zu den Parametern des Jet Quenchings \hat{q} und \hat{e} zu berechnen. Diese hadronischen Transportkoeffizienten werden als \tilde{q} und \tilde{e} bezeichnet, und ihr Wert wird berechnet auf ungefähr drei- bis viermal kleiner als der ihrer QGP-Gegenstücke. Während die Auswirkungen auf die beobachtbaren Jet-Effekte hieraus geringer sein sollten, ist dies keineswegs vernachlässigbar. Dies zeigen wir anhand der Winkelverteilung des Impulses (oder der Jet-Form) eines Teilchens mit hohem p_T , das durch eine expandierende Kugel fliegt. Wir weisen abschließend darauf hin, dass es zwar einen heuristischen Zusammenhang zwischen der Scherviskosität η und dem Querparameter \hat{q} im QGP gibt, dies jedoch bei den niedrigeren Temperaturen, die dem Hadronengas entsprechen, anscheinend nicht der Fall ist.

In dieser Arbeit wird gezeigt, dass die makroskopischen Transportkoeffizienten sehr empfindlich auf die spezifische mikroskopische Art in der Wechselwirkungen zwischen Teilchen modelliert werden, reagieren. Um dies umzukehren, können genauere Werte dieser Koeffizienten aus experimentellen Daten extrahiert werden und dann auch verwendet werden, um dieser Modellierung einige Einschränkungen aufzuerlegen.

Chapter 1

Introduction

The Standard Model is generally accepted to be the fundamental theory upon which most of particle physics can be constructed. Indeed, it has so far managed to incorporate three of the four known fundamental interactions, namely the electromagnetic, weak and strong interactions, while the gravitational interaction does remain separate. The electromagnetic and weak interactions have been combined in the so-called quantum electroweak theory, and the strong interaction, modeled using Quantum Chromodynamics (QCD), is added to the previous two [1].

Of those three field theories, QCD, which will be the main focus of this thesis, is without a doubt the one whose solution has proven to be the most elusive¹. In this theory of strong interactions, the fundamental degrees of freedom (or, equivalently, fields) are the fermionic quarks ψ , which interact through the bosonic gluons A_a . In such relativistic field theories, all the features of a given model are encapsulated in the Lagrangian density \mathcal{L} , which includes contributions from the kinetic part of the system (e.g. the propagation of fields) and from its potential parts (e.g. their mass, interaction with other fields, etc.). In the case of QCD it takes the form

$$\mathcal{L}_{QCD} = \sum_{\psi} \bar{\psi}_i \left(i\gamma^{\mu} (\partial_{\mu} \delta_{ij} - \frac{i}{2} g_s A_{\mu}^a \lambda_{ij}^a) - m_{\psi} \delta_{ij} \right) \psi_j - \frac{1}{4} G_{\mu\nu}^a G_a^{\mu\nu}, \quad (1.1)$$

$$G_a^{\mu\nu} = \partial_{\mu} A_{\nu}^a - \partial_{\nu} A_{\mu}^a + f^{abc} A_b^{\mu} A_c^{\nu}, \quad (1.2)$$

where γ^{μ} are Dirac matrices, g_s is the strong coupling constant, λ_{ij}^a are the Gell-Mann matrices (i.e. the generators of the SU(3) symmetry group), m_{ψ} is the mass of a quark and f^{abc} are the structure constants of SU(3). The sum over ψ goes over all the known existing quarks (and antiquarks), which currently number to six; by increasing mass, these are known as the up, down, strange, charm, bottom and top. Both quarks and gluons also carry a color charge. Quarks carry a single color charge,

¹Although this is a completely unbiased statement by the author of these lines, one could be forgiven to think other fields related to the Standard model also to be deserving of this prized distinction.

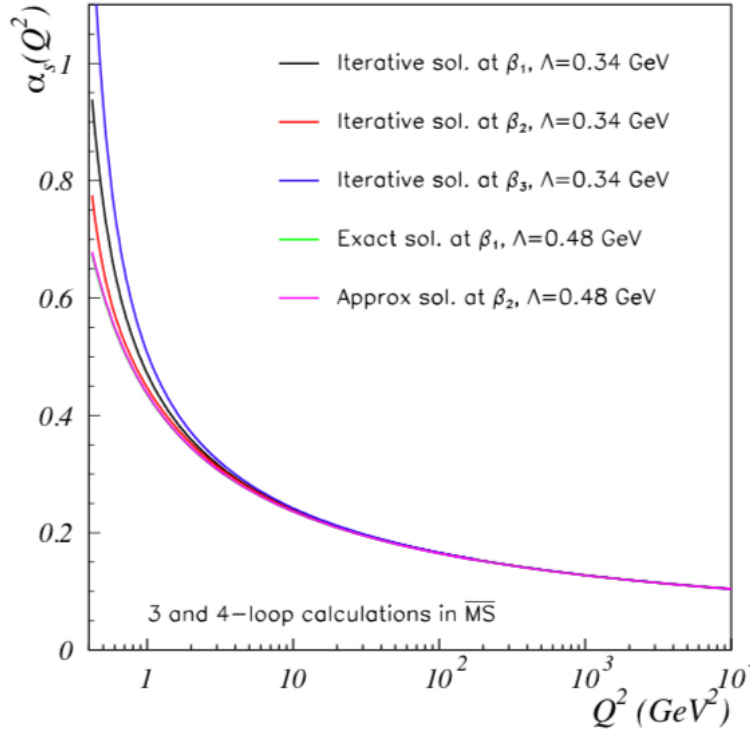


Figure 1.1: Running coupling constant of QCD α_s as a function of the energy scale Q^2 , according to various calculation methods; Λ is the QCD scale parameter which can be understood as a characteristic length. Taken from [2].

which will then be called blue, green or red; similarly, antiquarks carry a charge which will be either anti-blue, anti-green or anti-red. Gluons carry compositions of colors and anti-colors, for a total of eight possible combinations, which are summed over in the previous equation over the latin indices (note that the fermionic color charge was implicitly summed in the latin index of the Gell-Mann matrices). Some terms of this Lagrangian also correspond to the various interactions which are possible within QCD; the second term in the parenthesis for example corresponds to the quark-antiquark annihilation which produces a gluon. Interestingly and in contrast with the electroweak sector of the Standard Model, the last term of the Lagrangian contains additional contributions from the structure constants which lead to purely gluonic interactions (namely the 3-gluon and 4-gluon vertices). This self interaction between the bosons makes the treatment of the strong interaction non-linear and leads to a running of the strong coupling constant which asymptotically tends towards zero at large energies, but diverges at lower temperatures (see Fig. 1.1), and is thus the source of the phenomenon called color confinement.

This color confinement is one of the defining characteristics of QCD, as it shapes the low energy world we live in; specifically, it states that it is strictly impossible for free-streaming particles to have a net color charge at the energies the universe currently features. It is the reason why no lone quarks or gluons are ever observed

in the outside world: they all exist in confined states within the more stable and color neutral hadrons such as the proton, neutron or pion. Thus can one distinguish baryons, which are composed of three valence quarks with a zero net total color charge (e.g. a neutron is made of an up quark with electric charge $+2/3$ and two down quarks each with electric charge $-1/3$; this is sometimes written as udd), and mesons, which are bound states of quarks and anti-quarks with opposite color charges (e.g. pions are then $u\bar{d}$ if positive, $\bar{u}d$ if negative or a superposition of both if neutral $(u\bar{d} + \bar{u}d)/\sqrt{2}$).

1.1 The field of heavy ion collisions

In this work we will be most interested in the behavior of bulk fermions, or “QCD matter.” The confinement phenomenon is, as stated earlier, a low energy phenomenon; at high energy densities, QCD predicts a deconfinement of the color charge due to the weakening of the strong coupling, which then implies the existence of multiple phases of the QCD matter, which are shown on Fig. 1.2. At very high energy (i.e. at large temperatures or densities), it is supposed that QCD matter should consist of a gas of quarks and gluons; this thermodynamic phase of matter is called the quark-gluon plasma (QGP). At lower energies, below the color confinement threshold, similarly, the QCD matter, now composed of hadrons, should act as a gas of hadrons (also known as the hadron resonance gas). Although it will not be the main topic of this thesis, it is thus expected that at some point, a phase transition should occur between the quark-gluon plasma and the hadron resonance gas; this transition is generally thought to be a crossover at zero baryon chemical potential μ_B , and a first order phase transition at some unknown larger μ_B , which means a critical point should exist somewhere in between the two [3].

In order to observe both of these phases and their interplay, one must first be able to generate extremely high temperatures and pressures in a controlled environment², which is one of the goals that motivated the development and construction of several modern day particle accelerators. Up to now, only two accelerators exist which have been proven to be able to reach the energies required for the presence of the QGP: the Relativistic Heavy Ion Collider (RHIC) at the Brookhaven National Laboratory and the Large Hadron Collider (LHC) in Geneva, while several others still manage to reach the energies required for the creation of a hadron gas. Many observations which first came out of RHIC [5–8] and were later confirmed by the LHC [9–11] were at first surprising, as it was realized that the QGP produced at these experimental facilities was not in fact weakly but rather strongly coupled [12, 13]; this picture is

²The temperature conversion factor from mega electron-Volt (MeV) to Kelvin (K) is $1 \text{ MeV} = 11,600,000 \text{ K}$. This means that using these more common units, the temperatures discussed in this thesis ($\sim 75 - 175 \text{ MeV}$) are typically of the order of 1-2 billion K; as a comparison for the reader, the surface of the sun is at relatively frisky 5778K.

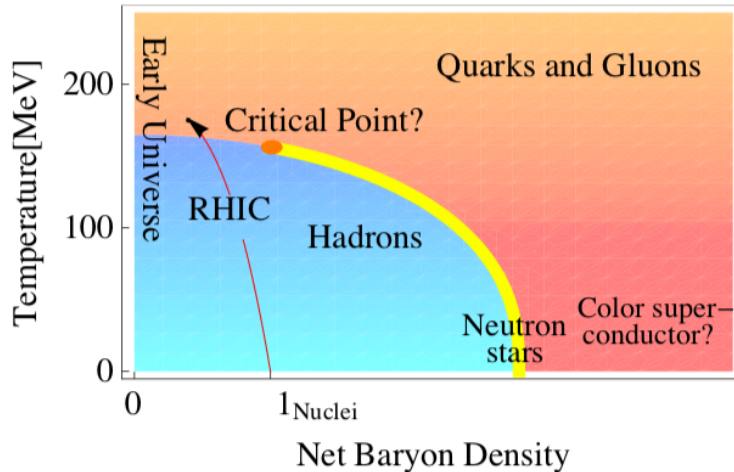


Figure 1.2: Phase diagram of QCD; the QGP is in the top right part, in orange, and the hadron gas in blue in the bottom left. Also indicated are approximate locations for a possible critical point between crossover and first order phase transitions, as well ultra-dense neutron stars or the state the early universe was in shortly after the Big Bang. Taken from [4].

thus more consistent with a fluid description, indicating that although the running coupling constant decreases as the energy increases (see Fig. 1.1), the density of this phase of matter is still sufficiently high for it not to behave as a gas of almost free streaming quasi-particles. Due to this strong non-linearity of the underlying theory of QCD and large coupling constant at the energies which are currently reachable through experiment, the field of heavy ion physics has thus seen a flourishing of so-called effective models whose validity regime extend on one or the other side (and sometimes both, in a limited fashion) of the phase transition. The rest of this section is dedicated to highlighting some features of prominent models; note that this list is in no way exhaustive.

Closest to QCD in spirit as well as in form exist a plethora of effective field theories, in which a Lagrangian formalism similar to the fundamental theory is used, but modified in such a way as to make them calculable in some (usually quite energetic, but not always) regime. The most prominent member of this family of models is undoubtedly lattice QCD, where a discretization of space and time allow for the computation of some quantities (most prominently the equation of state) in the region $\mu_B/T \leq 2$ [14–16]; in the continuum limit, time and space granularity should converge to the actual QCD result. Lattice QCD is thus in principle the most fundamental “easily” computable expression of QCD, but it faces technical obstacles which are almost as complicated as regular QCD calculations, especially in terms of computing power; to surmount them, unphysical quark masses and other simplifying assumptions are often made. Other notable field theory contributions are:

1. The Dyson-Schwinger formalism [17], in which propagators are modified in a spe-

cific way to produce valid results at any energy, provided one can appropriately truncate an infinite system of equations,

2. Chiral effective theories [18], in which hadrons rather than quarks and gluons are the degrees of freedom, the large number of which make precise calculation complicated,
3. The Color Glass Condensate (or CGC) formalism [19], in which a separation of energy scales allows to impose a saturation scale on cross-sections; this allows to approximate nucleons as gluon balls enveloping highly energetic quarks, which is valid at very early times after a heavy ion collision,
4. The Anti-de Sitter/Conformal Field Theory correspondence, or holography [20], in which similarities between the weakly coupled 5-dimensional supergravity and conformal strongly coupled quantum field theories are exploited; aside from the fact that this duality remains a conjecture, difficulties usually arise when remembering that QCD only *approaches* conformality at the very highest energies.

Another very successful effective model is that of relativistic hydrodynamics, one of whose strengths is its ability to correctly reproduce the observed large final state anisotropic momentum distributions (or “flow”) [21]. In essence, hydrodynamics is nothing but the application of conservation laws to a system which is assumed to be locally in equilibrium; in the relativistic case, the energy-momentum tensor $T^{\mu\nu}$ and the particle 4-current N^μ are thus conserved, such that $\partial_\mu T^{\mu\nu} = 0$ and $\partial_\mu N^\mu = 0$. Closing the system of equations additionally requires one to define an equation of state relating the pressure to the energy density and particle current, which then encapsulates all the microscopic interactions. Hydrodynamics is traditionally considered valid provided that the individual equilibrated parts of the system system are large enough, i.e. if the Knudsen number $\text{Kn} = \frac{\lambda_{mfp}}{L} \ll 1$ [22], where λ_{mfp} is the mean free path of particles in a cell of size L in the fluid³ (typically this should then happen at large temperatures, although it is not restricted to the sole QGP phase; high temperature hadronic gases are also generally thought to be dense enough to be treated with this formalism). Since hydrodynamic descriptions deal with energy-momentum and particle current tensors rather than directly with the underlying degrees of freedom, it must be initialized according to some prescription which needs to come from another initial condition model (for example the Glauber model for energy deposition [34, 35], or various implementations of the previously discussed CGC formalism [36–39]), as well as

³Some recent observations of collective phenomena which are usually associated with hydrodynamic behavior in small systems (i.e. proton-nucleus or even proton-proton collisions) at the LHC [23–25], along with the apparent ability of hydrodynamics to reproduce such results [26–30], have caused many in the field to question whether this applicability range should be extended; some theoretical expansions, notably through the concepts of hydrodynamic attractors [31, 32] and cavitation [33], have tried to bridge that gap.

reconverted into particles (a process known as “particlization”) at some phenomenologically determined fixed temperature or energy density through the Cooper-Frye formula [22, 40–42]. As such, hydrodynamic models are most often the central part of so-called hybrid models of heavy ion collisions, which are then composed of an initial conditions model, the hydrodynamic evolution of the high temperature sector of the produced medium, the Cooper-Frye particlization and a hadronic afterburner.

These afterburners refer to the last category of models which we will mention and which are used throughout the bulk of this thesis: transport approaches, which deal with statistical ensembles of particles and their interactions with each other [43]. In a system in which particles of a species i with distribution function f_i propagate and interact, transport approaches generally assume the following:

1. The system is dilute enough that only binary collisions are relevant, i.e. in any sub-region of space of the order of the collision range, there are never more than two particles. Those binary collisions can be elastic as well as inelastic.
2. The mean free path λ_{mfp} is much longer than the collision time; in other words, the interaction range is assumed to be short. This could be violated for example if a long-ranged Coulomb potential between particles was considered.
3. The incoming and outgoing particles of a binary collision are uncorrelated, that is, in terms of distribution functions,

$$f(t, \mathbf{x}_1, \mathbf{p}_1, \mathbf{x}_2, \mathbf{p}_2) \simeq f(t, \mathbf{x}_1, \mathbf{p}_1)f(t, \mathbf{x}_2, \mathbf{p}_2), \quad (1.3)$$

where \mathbf{x} and \mathbf{p} are the position and momenta of the interacting particles. This is known as the molecular chaos hypothesis.

These conditions are generally known as Boltzmann’s *Stosszahlansatz*, and are required for the relativistic Boltzmann equation upon which transport approaches are based (here written in a covariant form):

$$p^\mu \frac{\partial f_i}{\partial x^\mu} + m_i \frac{\partial(\mathcal{F}^\mu f_i)}{\partial p^\mu} = \sum_j^N C[f_i, f_j], \quad (1.4)$$

where \mathcal{F}^μ is an external force and $C[f_i, f_j]$ is the collision term which encapsulates the interactions with another particle species (or possibly itself); for a system containing N degrees of freedom, one then correspondingly obtains N such equations. This large system of equations is then solved using Monte Carlo simulations where particles propagate according to the left-hand side of the equations and interact via the cross-sections involved in the writing of the collision integrals on the right-hand side. This method can in principle be applied for any number of degrees of freedom,

be they partonic or hadronic, as long as the previously mentioned conditions are fulfilled. Transport approaches have the advantage of not requiring the system to be in equilibrium, in contrast with hydrodynamics which require at least local equilibrium over large enough regions; combined with the fact that these two approaches are valid in different energy regimes, this makes them complementary in many ways, hence the prevalence of the previously mentioned hybrid models. On the other hand, the exponential combinatorics of increasing the number of degrees of freedom means very large amounts of phenomenological data is needed to obtain sensible results. Heavy ion collisions at low beam energies, where the production of a quark-gluon plasma is unlikely, can also be appropriately described by such a model. Notable transport approaches include UrQMD [44], GiBUU [45], PHSD [46], BAMPS [47], B3D [226] and finally the one which will be used in this thesis, SMASH [48], which will be extensively discussed in Chapter 3.

1.2 Transport coefficients in the hadron gas

In this thesis we will focus our efforts on the region of applicability of SMASH, that is, the hadron resonance gas at temperatures around and below the phase transition. Specifically, we will be interested in calculating so-called linear response transport coefficients, which describe the relaxation of a perturbation in a given system. Those macroscopic quantities fully encode the microscopic QCD physics such as the interaction strength of constituents and their relative abundances and charges, making excellent tools for the characterization of the medium; typically, they can be expressed such that

$$\mathbf{J}_k = \nu_k \mathbf{X}_k, \quad (1.5)$$

where \mathbf{J}_k is some flux related to a property k , ν_k is the transport coefficient and \mathbf{X}_k is a gradient acting on the property k ; several ways of calculating transport coefficients will be detailed in Chapter 2. Studying these transport coefficients of the hot and dense nuclear matter is one of the main goals of the field heavy-ion collisions, as they control the non-equilibrium evolution of the expanding fireball, and as such many efforts in the field have been concentrated on constraining their possible values, both to characterize QCD matter and to provide robust inputs for hydrodynamical models. In the following, the various coefficients which will be calculated in this thesis and the specific reasons they are of interest will be introduced.

1.2.1 Shear viscosity

One of the most well-studied dissipative coefficients is the shear viscosity η and its associated dimensionless ratio with the entropy density η/s , which measure the ability

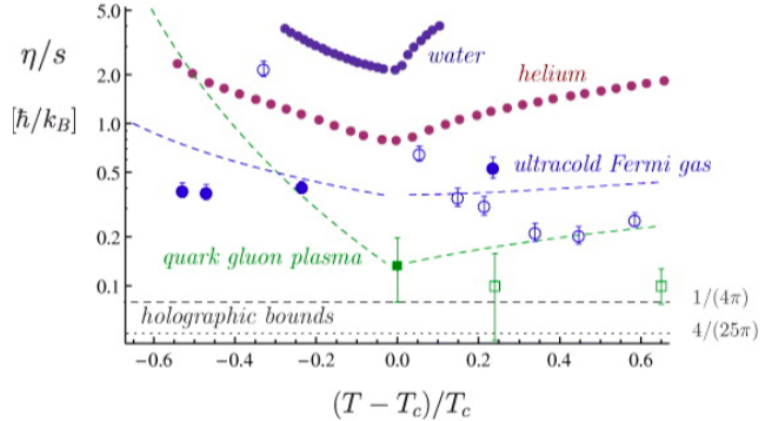


Figure 1.3: Shear viscosity to entropy density ratio vs temperature around the critical temperature T_c , for various everyday substances and QCD matter. Taken from [65].

of the fluid system to relax towards equilibrium after a shear perturbation [43, 49]. The interest in shear viscosity surged in the field of heavy ion collisions as measurements of large anisotropies in the final momentum distributions (or “flow”) were made at RHIC in the early 2000s, which was then shown to be in very good agreement with hydrodynamics. Specifically, although ideal hydrodynamics manage to reproduce the broad features of heavy ion collisions [41, 50], the inclusion of small shear viscous corrections were shown to be necessary to explain this anisotropy of the radial flow [26–30] (see Fig. 1.3 for a comparison of the η/s of various substances around their critical temperature T_c , including early estimates of the QGP viscosity). In conjunction with this, calculations from the AdS/CFT conjecture showed that in a conformal fluid, the value of the ratio of shear viscosity to entropy density η/s should take a value of $1/4\pi$ (and was conjectured to be an absolute minimum in all systems, although this is not yet proven; this is sometimes called the KSS bound) [51]. Since QCD approaches conformality in the limit of large energies, which coincides to a good extent with the region in which the quark-gluon is expected to be found, this result garnered a lot of interest, and further reinforced the idea of including shear viscous corrections as a way to better fit the various observables produced by the experiments.

Phenomenological extractions of the effective value of η/s by fitting relativistic viscous hydrodynamics to experimental measurements have been carried out [21, 26, 27, 52–54], and have shown that above the phase transition (i.e. at temperatures above ~ 150 MeV), the average η/s is very close but slightly larger than the conjectured ratio in the QGP. The temperature dependence $\eta/s(T)$ was also studied within hydrodynamical [55, 56] and hybrid approaches [57–61]; more recently, quantitative methods using Bayesian techniques for the analysis of large parameter space dimensionalities were used to determine with a high degree of confidence that the shear viscosity increases with temperature in this phase [62–64].

The low temperature behavior of the shear viscosity over entropy ratio can be

constrained by calculations with hadronic degrees of freedom. For zero net baryon density, the shear viscosity of a hadron gas was studied extensively up to temperatures of around 160 MeV [66–83], where the hadron gas turns into the quark-gluon plasma. Around the transition temperature, results from gluodynamics and QCD on a lattice have also provided estimates of η/s [84–87]. In addition to the temperature, the dependence $\eta(T, \mu_B)$ on the baryon chemical potential was also investigated [69, 71, 88]. In parallel, as shown on Fig. 1.3, it is generally known that the shear viscosity to entropy density ratio reaches a minimum around the phase transition temperatures for everyday substances; several effective models of QCD have predicted a similar behavior in the case at hand [73, 75, 89–93], which presents another motivation to study this coefficient. Importantly, it should be noted that the results of existing studies in the range of $T = 75 - 175$ MeV and $\mu_B = 0 - 600$ disagree with each other by up to one order of magnitude, which was also recently addressed in [82], where the authors find a considerable difference between the results from the UrQMD transport code [78], and the ones from the B3D transport approach [82, 94]. In Sections 4.1 and 4.2, by providing an independent computation of $\eta/s(T, \mu_B)$ in the hadronic phase using SMASH, the physical origin of this discrepancy is investigated, and, more generally, the key role of differences in the microscopic treatment of interactions between transport computations is highlighted.

1.2.2 Bulk viscosity

Since AdS/CFT calculations imply that it is identically zero [51], the bulk viscosity ζ (and its corresponding dimensionless ratio ζ/s), which can be thought of as the resistance to expansion of a fluid, has not been subject to the same extended treatment as shear viscosity [41]. It should be pointed out that although bulk viscosity is identically zero in conformal fluids and that QCD approaches conformality in the limit of high energies, there is no evidence that the nuclear matter which is produced in accelerators (even at the highest LHC energies) is formally a conformal fluid. This is especially true around the phase transition, where calculations from lattice QCD indicate large enhancements of the bulk viscosity in this regime [95, 96]. Although not exhaustive, some studies on the effect of bulk viscosity on some observables such as elliptic flow [97, 98] and particle spectra [99] were however made. More recently, bulk viscosity has started attracting more attention since it was pointed out by phenomenological studies in hybrid models that the inclusion of bulk viscosity as described by [100] was important in some cases to properly reproduce simultaneously the radial and azimuthal flow anisotropies [101, 102].

On the hadronic side, calculations of the bulk viscosity are notoriously more complicated than those of the shear viscosity (it will be shown in Chapter 4 that the amplitude of the fluctuations related to bulk viscosity are as much as ~ 25 times smaller than

those related to the shear case), and as such are a lot more scarce. The temperature dependence of the bulk viscosity of a full hadron gas was computed in [76, 81, 88, 103], and, similarly to the case of the shear viscosity, results from the various calculations differ from one another by an order of magnitude or more. Additional calculations using a simplified pion gas were also performed, providing additional insights on the behavior of ζ at low energy. Notably, [104] predicted a double bump structure where the low T maximum was explained from the explicit conformal breaking of the pion mass, [105] pointed out the importance of inelastic processes while obtaining a diverging bulk viscosity at $T = 0$, and finally, [106] further commented that the addition of a pion chemical potential due to its non-zero mass was also necessary to be fully consistent with a picture containing only elastic collisions. By providing an additional independent calculation of ζ and ζ/s in several systems in Section 4.3, some more light is shed on this as of yet still relatively unconstrained coefficient.

1.2.3 Cross-conductivity

The electrical conductivity describes the response of a medium either to an external electric field or an uneven distribution of charge density. As opposed to the previously discussed shear and bulk viscosities, it is only sensitive to transport cross sections involving charged particles. The electrical conductivity is used in theoretical predictions of the low-mass dilepton yield, which is directly proportional to this coefficient [107, 108]; it has also been related to the diffusion of magnetic fields in a medium [109–111] and is an important input to magnetohydrodynamics [112–114], allowing for a longer duration of the initial magnetic field when non-zero. Although they are expected to decrease over time, it has recently become more and more apparent that electric and magnetic fields are very strong during the early phases of a heavy ion collision. This has produced many explicit calculations of this conductivity, using hadronic kinetic theory [115], partonic transport models [116, 117], off-shell transport and dynamical quasiparticle models [118–121], holography [88, 122, 123], lattice QCD [107, 124–126], Dyson-Schwinger calculations [127], semianalytic calculations within perturbative QCD [128–130], and also taking into account strong magnetic fields [131, 132].

In the hadronic phase, some semianalytical calculations in pion gases were made using chiral perturbation theory [75, 111], in a pion gas using a sigma model where the effect of including medium-modified interactions was studied [133], in a sigma model with baryonic and mesonic interactions [134], and finally in resonance gas models [115, 118, 119]. Note that almost none of the previously mentioned calculations include a dynamical treatment of resonances, and thus this thesis contributes a solid determination of the electrical conductivity of a realistic hadronic gas which takes into account these effects.

Additionally, two new coefficients are introduced: the baryon-electric conductivity, and the strange-electric conductivity, which, together with the previously discussed electric conductivity, is dubbed the “cross-conductivity”. Since individual hadrons carry not only an electrical but also sometimes a baryonic and strange charge, it stands to reason that the application of an electric field can produce not only an electric, but also a baryonic or strange current. Although they will be introduced in more detail in Chapter 2, those two new transport parameters then essentially measure the baryonic or strange response of a medium when this one is subjected to an external electric field or uneven charge distributions. Although these coefficients have not been studied before, similar ideas of inspecting the cross effects of baryon-strange correlations were proposed in [135, 136], where it was suggested that those correlations could be used as a signature for the phase transition region. Our own new coefficients can in principle also be computed in the low temperature region in lattice QCD calculations, so that one could constrain several unknown parameters of hadronic resonance gas transport models, such as for example the abundance of degrees of freedom which need to be included at various temperatures, as well as their cross-sections with each other.

1.2.4 Jet quenching parameters

So-called “hard” interactions between constituent nucleons in experimental collisions can create partons which exhibit a very large transverse momentum p_T . In the case of proton-proton collisions, these highly off-shell particles then proceed to radiate gluons in a restricted angle range around their direction of propagation through a gradual return to an on-shell state via the emission of soft gluons, thus resulting in collimated particle showers called jets, which are then detected by experimental setups. In heavy ion collisions, such jets are typically created within the medium, and thus they must cross some length of it before reaching detectors, which will then suppress some of their energy through a modification of their radiative properties and through direct interaction with the medium. The study of this suppression, typically called jet quenching, is an important way in which the properties of the medium can be characterized [137, 138].

Since jets, composed of multiple partons, must cross a medium which is fully dynamic and spans from the high temperatures associated with the QGP to the lower ones where hadronic degrees of freedom dominate, a fully unified and self consistent picture of jet quenching physics is still under development, and thus a profusion of theoretical models of the jet/medium interactions exist, both on the perturbative [137–167] and non-perturbative levels [168–182]. However, it should be noted that the vast majority of these studies have only considered the effects of the QGP on the jet, omitting any possible contributions from hadronic interactions in the lower temperature region; it has however been shown that the hadronic phase can generate

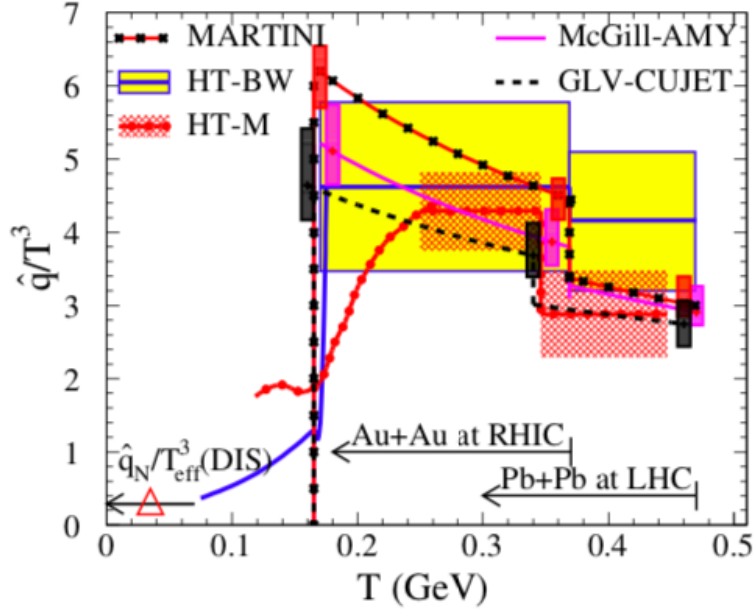


Figure 1.4: Jet quenching parameter \hat{q} vs temperature, as obtained from a cross-model study. Taken from [187].

a significant suppression of the transverse momentum both in a purely hadronic model [183] and hybrid approach [184], as well as exhibit qualitative differences in the nuclear factor and elliptic flow at $p_{\perp} = 2 - 6$ GeV [185, 186].

In the QGP, the jet quenching can usually be characterized by the transverse and longitudinal average momentum transfers per unit length squared \hat{q} and \hat{e} , which are transport coefficients that can be thought of as similar to the diffusion parameter of a large particle in a fluid, which has been done by many of the previously cited models. Interestingly, the transverse parameter \hat{q} has additionally been related to the shear viscosity η [188], providing an additional tomographic probe into the medium; one would then expect that the previously mentioned direct calculation of η should provide a result which is consistent with a calculation of \hat{q} using the same model.

Recently, a cross-model study [187] has managed to narrow down the value of \hat{q} at very high temperatures, which is shown on Fig. 1.4. In the explorative study presented in Chapter 5, a first estimation and parametrization of the analog hadronic quantities \tilde{q} and \tilde{e} is provided, and it is shown that although smaller by factors of 3-4 to their QGP counterparts, they are still large enough to have a significant effect on angular momentum distributions, an observable which characterizes how energy is spread away from the jet axis, similar to [189–191]; the transverse parameter \tilde{q} 's relation with the shear viscosity η is subsequently investigated, and comments are made on the validity of the relations presented in [188] in the hadron gas regime.

1.3 Structure of the thesis

This thesis is divided in several chapters, the first of which consisted of a contextualization of the rest, and which we assume the reader, now coming to its end, does not require to be reminded of yet.

In Chapter 2, two different ways of obtaining most of the previously discussed transport coefficients (with the exception of the jet quenching parameters) will be discussed in detail. The first one is the well-known Green-Kubo formalism, which will be derived from fundamental kinetic theory, while the second is the Chapman-Enskog formalism which allows for the linearization of the collision term of the previously discussed Boltzmann equations, thus leading directly to semianalytical relations for the shear and bulk viscosities as well as for the cross-conductivity; both of these methods will lead to direct expressions for all of those coefficients. Directly following is Chapter 3, which is dedicated to an in-depth look at the transport model which is used to obtain most of the results in this thesis, SMASH, and of all of its relevant features within the context of this work.

The next two chapters, 4 and 5, contain the bulk of the results which were obtained in the course of the writing of this thesis. The former concerns itself with the calculation of the shear and bulk viscosities and of the cross-conductivity, as well as their temperature and chemical potential dependences in a variety of systems of different complexities. This will be done using both the Green-Kubo and Chapman-Enskog formalism, where they will be compared when possible, usually in simpler systems to provide some degree of calibration to Green-Kubo calculations which can then be expanded to more complex ones. The latter explores the effects of adding a single high momentum particle in a hadron gas on angular distributions, or so-called “jet shapes”, and provides a first calculation of the temperature and particle momentum dependence of the hadronic jet quenching coefficients \tilde{q} and \tilde{e} .

Finally, in Chapter 6, we summarize our findings and look towards possible ways of improving or expanding the obtained results in future endeavours.

Chapter 2

Theory of transport coefficients

This chapter aims to cover in a non exhaustive way previous theoretical developments regarding the computation of transport coefficients in systems of varying complexity. Specifically, we will concentrate on ways to calculate the shear and bulk viscosity, as well as the so-called cross-conductivity (i.e. the vector of coefficients relating the movement of electric, baryonic and strange charges with respect to an external electric field; a more formal definition will be provided in Section 2.1.2).

We will first examine the well-known Green-Kubo formalism, which relates self correlations of dissipative fluctuations with the transport coefficients. This series of prescriptions are both very robust in terms of theoretical foundation and relatively reasonable in terms computational requirements, even for highly complex systems with many degrees of freedom. As such, this formalism will be used to provide most of the results presented in Chapter 4. One should note that the use of this prescription does rely on a series of *ansätze* and approximations, notably the exponentiality of the correlation functions and the characterization of the equilibrium in which the system finds itself. These do introduce some systematic uncertainties, which can and will be discussed in a general fashion in Sections 3.6 and 4.1, and more specifically to the bulk viscosity case in Section 4.3.

Second, we will discuss the Chapman-Enskog formalism, which aims to linearize the Boltzmann equation in order to obtain semi-analytical estimations of the different transport coefficients. Although this method is in principle one of the most straightforward and accurate ways of calculating those coefficients, its computational complexity and requirements grow exponentially as systems get more advanced, so that it is typically not practical to use it for more than relatively simple systems (i.e. with very few species and resonances). The fact that one obtains a semi-analytical result however does mean that this makes it a good comparison and calibration tool for the estimation of the systematic error on the Green-Kubo formalism. It should be noted that the author of these pages did not explicitly perform these calculations; as such, we will here present the general features of the formalism but will not go into the details

required to actually perform it.

2.1 The Green-Kubo formalism

Perhaps one of the simplest and oldest examples of what the Green-Kubo formalism explains, that is, linking fluctuations to transport coefficients, dates back from the early 19th century, when Robert Brown was studying the movement of large macromolecules (in this case pollen grains) in water. He observed that the smallest particles appeared to be moving in a random way, in what came to be known as the Brownian motion. Almost a century later, the mystery of the Brownian motion was resolved, when the Langevin equation of motion was introduced [192]¹

$$m\ddot{x} = -\gamma\dot{x} + R, \quad (2.1)$$

where m is the mass of the particle, γ some coefficient of friction of the liquid which slows the particle down and R is a random force which springs from the myriad of mini-interactions between water molecules and the grain of pollen. Although there is no way for us to describe R exactly, we can still enumerate some of its statistical properties.

1. It is on average zero, $\langle R \rangle = 0$.
2. The fluid is uniform, so R has no dependence on x .
3. Since it varies very rapidly and chaotically, it is assumed to be uncorrelated with itself over times larger than some characteristic time τ , that is

$$\langle R(t)R(t + \delta t) \rangle = 0 \text{ if } \delta t > \tau. \quad (2.2)$$

4. The rate at which correlations decay is independent of time (i.e. the water remains in the same equilibrium state over time).

Those simple postulates allow us to look at the solution of the Langevin equation and make some interesting preliminary calculations. The solution of differential Eq. (2.1) takes the form

$$\dot{x}(t) = \dot{x}(0)e^{-\frac{\gamma}{m}t} + \frac{1}{m} \int_0^t dt' e^{-\frac{\gamma}{m}(t-t')} R(t') \quad (2.3)$$

¹Formally speaking, Einstein did it first some years earlier [193], but the author is convinced the reader will forgive this breach of formality for the sake of the discussion.

We are interested in calculating the average kinetic energy in equilibrium, and thus we take the limit $t \rightarrow \infty$ and square both sides of the equation:

$$\lim_{t \rightarrow \infty} \langle \dot{x}^2(t) \rangle = \lim_{t \rightarrow \infty} \frac{1}{m^2} \int_0^t dt' \int_0^t dt'' e^{-\frac{\gamma}{m}(2t-t'-t'')} \langle R(t')R(t'') \rangle. \quad (2.4)$$

Remembering our previous postulates according to which only the difference $t'' - t'$ is important in the calculation of $\langle R(t')R(t'') \rangle$, rather than the actual value of t' , we now substitute $r = t - t''$ and $s = t'' - t'$, perform the r integration and obtain

$$\lim_{t \rightarrow \infty} \langle \dot{x}^2(t) \rangle = \frac{1}{2m\gamma} \int_{-\infty}^{\infty} ds e^{-\frac{\gamma}{m}s} \langle R(0)R(s) \rangle. \quad (2.5)$$

This can be further simplified by using the equipartition theorem² $\langle \dot{x}^2(t) \rangle = T/m$, as well as setting the timescale over which the random force is correlated to itself to being much shorter than the one over which friction has an effect, $\tau \ll m/\gamma$, so that

$$\gamma = \frac{1}{2T} \int_{-\infty}^{\infty} ds \langle R(0)R(s) \rangle. \quad (2.6)$$

This last result is a first example of what is known as the fluctuation-dissipation theorem, or Green-Kubo formula; it relates a transport coefficient γ to the self correlation $\langle R(0)R(s) \rangle$ of some thermodynamic variable R . In this case, since we cannot really easily associate a value with R , which is by definition a random force which we did not overly describe, the usefulness of this first formula is limited. However, as we shall see in the remainder of this section in quite a bit more detail and rigor, there are multiple other cases for which this type of Green-Kubo formulas can be derived to relate well-defined thermodynamic variables to transport coefficients.

The following subsections are loosely based on previous works by Zubarev [194] and Hosoya et al. [195]. The reader is encouraged to refer to these works for more details, especially if one wants to know about the quantum mechanics version of the derivation of this formalism; notably, §15 and §22 in Zubarev and §2 in Hosoya et al. should be of interest.

2.1.1 Linear response theory

Before discussing the actual calculation of the transport coefficients, we will review in this section some basic concepts of linear response theory which will be of great use later on.

We are interested in describing the response of a statistical ensemble to an external

²We use the natural convention of units, in which $k = c = 1$.

perturbation. The system is assumed to be described by

$$H(p, q) = H_0(p, q) + H_t^l(p, q) \quad (2.7)$$

where the first term is the undisturbed Hamiltonian of the system and does not depend on time, and the second describes the time dependent interaction energy of the system with the external forces. The distribution function is defined from the Liouville equation

$$\frac{\partial f}{\partial t} = \{H_0 + H_t^l, f\}, \quad (2.8)$$

where the curly braces denote the Poisson bracket

$$\{A, B\} = \frac{\partial A}{\partial q} \frac{\partial B}{\partial p} - \frac{\partial A}{\partial p} \frac{\partial B}{\partial q}, \quad (2.9)$$

where summation over all particles is implicit on the right-hand side. Additionally, we require that H_t^l was absent at $t = -\infty$ so that f must be in a state of equilibrium at that time. This initial condition and the previous Liouville equation completely define the distribution function. Although many functions would in principle satisfy those two requirements, we can narrow the choice by assessing the characteristics of the considered system. In the present discussion we choose an equilibrium which was defined by a temperature T , volume V and particle number N , which corresponds to the canonical distribution, and thus

$$\begin{aligned} f(t)|_{t=-\infty} = f_0 &= Q^{-1}(T, V, N) e^{-H_0/T} \\ Q(T, V, N) &= \int e^{-H_0/T} d\Gamma, \quad d\Gamma = \frac{dpdq}{N!h^{3N}}. \end{aligned} \quad (2.10)$$

In order to find a solution at all times for f , we first apply the following transformation

$$f_1 = e^{-itL} f, \quad (2.11)$$

with L being the differential Liouville operator defined by

$$itL = \{H, f\}. \quad (2.12)$$

The factor e^{-itL} then corresponds to the evolution operator, which acts on any function of the coordinates $p(0)$ and momenta $q(0)$ at $t = 0$ into the same function at a later time as a function of $q(t)$ and $p(t)$. Noting that the equilibrium part of the Hamiltonian vanishes in Liouville's equation (2.8), we then get

$$\frac{\partial f_1}{\partial t} = \{H_t^l(t), f_1\}, \quad H_t^l(t) = e^{itL} H_t^l. \quad (2.13)$$

This second equation is a classical analogue of the Heisenberg representation in quantum mechanics. Following directly from the initial condition given by Eq. (2.10), we also have

$$f_1(t)|_{t=-\infty} = f_0. \quad (2.14)$$

We write the solution to differential Eq. (2.13) with initial condition (2.14) in the form of a single integral equation

$$f_1(t) = f_0 + \int_{-\infty}^t \{H_t^l(t'), f_1(t')\} dt', \quad (2.15)$$

or

$$f(t) = f_0 + \int_{-\infty}^t e^{i(t-t')L} \{H_t^l, f_1(t')\} dt', \quad (2.16)$$

If we assume that the perturbation H_t^l is small, we can further approximate the previous result by iteration while taking f_0 as the zeroth approximation, so that

$$f(t) = f_0 + \int_{-\infty}^t \{H_t^l(t' - t), f_0\} dt'. \quad (2.17)$$

This distribution can also be written in other ways, noting for example that

$$\{H_t^l, f_0\} = -\beta \{H_t^l, H_0\} f_0, \quad (2.18)$$

where we introduced the inverse temperature $\beta = 1/T$. We then get

$$f(t) = f_0 \left(1 - \beta \int_{-\infty}^t \{H_t^l(t' - t), H_0\} dt' \right). \quad (2.19)$$

This linear approximation in H_t^l now allows us to calculate the average value of any dynamic variable that is a function of p and q , according to the well-known averaging formula

$$\langle A \rangle = \int A(p, q) f(p, q, t) d\Gamma. \quad (2.20)$$

Combining each of Eqs. (2.17) and (2.19) with (2.20), we obtain

$$\langle A \rangle = \langle A \rangle_0 + \int_{-\infty}^t \langle \{A, H_t^l(t' - t)\} \rangle_0 dt', \quad (2.21)$$

and

$$\begin{aligned} \langle A \rangle &= \langle A \rangle_0 - \beta \int_{-\infty}^t \langle A \dot{H}_t^l(t' - t) \rangle_0 dt' \\ &= \langle A \rangle_0 + \beta \int_{-\infty}^t \langle \dot{A}(t - t') H_t^l \rangle_0 dt', \end{aligned} \quad (2.22)$$

where

$$\langle \dots \rangle_0 = \int \dots f_0 d\Gamma, \quad (2.23)$$

is the averaging with respect to the equilibrium distribution, and $\dot{A} = \{A, H_0\}^3$. The last equality of Eq. (2.22) derives from the fact that the product of dynamical variables in a state of equilibrium only depends on the time difference

$$\langle A(t)B(t') \rangle_0 = \langle A(t-t')B \rangle_0 = \langle AB(t'-t) \rangle_0. \quad (2.26)$$

Differentiating with respect to time, we get

$$\langle \dot{A}(t-t')H_t^l \rangle_0 = -\langle AH_t^l(t'-t) \rangle_0. \quad (2.27)$$

Equations (2.21) and (2.22) are the full classical expressions of the average value of any dynamical variable if non-equilibrium forces are small; in one form or the other, this is one of the specific tools which will allow us to recover the Green-Kubo formulas for transport coefficients.

2.1.2 Cross-conductivity

In this section we will examine the effect of applying an electric field on a statistical ensemble using the previous formalism. The electric field will take the following shape:

$$\mathbf{E}(t) = \mathbf{E} \cos \omega t e^{\varepsilon t} = \text{Re}\{e^{i\omega t + \varepsilon t}\}. \quad (2.28)$$

This electric field is spatially uniform and periodic in time, and is assumed to be switched on adiabatically at $t = -\infty$. Furthermore, we will assume that the charges are here not under the effect of each other's potentials and are free-streaming from collision to collision (i.e. any screening effect caused by the proximity of other particles is assumed to be small). We start out by writing out the corresponding perturbation to the hamiltonian:

$$H_t^l = -(\mathbf{E} \cdot \mathbf{P}) \cos \omega t e^{\varepsilon t}, \quad (2.29)$$

³The dot notation is here not random, and does in fact correspond in a lot of cases to the time derivative of the dynamical variable A. Remembering that in classical mechanics the kinetic part of the hamiltonian is

$$\sum_k \frac{1}{2} q_k^2 / m_k, \quad (2.24)$$

where the sum goes over all particles in the system (each with a mass m_k), and combining with the definition of the Poisson bracket (2.9), we see that the first term of Eq. (2.9) falls to zero, whereas the second term contributes

$$\frac{\partial A}{\partial p} \frac{\partial H_0}{\partial q} = \frac{\partial A}{\partial p} \frac{q}{m} = \frac{\partial A}{\partial p} \frac{\partial p}{\partial t} = \frac{\partial A}{\partial t} \quad (2.25)$$

summed over particles.

where we introduced the polarization vector

$$\mathbf{P} = \sum_k e_k \mathbf{x}_k, \quad (2.30)$$

which sums over all particles positions x_k and electrical charge e_k . Let us now remember that an electric field acting upon a system of particles will create an electric current that will be proportional to the field, considering microscopic fluctuations to vanish on average:

$$\langle J_\alpha^Q(t) \rangle = \sigma_{\alpha\beta}^{QQ} \langle E_\beta \rangle, \quad (2.31)$$

where α and β run over the 3 dimensions, and

$$J_\alpha^Q(t) = \sum_k e_j \dot{x}_{j\alpha}(t) = \dot{P}_\alpha(t) \quad (2.32)$$

is the instantaneous electric current. Eq. (2.31) is considered the constitutive relation of the electrical conductivity $\sigma_{\alpha\beta}^{el}$, in the sense that it is this relation which defines it as a coefficient. Coincidentally, in the previous section we defined a way to calculate the average of any dynamical variable, provided we know the form of H_t^l . Using the first expression of Eq. (2.22) and Eq. (2.29), we obtain

$$\begin{aligned} \langle J_\alpha^Q \rangle &= \langle J_\alpha^Q \rangle_0 - \beta \int_{-\infty}^t \langle J_\alpha^Q \dot{H}_t^l(t' - t) \rangle_0 dt' \\ &= \beta \int_{-\infty}^t \langle J_\alpha^Q \dot{P}_\beta(t' - t) \rangle_0 E_\beta e^{i\omega t - \varepsilon t} dt', \end{aligned} \quad (2.33)$$

where we used the fact that on average in equilibrium the electric current vanishes. Therefore, combining Eqs. (2.31), (2.32) and (2.33), we obtain the electric conductivity:

$$\sigma_{\alpha\beta}^{QQ} = \beta \int_{-\infty}^t \langle J_\alpha^Q J_\beta^Q(t' - t) \rangle_0 e^{i\omega t - \varepsilon t} dt', \quad (2.34)$$

It is possible to simplify the previous equation in some ways. First of all, let us go to a more specific case by assuming a static field ($\omega = 0$). Second, we shall assume that the system is isotropic, i.e. its response to an electric field is symmetric in all directions. Third, the parameter ε can be made as small as desired; we thus take it to zero, which allows us to flip the time axis, so that

$$\sigma^{QQ} = \beta \int_0^\infty \langle J_x^Q J_x^Q(t') \rangle_0 dt'. \quad (2.35)$$

This equation paints a very different picture conceptually than the previous one. Namely, instead of adiabatically switching on a perturbation at $t = -\infty$, we are now looking at a system which is in equilibrium, and which, as all equilibrium systems, pro-

duces small fluctuations from the expectation value due to microscopic processes; this equation then relates the adiabatic switching *off* of an arbitrarily small equilibrium fluctuation to the electric conductivity.

Let us now expand this discussion by noting that the application of an electric field can also produce associated currents. For example, in a hadron gas or a quark gluon-plasma, the electrically charged particles also often carry other charges such as the baryonic or strange charges; additionally, even ensembles of particles which do not have an electric charge could start moving in a coherent way, provided other charged particles are allowed to collide with them. As such, we write, similarly as we did for the electric conductivity in Eq. (2.31), constitutive relations for baryon-electric

$$\langle J_\alpha^B(t) \rangle = \sigma_{\alpha\beta}^{QB} \langle E_\beta \rangle \quad (2.36)$$

and strange-electric

$$\langle J_\alpha^S(t) \rangle = \sigma_{\alpha\beta}^{QS} \langle E_\beta \rangle \quad (2.37)$$

conductivities, where we, similarly as in Eq. (2.32), defined the baryon and strange currents:

$$J_\alpha^B(t) = \sum_k B_j \dot{x}_{j\alpha}(t) \quad (2.38)$$

and

$$J_\alpha^S(t) = \sum_k S_j \dot{x}_{j\alpha}(t), \quad (2.39)$$

where B_j and S_j are respectively the baryonic and strange charge of a particle j . The union of these 3 quantities σ^{QQ} , σ^{QB} and σ^{QS} , for example in a vector $\boldsymbol{\sigma} = (\sigma^{QQ}, \sigma^{QB}, \sigma^{QS})$, is what will be further on referred to as the cross-conductivity. Following the same steps as we did for the electric conductivity, we obtain

$$\sigma^{QB} = \beta \int_0^\infty \langle J_x^B J_x^Q(t') \rangle_0 dt'. \quad (2.40)$$

and

$$\sigma^{QS} = \beta \int_0^\infty \langle J_x^S J_x^Q(t') \rangle_0 dt'. \quad (2.41)$$

for respectively the baryon-electric and strange-electric conductivities.

2.1.3 Shear and bulk viscosity

The derivation of expressions for the shear and bulk viscosities is closely intertwined, as both of those quantities (as well as the thermal diffusion) spring from fluctuations of the same energy-momentum tensor; for the sake of avoiding duplication, we will carry out both simultaneously.

In order to calculate the viscosities, we will consider systems which are slightly more complex than the ones previously discussed, in that instead of consisting of a global equilibrium which is modified by some external factor, we now look at an ensemble in which thermodynamical parameters such as temperature or density can only be defined locally. This is the hydrodynamic picture, in which this set of local parameters describe the inhomogeneous distributions and their interactions which form the system. The overarching characteristic of this system is then the energy-momentum conservation law

$$\partial_\mu T^{\mu\nu}(\mathbf{x}, t) = 0, \quad (2.42)$$

where $T^{\mu\nu}$ is the energy-momentum tensor. In an analogous way as what we did in section (2.1.1), we must first determine the shape for the non-equilibrium distribution function f . As for all such functions in the classical case, f must satisfy the Liouville equation (2.8); additionally we will require that

$$\frac{df}{dt} = 0. \quad (2.43)$$

This last condition on the distribution function comes from a picture of separated scales in our description: we assume that in a small interval of time τ_f in which such a non-equilibrium is established, f depends on time only through its parameters, and comparatively slowly with a macroscopic characteristic time $\tau_M \gg \tau_f$ at which we will look at the system. We introduce the time-independent function $B(\mathbf{x}, t)$

$$B(\mathbf{x}, t) = \varepsilon \int_{-\infty}^t dt_1 e^{\varepsilon(t_1-t)} F^\nu(\mathbf{x}, t_1) T_{0\nu}(\mathbf{x}, t_1), \quad (\varepsilon \rightarrow +0), \quad (2.44)$$

where

$$F^\nu(\mathbf{x}, t) = \beta(\mathbf{x}, t) u^\nu(\mathbf{x}, t), \quad (2.45)$$

with $\beta(\mathbf{x}, t)$ and $u(\mathbf{x}, t)$ respectively the local Lorentz invariant inverse temperature and local velocity of the fluid, for which

$$u^\nu(\mathbf{x}, t_1) u_\nu(\mathbf{x}, t_1) = 1. \quad (2.46)$$

We show that $B(\mathbf{x}, t)$ is independent of t by taking a time derivative

$$\begin{aligned} \frac{d}{dt} B(\mathbf{x}, t) &= \varepsilon F^\nu(\mathbf{x}, t) T_{0\nu}(\mathbf{x}, t) \\ &\quad - \varepsilon^2 \int_{-\infty}^t dt_1 e^{\varepsilon(t_1-t)} F^\nu(\mathbf{x}, t_1) T_{0\nu}(\mathbf{x}, t_1), \end{aligned} \quad (2.47)$$

which is true if both $T_{0\nu}(\mathbf{x}, t)$ and $B(\mathbf{x}, t)$ are finite as $\varepsilon \rightarrow +0$. Integrating by parts

gives

$$\begin{aligned}
B(\mathbf{x}, t) &= F^\nu(\mathbf{x}, t)T_{0\nu}(\mathbf{x}, t) \\
&\quad - \int_{-\infty}^t dt_1 e^{\varepsilon(t_1-t)} (\dot{F}^\nu T_{0\nu} + F^\nu \dot{T}_{0\nu}),
\end{aligned} \tag{2.48}$$

Now if we remember the conservation law (2.42), integrate by parts and neglect higher order terms, we get

$$\begin{aligned}
\int d^3x B(\mathbf{x}, t) &= \int d^3x F^\nu(\mathbf{x}, t)T_{0\nu}(\mathbf{x}, t) \\
&\quad - \int d^3x \int_{-\infty}^t dt_1 e^{\varepsilon(t_1-t)} T_{\mu\nu}(\mathbf{x}, t) \partial^\mu F^\nu(\mathbf{x}, t)
\end{aligned} \tag{2.49}$$

This last result allows us to write the final form of the distribution function as a functional of $B(\mathbf{x}, t)$, which will also be time independent, such that

$$\begin{aligned}
f &= Q^{-1} \exp\left(-\int d^3x B(\mathbf{x}, t)\right), \\
Q &= \int d\Gamma \exp\left(-\int d^3x B(\mathbf{x}, t)\right),
\end{aligned} \tag{2.50}$$

with $d\Gamma$ defined in the same way as in Eq. (2.10). The distribution function as defined in Eqs. (2.49) and (2.50) contains two parts; an equilibrium part, which corresponds to the first term on the right-hand side of Eq. (2.49), and a non-equilibrium part, which contains the thermodynamic forces $\partial^\mu F^\nu$. We note that it is possible to start from the formalism we introduced in Section 2.1.1 to obtain the local equilibrium distribution of a system with conservation laws

$$\begin{aligned}
f_l &= Q_l^{-1} \exp\left(-\int d^3x F^\nu(\mathbf{x}, t)T_{0\nu}(\mathbf{x}, t)\right), \\
Q_l &= \int d\Gamma \exp\left(-\int d^3x F^\nu(\mathbf{x}, t)T_{0\nu}(\mathbf{x}, t)\right),
\end{aligned} \tag{2.51}$$

for which derivation we refer the reader to §§19-20 in Zubarev [194].

If we now move to the case where the thermodynamical forces are small enough that non-equilibrium processes take place slowly, we can further linearize the distribution function. We write (2.50) as

$$\begin{aligned}
f &= Q^{-1} e^{-A+B}, \\
Q &= \int d\Gamma e^{-A+B},
\end{aligned} \tag{2.52}$$

where

$$\begin{aligned}
A &= \int d^3x F^\nu(\mathbf{x}, t) T_{0\nu}(\mathbf{x}, t), \\
B &= \int d^3x \int_{-\infty}^t dt_1 e^{\varepsilon(t_1-t)} T_{\mu\nu}(\mathbf{x}, t) \partial^\mu F^\nu(\mathbf{x}, t),
\end{aligned} \tag{2.53}$$

where μ is now summed to generalize the possible influences of the thermodynamic forces on the distributions. Since we assume those forces to be small, we expand in a series of B

$$e^{-A+B} = e^{-A} + B e^{-A} + \dots \tag{2.54}$$

so that

$$f \cong (1 + B - \langle B \rangle_l) f_l \tag{2.55}$$

Following the classical averaging of quantities introduced by Eq. (2.20), we can write a linear relation for the expectation value of the energy-momentum tensor with respect to the thermodynamical forces

$$\begin{aligned}
\langle T_{\mu\nu}(\mathbf{x}, t) \rangle &= \langle T_{\mu\nu}(\mathbf{x}, t) \rangle_l \\
&+ \int d^3x' \int_{-\infty}^t dt' e^{\varepsilon(t'-t)} \langle T_{\mu\nu}(\mathbf{x}, t), T_{\rho\sigma}(\mathbf{x}', t') \rangle_l \partial^\rho F^\sigma(\mathbf{x}', t'),
\end{aligned} \tag{2.56}$$

with

$$\begin{aligned}
\langle T_{\mu\nu}(\mathbf{x}, t), T_{\rho\sigma}(\mathbf{x}', t') \rangle_l &\equiv \langle T_{\mu\nu}(\mathbf{x}, t) (T_{\rho\sigma}(\mathbf{x}', t') - \langle T_{\rho\sigma} \rangle_l) \rangle_l \\
&= \langle (T_{\mu\nu}(\mathbf{x}, t) - \langle T_{\mu\nu} \rangle_l) (T_{\rho\sigma}(\mathbf{x}', t') - \langle T_{\rho\sigma} \rangle_l) \rangle_l
\end{aligned} \tag{2.57}$$

Note that Eq. (2.56) has a similar shape to what we previously saw in the general case in Eqs. (2.21) and (2.22), as well as in the specific case of the cross-conductivity with Eq. (2.33), that is, an equilibrium value to which is added a self-correlation of the averaged quantity.

What remains to be done in order to obtain the shear and bulk viscosity is now simply to express specific transport coefficients in the form of a constitutive relation of the form of Eq. (2.31). To this effect, we decompose the energy-momentum tensor in terms of the four-velocity u^μ

$$T^{\mu\nu} = \epsilon u^\mu u^\nu - p \Delta^{\mu\nu} + P^\mu u^\nu + P^\nu u^\mu + \pi^{\mu\nu}. \tag{2.58}$$

We introduced the coefficients

$$\begin{aligned}
\epsilon &= u_\rho u_\sigma T^{\rho\sigma}, \\
p &= -\frac{1}{3}\Delta_{\rho\sigma}T^{\rho\sigma}, \\
P_\mu &= \Delta_{\mu\rho}u_\sigma T^{\rho\sigma}, \\
\pi_{\mu\nu} &= (\Delta_{\mu\rho}\Delta_{\nu\sigma} - \frac{1}{3}\Delta_{\mu\nu}\Delta_{\rho\sigma})T^{\rho\sigma},
\end{aligned} \tag{2.59}$$

where $\Delta_{\mu\nu} = g_{\mu\nu} - u_\mu u_\nu$, with $g_{\mu\nu}$ being the metric. Note that $\Delta_{\mu\nu}$ is orthogonal to u^μ ($\Delta_{\mu\nu}u^\mu = 0$), that consequently P_μ and $\pi_{\mu\nu}$ are also perpendicular to the velocity, and finally that $\pi_{\mu\nu}$ is traceless. In the comoving frame where $u = (1, 0, 0, 0)$, the coefficients can be written in a way which give them physical meaning:

$$\begin{aligned}
\epsilon &= T_{00}, \\
p &= -\frac{1}{3}T^k_k, \\
P_k &= T_{0k}, \quad P_0 = 0, \\
\pi^k_\ell &= (\delta^k_i \delta^j_\ell - \frac{1}{3}\delta^k_\ell \delta^j_i)T^i_j,
\end{aligned} \tag{2.60}$$

where the indices run over $(i, j, k, \ell = 1, 2, 3)$. In this frame we can in this way define ϵ as the energy density, p as the pressure, P_μ as the heat current and $\pi_{\mu\nu}$ as the viscous shear-stress tensor. From the definition of the local equilibrium (2.51) we see that the orthogonal parts of $T^{\mu\nu}$ will on average fall to zero

$$\langle P^\mu \rangle_l = 0, \quad \langle \pi^{\mu\nu} \rangle_l = 0. \tag{2.61}$$

This means that in a local equilibrium, we have

$$\langle T^{\mu\nu} \rangle_l = (\langle \epsilon \rangle_l + \langle p \rangle_l)u^\mu u^\nu - \langle p \rangle_l g^{\mu\nu}. \tag{2.62}$$

From the definitions of F^ν (2.45) and $T_{\mu\nu}$ (2.58), we can rewrite the contraction that happens between those two quantities in the non-equilibrium part of the distribution function such that

$$T_{\rho\sigma}\partial^\rho F^\sigma = \beta\pi_{\rho\sigma}\partial^\rho u^\sigma + \beta P_\rho(\beta^{-1}\partial^\rho\beta + Du^\rho) + \epsilon D\beta - \beta p\partial_\rho u^\rho, \tag{2.63}$$

where $D = u^\rho\partial_\rho$, which corresponds to the time derivative in the comoving frame. Using the ideal fluid equation $\partial_\mu\langle T^{\mu\nu} \rangle_l = 0$, we can express the quantity $D\beta$ as

$$D\beta = \beta \frac{\partial\langle p \rangle_l}{\partial\langle \epsilon \rangle_l \partial_\mu u^\mu}. \tag{2.64}$$

Plugging this last result into the previous one, we get

$$T_{\rho\sigma}\partial^\rho F^\sigma = \beta\pi_{\rho\sigma}\partial^\rho u^\sigma + \beta P_\rho(\beta^{-1}\partial^\rho\beta + Du^\rho) - \beta p'\partial_\rho u^\rho, \quad (2.65)$$

where we defined

$$p'(\mathbf{x}, t) = p(\mathbf{x}, t) - \frac{\partial\langle p(\mathbf{x}, t)\rangle_l}{\partial\langle\epsilon(\mathbf{x}, t)\rangle_l}\epsilon(\mathbf{x}, t). \quad (2.66)$$

Let us now look back to Eq. (2.56), which described the full linear response of the energy-momentum tensor, and more specifically to the correlation part of the integral, $\langle T_{\mu\nu}(\mathbf{x}, t)T_{\rho\sigma}(\mathbf{x}', t')\rangle_l$. According to Curie's theorem, linear coupling of tensors is non-zero only in the case where these tensors have the same rank and parity; using the decomposition of $T_{\mu\nu}$ (2.58), and the definitions of the coefficients (2.59), we can write

$$\begin{aligned} \langle p', p'\rangle_l &= L_\Pi, \\ \langle P_\mu, P_\nu\rangle_l &= -L_P\Delta_{\mu\nu}, \\ \langle \pi_{\mu\nu}, \pi_{\rho\sigma}\rangle_l &= L_\pi\frac{1}{2}(\Delta_{\mu\rho}\Delta_{\nu\sigma} + \Delta_{\mu\sigma}\Delta_{\nu\rho} - \frac{2}{3}\Delta_{\mu\nu}\Delta_{\rho\sigma}), \end{aligned} \quad (2.67)$$

where L_p and L_π are scalars defined as

$$\begin{aligned} L_P &= -\frac{1}{3}\langle P^\alpha(\mathbf{x}, t), P_\alpha(\mathbf{x}, t)\rangle_l, \\ L_\pi &= \frac{1}{5}\langle \pi^{\alpha\beta}(\mathbf{x}, t), \pi_{\alpha\beta}(\mathbf{x}, t)\rangle_l. \end{aligned} \quad (2.68)$$

Note that the prefactors $\frac{1}{3}$ and $\frac{1}{5}$ come from the number of independent elements in their respective associated sum, that is, for the comoving frame, 3 non-zero independent elements in the P_μ vector, and 5 independent elements in the symmetric 3x3 traceless tensor $\pi_{\mu\nu}$. Assuming that the variations of the thermodynamic forces from Eq. (2.56) are small with respect to the correlation lengths of L_Π , L_P and L_π , and remembering that the local equilibrium average of the heat current and shear-stress tensor are zero, we rewrite the linear response of the energy-stress tensor as 3 constitutive equations respectively for the shear viscosity, thermal conductivity and bulk viscosity:

$$\begin{aligned} \langle \pi_{\mu\nu}(\mathbf{x}, t)\rangle &= \eta\frac{1}{2}\left\{\Delta_\rho^\mu\Delta_\sigma^\nu(\partial^\rho u^\sigma(\mathbf{x}, t) + \partial^\sigma u^\rho(\mathbf{x}, t)) \right. \\ &\quad \left. - \frac{2}{3}\Delta^{\mu\nu}\Delta_{\rho\sigma}\partial^\rho u^\sigma(\mathbf{x}, t)\right\}, \\ \langle P_\mu(\mathbf{x}, t)\rangle &= -\kappa\Delta_\rho^\mu(\beta^{-1}(\mathbf{x}, t)\partial^\rho\beta(\mathbf{x}, t) + Du^\rho(\mathbf{x}, t)), \\ \langle p(\mathbf{x}, t)\rangle - \langle p(\mathbf{x}, t)\rangle_l &= -\zeta\partial_\rho u^\rho(\mathbf{x}, t) \end{aligned} \quad (2.69)$$

where the transport coefficients have been defined as

$$\eta = \frac{\beta(\mathbf{x}, t)}{5} \int d^3x' \int_{-\infty}^t dt' e^{\epsilon(t'-t)} \langle \pi^{\alpha\beta}(\mathbf{x}, t), \pi_{\alpha\beta}(\mathbf{x}', t') \rangle_l, \quad (2.70)$$

$$\kappa = \frac{\beta(\mathbf{x}, t)}{3} \int d^3x' \int_{-\infty}^t dt' e^{\epsilon(t'-t)} \langle P^\alpha(\mathbf{x}, t), P_\alpha(\mathbf{x}', t') \rangle_l, \quad (2.71)$$

$$\zeta = \beta(\mathbf{x}, t) \int d^3x' \int_{-\infty}^t dt' e^{\epsilon(t'-t)} \langle p'(\mathbf{x}, t), p'(\mathbf{x}', t') \rangle_l. \quad (2.72)$$

In a similar way as we did for the case of the electric conductivity with Eq. (2.34), let us now try to simplify these newly found expressions for the shear and bulk viscosities (we will now drop the thermal conductivity from the discussion, as it will play no further role in this thesis). First of all, let us once again assume that the system is not only in equilibrium, but isotropic; this allows us to remove the space dependence of both equations, the time dependence of the inverse temperature and the summation over indices in the case of the shear viscosity, so that we only focus on one sub element of the tensor, π^{xy} . Second, we will take the limit of the parameter ϵ to zero, and choose $t = 0$ as the initial time, which once again allows us to flip the time axis. Finally, let us make one more simplification to the bulk equation by noting that in the case which will interest us, the energy density ϵ is conserved; in that specific case, the second term of the right-hand side of Eq. (2.66) falls to zero. This yields

$$\eta = \frac{V}{T} \int_0^\infty dt' \langle \pi^{xy}(0), \pi^{xy}(t') \rangle_l, \quad (2.73)$$

$$\zeta = \frac{V}{T} \int_0^\infty dt' \langle p(0), p(t') \rangle_l. \quad (2.74)$$

We note that these equations present a very similar picture as did Eq. (2.35) for the case of electric conductivity; that is, we are once again looking at a system which is in equilibrium, and study how the adiabatic decay of fluctuations around this equilibrium relates to transport coefficients. Equations (2.73) and (2.74) (as well as (2.35), (2.40) and (2.41) from the previous section) will be used throughout Chapter 4 to obtain the transport coefficients of the hadron gas in a wide parameter space.

2.2 The Chapman-Enskog formalism

The so-called Chapman-Enskog formalism is a way to obtain semi-analytical formulas for the transport coefficients in gas mixtures which are in the hydrodynamical stage; we here present a short overview of its defining features and formalism, where we loosely follow the discussion in §1 from Chapter 5 in [43] and Chapters 2-5 in [75]. It is based upon two foundations:

1. The previously introduced relativistic Boltzmann transport equation, which can be written in a very general form as

$$p^\mu \frac{\partial f_1}{\partial x^\mu} + m_1 \frac{\partial(\mathcal{F}^\mu f_1)}{\partial p^\mu} = C[f_1, f_2], \quad (2.75)$$

where f_1 and f_2 are one-particle distribution functions for different particle species, m_1 is the mass of the first of these particle species, and $C[f_1, f_2]$ is the collision term between these two distributions⁴. The first term on the left-hand side can be interpreted as the propagation or diffusion term, and the second one as the influence of any Lorentz invariant external forces K^μ on the statistical distribution functions; we will assume there are no external forces for most of this section, until the very end where we will introduce an electric perturbation in order to get expressions for the cross-conductivities in Section 2.2.3. We rewrite the Boltzmann equation to separate the explicit comoving time derivative and orthogonal convective term,

$$p^\mu u_\mu D f_1 + p^\mu \nabla_\mu f_1 = C[f_1, f_2], \quad (2.77)$$

with $\nabla = \Delta^{\mu\nu} \partial_\nu$ and $D = u^\mu \partial_\mu$, same as in Eq. (2.63). $C[f_1, f_2]$ is the collision term resulting of the interactions between the two incoming particle species (or, by extension, with itself if said particle can collide with other particles of the same species). It can be written in a general way as

$$C[f_1, f_2] = \frac{1}{(2\pi)^3} \int d\Omega dk_2 v_{rel} \frac{d\sigma_{12}}{d\Omega} [f_3 f_4 - f_1 f_2], \quad (2.78)$$

where v_{rel} is the relative velocity between the incoming particles $d\sigma_{12}/d\Omega$ is the differential cross-section and $f_{3,4}$ are the distribution functions of the outgoing particles.

2. A well defined hierarchy of scales in the system, which can be written as

$$L \gg h \gg \lambda_{mfp} \gg R. \quad (2.79)$$

Starting from the smallest scale, R is defined as the range of the interaction potential within a collision. This is assumed to be much smaller than the mean free

⁴An even more general form would consider many types of particles interacting with each other,

$$\sum_i \left(p^\mu \frac{\partial f_i}{\partial x^\mu} + m_i \frac{\partial(\mathcal{F}^\mu f_i)}{\partial p^\mu} \right) = \sum_{i,j} C[f_i, f_j], \quad (2.76)$$

where both i and j run over all particle species; this massive increase in combinatorics is what makes using this formalism complicated for highly complex gases with many different particles. For the remainder of the discussion, we will consider the one-particle case.

path λ_{mfp} of particles between collisions, and is essentially the dilute gas approximation in which only binary collisions occur, which is one of the assumptions made in the derivation of the previously mentioned transport equation. The length h is assumed to be a characteristic hydrodynamic length in which many particles are present and many collisions occur, so that all 5 hydrodynamic fields (i.e. a temperature T , number density n and 3-velocity \mathbf{u}) can be locally defined. The largest scale is the system size L , which is once again assumed to be much larger than the previous hydrodynamic scale. Dividing (2.79) by a characteristic thermal velocity $v \sim \sqrt{T/m_1}$, we define a series of characteristic timescales in the system

$$\tau_L \gg \tau_h \gg \tau_{mfp} \gg \tau_R. \quad (2.80)$$

In this picture there are two subsequent processes: a fast (kinetic) stage where the initial state quickly thermalizes locally due to large number of collisions in τ_h , and a slow (hydrodynamic) stage in which all the local equilibria tend towards a global equilibrium through the interaction of the hydrodynamical fields. At this scale, it is assumed that only these hydrodynamic fields vary with respect to the individual positions and momenta of the particles, and as such the distribution functions only depend indirectly upon those, but rather have a functional dependence on the fields

$$f(p, q) = f[T, n, \mathbf{u}] \quad (2.81)$$

Knowledge of these fields at every point in the system (or equivalently at some position \mathbf{r} with all their derivatives) leads to being able to build a so-called Hilbert-class or normal solution to the distribution function.

The Chapman-Enskog formalism is a straightforward way of obtaining such a normal solution as an expansion of the previously introduced Knudsen number, which here corresponds to the ratio $\lambda_{mfp}/h = \tau_{mfp}/\tau_h$. It is relatively intuitive to see that $h^{-1} \sim |\nabla \ln f|$, and thus we can see that such an expansion is actually equivalent to an expansion in powers of hydrodynamic gradients. Specifically, we expand the distribution function using the parameter ε such that

$$f_p = f_p^{(0)} + \varepsilon f_p^{(1)} + \varepsilon^2 f_p^{(2)} + \dots \quad (2.82)$$

The Boltzmann equation (2.77) is rewritten by introducing $\nabla \rightarrow \varepsilon \nabla$

$$p^\mu u_\mu D f_1 + \varepsilon p^\mu \nabla_\mu f_1 = C[f_1, f_2], \quad (2.83)$$

and the comoving derivative is redefined as

$$D f_p = \varepsilon (D f_p)^{(1)} + \varepsilon^2 (D f_p)^{(2)} + \dots \quad (2.84)$$

The non-uniformity parameter ε is essentially a book-keeping parameter to keep track of the order of the expansion and is to be set to 1 at the end of the calculation. It is used to create a hierarchy of solvable equations by equating similar powers of ε on both sides of the Boltzmann equation, which read

$$0 = C[f_1^{(0)}, f_2^{(0)}], \quad (2.85)$$

$$p^\mu u_\mu (Df_1)^{(r)} + p^\mu \nabla_\mu f_1^{(r-1)} = \sum_{s=0}^r \left(C[f_1^{(s)}, f_2^{(r-s)}] + C[f_1^{(r-s)}, f_2^{(s)}] \right), \quad (2.86)$$

with $r \geq 1$ being the order of a given equation. The solution of the zeroth order equation (2.85) is the well-known Jüttner distribution

$$f^{(0)}(x, p) = \frac{g}{(2\pi\hbar)^3} \left(\exp\left(\frac{p^\mu u_\mu(x) - \mu(x)}{T(x)}\right) + \delta \right)^{-1}, \quad (2.87)$$

where g is the degeneracy of the species, and $\delta = 0, \pm 1$, depending on whether Maxwell-Boltzmann, Bose-Einstein or Fermi-Dirac statistics should be used.

For the remainder of this discussion, we will focus on the specific case of the Bose-Einstein statistics, as it describes the case which will be of most use in the remainder of this thesis, namely, the pion gas at moderate to low temperatures. In this case, the collision term (2.78) takes the form

$$C[f_3, f_p] = \frac{g_3}{1 + \delta_{3,p}} \int d\Gamma_{12,3p} [f_1 f_2 (1 + f_3)(1 + f_p) - f_3 f_p (1 + f_1)(1 + f_2)], \quad (2.88)$$

with $1 + \delta_{3,p}$ being a factor to account for the indistinguishability of particles in the final state, and

$$d\Gamma_{12,3p} \equiv \frac{1}{2E_p} |T|^2 \prod_{i=1}^3 \frac{d\mathbf{k}_i}{(2\pi)^3 2E_i} (2\pi)^4 \delta^{(4)}(k_1 + k_2 + k_3 + p). \quad (2.89)$$

If we now look at the first order equation of (2.86), as an *ansatz* we parametrize the solution (with Bose-Einstein statistics) of $f_p^{(1)}$ such that

$$f_p^{(1)} = -f_p^{(0)}(1 + f_p^{(0)})\Phi(\mathbf{p}), \quad (2.90)$$

where $\Phi(\mathbf{p})$ is an appropriate function that will contain one or another hydrodynamic gradient, depending on the transport coefficient one wants to compute. Combining (2.88) and (2.90) and defining $\nu_p(x) \equiv f_p^{(0)}(x)$, we get

$$p^\mu u_\mu (Df_p)^{(1)} + p^\mu \nabla_\mu f_p^{(0)} = \frac{g}{2} \int d\Gamma_{12,3p} (1 + \nu_1)(1 + \nu_2) \nu_3 \nu_p \times (\Phi_p + \Phi_3 - \Phi_1 - \Phi_2). \quad (2.91)$$

One sees already in this last formula where the collision term has been linearized in terms of Φ_p one of the advantages of the Chapman-Enskog formalism, even only at first order: the left-hand side now only depends on derivatives of the equilibrium distribution, and thus does not depend on Φ_p .

Let us now take a closer look at the left hand side of the Boltzmann equation (2.83). To the first order⁵, and remembering that the distribution function is assumed to have a functional dependence on the hydrodynamic fields (2.81), we can write that

$$(Df_p)^{(1)} = \frac{\partial \nu_p}{\partial n} (Dn)^{(1)} + \frac{\partial \nu_p}{\partial T} (DT)^{(1)} + \frac{\partial \nu_p}{\partial u^\mu} (Du^\mu)^{(1)}, \quad (2.92)$$

where the functionals $(Dn)^{(1)}$, $(DT)^{(1)}$ and $(Du^\mu)^{(1)}$ can be obtained from conservation laws using the same ε expansion. They are given by

$$\begin{aligned} (Dn)^{(1)} &= -n \nabla_\mu u^\mu, \\ (DT)^{(1)} &= -\frac{T}{c_v} \nabla_\mu u^\mu, \\ (Du^\mu)^{(1)} &= \frac{1}{\varepsilon n + p} \nabla^\mu p, \end{aligned} \quad (2.93)$$

with the local energy density ε and pressure p defined in the same way as in the previous section (2.59), and where we defined the heat capacity per particle $c_v = \frac{\partial \varepsilon}{\partial T}$. Using the definition of the Jüttner distribution (2.87) and the newly found time derivatives (2.93), we rewrite the first order Boltzmann equation (2.86) as

$$\begin{aligned} p^\mu u_\mu p^\nu \left(\frac{\nabla_\nu T}{T} - \frac{\nabla_\nu p}{\varepsilon n + p} \right) + p^\nu T \nabla_\nu \frac{\mu}{T} - p^\mu p^\nu \left(\nabla_\mu u_\nu - \frac{1}{3} \Delta_{\mu\nu} \nabla_\sigma u^\sigma \right) + Q \nabla^\mu u_\mu \\ = C[f_1^{(1)}, f_2^{(0)}] + C[f_1^{(0)}, f_2^{(1)}] \end{aligned} \quad (2.94)$$

where μ is the chemical potential and

$$Q \equiv -\frac{1}{3} \Delta^{\mu\nu} p_\mu p_\nu + \frac{1}{c_v} (p^\mu u_\mu)^2 + \left(\frac{T^2}{c_v} \frac{\partial \mu}{\partial T} - n \frac{\partial \mu}{\partial n} \right) p^\mu u_\mu. \quad (2.95)$$

The left-hand side of Eq. (2.94) is now conveniently completely expressed in terms of various spatial gradients, which finally allows us to relate it to transport coefficients. Remembering the constitutive relations from the previous section for the shear (2.70) and bulk (2.72) viscosities, we see that this last equation contains terms which depend on exactly the same gradients. Thus, we see that the first 2 terms of the left-hand side of Eq. (2.94) are associated with the thermal conductivity, the third one with the shear viscosity and the last one with the bulk viscosity. What remains to be done to get expressions for these coefficients is to choose an appropriate form for the

⁵The reader can find the derivation of the solution at all orders in §1b of Chater 5 in [43].

previously introduced adimensional function Φ_p , such that one can then solve the system of equations numerically and obtain a value for the coefficients. As the author of these lines has not performed it directly, we will not be developing this calculation much further; instead we now give some insight as to the choices which then lead to the various coefficients of interest⁶. Note that higher orders give rise to more precise values for the coefficients, and as such most calculations are then done using a sufficiently high order of the expansion so that no appreciable difference remains from going to the next order.

2.2.1 Shear Viscosity

As previously mentioned, the third term of Eq. (2.94) is associated with the shear viscosity. More specifically, the shear-stress tensor is related to the viscosity via

$$\tau_{ij} = -2\eta \left(\nabla_\mu u_\nu - \frac{1}{3} \Delta_{\mu\nu} \nabla_\sigma u^\sigma \right). \quad (2.96)$$

The shear-stress tensor can be expressed in the first order Chapman-Enskog expansion such that

$$\tau_{ij} = g \int \frac{d^3 p}{(2\pi)^3} f_p^{(1)} \frac{p_i p_j}{E_p}. \quad (2.97)$$

Thus, choosing a Φ_p such that

$$\Phi_p = \beta^3 B_p^{ij} \left(\nabla_\mu u_\nu - \frac{1}{3} \Delta_{\mu\nu} \nabla_\sigma u^\sigma \right), \quad (2.98)$$

where B_p^{ij} is a function of the momenta p leads to a closed system of equations from which one can get the shear viscosity.

2.2.2 Bulk Viscosity

Similarly to the shear viscosity, the bulk viscosity stems directly from the fourth term of Eq. (2.94). The bulk viscosity is related to the trace of the shear-stress tensor

$$\tau_i^i = 3\zeta \nabla^\mu u_\mu. \quad (2.99)$$

At first order, this trace can be written such that

$$\tau_i^i = - \int d^3 p \frac{p^2}{E_p} f_p^{(1)}. \quad (2.100)$$

⁶See Chapter 5 in [43] and Chapters 2-5 in [75] for a more complete discussion.

Then, in an analogous way, we choose Φ_p to be of the form

$$\Phi_p = \beta A_p \nabla^\mu u_\mu, \quad (2.101)$$

with A_p once again an adimensional function of the momenta p . Solving the system of equations leads to the bulk viscosity.

2.2.3 Cross-Conductivity

The case of the cross-conductivity is (slightly) more involved, most notably because the various conductivities do not spring directly from the unperturbed Boltzmann equation but rather require external forces to be applied to it (i.e. the force term in Eq. (2.75) is now non-zero). We then apply a small uniform electrical field, which produces a force term of the form

$$qp_\nu \mathcal{F}^{\mu\nu} \frac{\partial}{\partial p^\mu} f_p, \quad (2.102)$$

where q is the charge of a given species. $F^{\mu\nu}$ can be written in terms of the electric field E^μ

$$F^{\mu\nu} = E^\mu u^\nu - E^\nu u^\mu, \quad (2.103)$$

for which E^μ is perpendicular to the velocity u^μ , and there are thus no time derivatives involved. The Boltzmann equation is written with the additional term as

$$p^\mu \frac{\partial f_p}{\partial x^\mu} + \frac{q}{T} n_p \Delta_\nu^\mu p_\mu E^\nu = C[f_p, f_3]. \quad (2.104)$$

We now remember the constitutive relation for electrical conductivity⁷ (2.31) and write the electric current in a similar form as we did the shear-stress tensor previously

$$j_Q = g \int \frac{d^3 p}{(2\pi)^3 E_p} p^i q f_p^{(1)}. \quad (2.105)$$

By choosing a Φ_p which is now proportional to the electric field E^μ rather than to some specific spatial gradient,

$$\Phi_p = \beta^3 Z_p \frac{E^\mu}{q}, \quad (2.106)$$

we now possess all the necessary tools to extract the various conductivities.

⁷The treatment is in all ways similar for the other parts of the cross-conductivity.

Chapter 3

Modeling the hadron gas: SMASH

Most of the results presented in this thesis depend in one way or another upon some form of modeling for the hadron gas. As mentioned in Chapter 1, this modeling role is taken in those instances by a relatively new transport approach, SMASH (Simulating Many Accelerated Strongly-interacting Hadrons). This model was described in depth [48], with further implementation details provided in topical follow-up articles [196–203]. The source code (in C++) is currently available under a free GPL distribution online [204]. These references are used throughout all sections of this chapter, and will for brevity not always be repeated.

In essence, SMASH as a transport approach keeps track of every particle in a given system, propagates them according to their equations of motion and allows them to interact with each other according to some predefined set of rules that determine whether a collision between 2 particles occurs or not, and what is produced out of the reaction. In some sense, it can be thought of as a very elaborate 3D pool table, which can help as a visualization tool for the reader to keep track of the numerous components of the model.

Although it is in principle possible to turn on inter-particle potentials in SMASH (for example the Skyrme potential between nucleons), this work will not make use of them, as their effect should be very small at the relatively low densities we consider (with respect to the nuclear density at which these potentials are expected to have a large impact). Thus all propagation of the particles in this work is strictly linear (in the geodesic sense of the term in some cases) between collisions with other particles.

3.1 Collision criterion

As they fly along their linear trajectories, particles are bound to encounter others with which they might interact. The decision to have a given set of particles (usually two, sometimes more) interact is called the collision criterion. Several such criteria exist in the literature, each with a set of advantages and inconvenients. The Kodama

criterion [205], for example, is perfectly covariant even in ultra-relativistic cases, but is computationally relatively intensive and not very intuitive. Stochastic rates [206–208] are another example which are numerically challenging and require a granularization of time (in the form of time steps, for example), but can in principle deal with multi-particle interactions. SMASH uses yet another criterion, usually called the geometric or UrQMD collision criterion [44], which is numerically much faster, although it has larger physical limitations. If the total cross-section between two particles is given by σ_{tot} , then a collision happens if the two corresponding hard spheres overlap:

$$d_{trans} \leq \sqrt{\frac{\sigma_{tot}}{\pi}}, \quad (3.1)$$

with d_{trans} the transverse distance between the particles

$$d_{trans}^2 = (\mathbf{r}_a - \mathbf{r}_b)^2 - \frac{((\mathbf{r}_a - \mathbf{r}_b) \cdot (\mathbf{p}_a - \mathbf{p}_b))^2}{(\mathbf{p}_a - \mathbf{p}_b)^2}, \quad (3.2)$$

where \mathbf{r} and \mathbf{p} are the three-positions and three-momenta of particles a and b in the center of mass frame of the collision. Once a collision has been confirmed, the time of the collision is taken to be the time of closest approach between the two particles in the computational frame:

$$t_{coll} = -\frac{(\mathbf{r}_a - \mathbf{r}_b) \cdot (\mathbf{p}_a/E_a - \mathbf{p}_b/E_b)}{(\mathbf{p}_a/E_a - \mathbf{p}_b/E_b)^2}, \quad (3.3)$$

with E the energy of a particle. In the case of an inelastic collision, the resulting outgoing particles are placed in the center of mass of the collision, and particles are simply given new momenta in the case of elastic collisions. The choice of the computational frame which we mentioned is important, since it determines the ordering of the collisions; as such, the geometric collision criterion is not covariant, although preliminary comparison with the Kodama criterion yielded un consequential differences. Another limitation is that this geometric criterion is only well-defined for binary collisions; high density systems where multi-particle interactions become important should thus be approached cautiously when using SMASH.

3.2 Initialization

There are currently four different modi which can be used to initialize a given simulation (or event) in SMASH:

1. Collider modus: Two nuclei fly towards each other in an effort to simulate a heavy ion experiment in a manner as similar as possible to what happens in real-life colliders;

2. Box modus: A predetermined set of hadrons are generated in a finite box with periodic boundary conditions;
3. Sphere modus: A predetermined set of hadrons are generated in a finite sphere with a permeable boundary;
4. List modus: A full list of initial positions, species, and four-momenta of particles is fed directly into SMASH; typical use would be as an afterburner after some hydrodynamic simulation and Cooper-Frye particlization [209, 210].

In this thesis we will be using exclusively the box and sphere modi, and as such will from now on exclusively describe and refer to those two initialization schemes.

The main difference between these two modes, as one would expect from the name, is in their initial boundary. The sphere mode has a spherical boundary at radius R which plays no further role in the subsequent event; its only function is to circumscribe a volume $\frac{4}{3}\pi R^3$ in which particles can be deposited. In the following simulation, particles are free to leave this initial volume, and we thus can study an expanding and cooling fireball of hadrons which eventually freezes out into free streaming. Additionally, the sphere modus allows to modify the metric from the default Minkowski metric to a Friedmann-Lemaître-Robertson-Walker (FLRW) expanding universe metric, which will prove useful in confirming the equivalence of SMASH with solutions of the Boltzmann equation in Section 3.3.

The box mode, on the other hand, has a cubic boundary of length L , which firstly serves, similarly to the sphere case, in delimiting a volume L^3 where particles are created, but also subsequently to keep all particles in the simulation inside this same box by enforcing periodic boundary conditions; this can be used for so-called “infinite matter” calculations, in which one simulates the behavior of some hadron gas¹ in a controlled environment where the energy density is conserved over the whole volume. Provided that detailed balance is enforced (see Section 3.5.4), a box simulation will over long periods attain some state of equilibrium; this will be discussed further in Section 3.6; precisely for this reason, the box modus will be used throughout Chapter 4 for all calculations involving the Kubo formalism.

Both initialization schemes initialize within their respective volume a number of particles $N = N_{test} \sum_i N_i$, where N_i is the initial number of particles of species i and N_{test} is the number of test particles². N_i can either be fed directly into SMASH or

¹This includes simpler versions such as the pion gas, or any otherwise specified combination of species; see Section 3.4.1 below for details.

²Test particles are a way of increasing locality in the collisions as well as smoothing out distribution functions by increasing statistics for spatial or phase-space density calculations; this is notably useful for calculations which use the previously mentioned inter-particle potentials. If $N_{test} > 1$, then all cross-sections in the simulation are scaled down, $\sigma \rightarrow \sigma N_{test}^{-1}$, so that the scattering rate remains the same. Some experimental observables require to reach saturation of test particles, but the calculation of transport coefficients is not one of them, as we will show in Fig. 4.5e. Except where explicitly

left to be calculated automatically according to the thermal expectation (allowing for Poissonian fluctuations) at a given temperature T and baryonic chemical potential μ_B , such that

$$N_i = \frac{g_i T^3}{2\pi^2} \exp\left(\frac{B_i \mu_B}{T}\right) \frac{m_i^2}{T^2} K_2\left(\frac{m_i}{T}\right), \quad (3.4)$$

where g_i is the degeneracy of a species, B_i its baryonic charge and m_i its pole mass. This last method for calculating initial multiplicities is used for all simulations in this thesis except where specifically noted otherwise, and will be referred to as “thermal multiplicities” in the following. The N particles are subsequently uniformly spatially distributed in the initial volume. Each particle is assigned a momentum for which the amplitude is sampled from the Boltzmann distribution³ at temperature T , and the direction is sampled uniformly:

$$w(\mathbf{p}) = W \exp\left(\sqrt{\mathbf{p}^2 + m^2}/T\right) p^2 dp \sin\theta d\theta d\phi, \quad (3.5)$$

where $w(\mathbf{p})$ is a probability to sample the momentum \mathbf{p} and W is a normalization factor. Although the ensemble average of the total momentum p_{tot} is zero, p_{tot} in any given event is not zero because of the sampling procedure. Thus, to obtain an immobile system the momenta of every particle j is adjusted according to $p_j \rightarrow p_j - p_{tot}/N$, and their energy is modified accordingly. This slightly affects the thermal distribution and can affect the temperature after equilibration, as will be discussed in Section 3.6.

Optionally, both modi offer the possibility of adding a single high energy particle in the middle of the considered volume⁴ in an effort to study the effects of a jet crossing a hadronic medium; Chapter 5 is entirely devoted to this case, and will make use of both the sphere and box initializations.

3.3 SMASH and the Boltzmann equation

Let us now make a small detour before continuing on with the description of more and more physical hadron gases. Specifically, we take a look back at the Boltzmann equation first discussed in Sections 1.1 and 2.2,

$$k^\mu \frac{\partial f_1}{\partial x^\mu} + m_1 \frac{\partial(\mathcal{F}^\mu f_1)}{\partial k^\mu} = C[f_1, f_2]. \quad (3.6)$$

Note that for consistency with [196] upon which this section is built, we exchanged the notation of the momentum p used in Chapters 1 and 2 to k . While it is beyond mentioned, $N_{test} = 1$ in the following chapters.

³Other initial distributions are also possible, but this one will be used throughout most of this thesis; see for example Eq. (3.12) for another off-equilibrium initialization.

⁴In the case of the box simulation, we let the reader ponder the philosophical implications of finding the middle of an infinite matter calculation.

the scope of this work to fully derive this equation, let us have another look at the previously introduced *Stosszahlansatz* which determine if the Boltzmann equation can be applied:

1. The system is dilute enough that only binary collisions are relevant, i.e. in any sub-region of space of the order of the collision range, there are never more than two particles. Those binary collisions can be elastic as well as inelastic.
2. The mean free path λ_{mfp} is much longer than the collision time; in other words, the interaction range is assumed to be short. This could be violated for example if a long-ranged Coulomb potential between particles was considered.
3. The incoming and outgoing particles of a binary collision are uncorrelated, that is, in terms of distribution functions,

$$f(t, \mathbf{x}_1, \mathbf{k}_1, \mathbf{x}_2, \mathbf{k}_2) \simeq f(t, \mathbf{x}_1, \mathbf{k}_1)f(t, \mathbf{x}_2, \mathbf{k}_2), \quad (3.7)$$

where \mathbf{x} and \mathbf{k} are the position and momenta of the interacting particles. This is known as the molecular chaos hypothesis.

If we now look back to our previous description of SMASH, we see that all three of those postulates are very often valid (if not always, in some cases). The first one is true as long as densities remain relatively low. The second is always true, as all interactions in SMASH are instantaneous (leading in some edge cases to locality problems as discussed previously). The last postulate is true as long as the system is large enough to contain enough sampled particles for the incoming and outgoing particles to have a very large heat bath to draw a “random” momentum from. Thus, in principle, if initialized using the same distribution function, SMASH and the Boltzmann equation should produce equivalent results, the only difference being that SMASH samples the distribution rather than using it directly. As such, transport models (this is in principle not limited to SMASH) can be thought of as Monte-Carlo solvers for the Boltzmann equation.

In order to verify this assertion, we need to define a system in which an analytic solution of the Boltzmann equation is known. Unfortunately, this turns out to be the exception rather than the rule, as most systems produce deeply non-linear solutions which do not have easy to compute analytic solutions. This problem was however recently solved in a very specific expanding-universe scenario [211, 212]. In a non-Minkovskian space-time, the Boltzmann equation becomes

$$k^\mu \frac{\partial f_1}{\partial x^\mu} + \Gamma_{\lambda\mu}^i k^\lambda k^\mu \frac{\partial f_1}{\partial k^\mu} = C[f_1, f_2], \quad (3.8)$$

where $\Gamma_{\lambda\mu}^i$ are the Christoffel symbols, and where we neglected any external potentials. The solution which has been found is valid only for massless particles interacting via

constant total cross-sections in a flat universe which expands according to a Friedmann-Lemaître-Robertson-Walker metric

$$ds^2 = dt^2 - a^2(t)(dx^2 + dy^2 + dz^2). \quad (3.9)$$

with the expansion factor $a(t)$ some monotonically increasing⁵ function of time. Physically, this scenario is quite similar to the expansion of the universe in the radiation-dominated era after the Big Bang. Under these conditions, the Boltzmann equation takes the reduced form

$$k^\mu u_\mu u_\nu \partial f(t, p) = C[f], \quad (3.10)$$

which is the equation which was solved by the authors of [211, 212]. They choose an expansion factor

$$a(t) = \sqrt{1 + \frac{b_r}{l_0} t}, \quad (3.11)$$

where $l_0 = 1/(\sigma n_0)$ is the mean free path at $t = 0$, σ is the constant cross-section and n_0 the initial particle density, and b_r is a parameter containing the density fraction of radiation in the universe; the ratio b_r/l_0 is in some sense a free parameter of the system for our purposes. For a far-from-equilibrium initial condition

$$f(t = 0, k) = \frac{256}{243} \frac{ka}{T_0} \lambda \exp\left(-\frac{4ka}{3T_0}\right), \quad (3.12)$$

where $\lambda = \exp(\mu_0/T_0)$ is the fugacity and T_0 is analogous to the initial temperature of the system (remember that temperature is not formally defined outside of equilibrium), the solution is

$$f(t, k) = \lambda \frac{\exp\left(-\frac{ka}{\kappa T_0}\right)}{\kappa^4(\tau)} \left[4\kappa - 3 + \frac{ka}{\kappa(\tau)T_0}(1 - \kappa(\tau))\right], \quad (3.13)$$

where $\kappa(\tau) = 1 - \exp(-\tau/6)/4$, and the transformed time $\tau = \int_{\hat{t}_0}^{\hat{t}} a^{-3}(\hat{t}') d\hat{t}'$ with $\hat{t} = t/l_0$. Using the previously introduced expansion factor (3.11), we get

$$\tau = \frac{2}{b_r} \left[1 - \left(1 + \frac{b_r}{l_0} t\right)^{-\frac{1}{2}}\right]. \quad (3.14)$$

Modifying SMASH to actually have a different metric than the Minkovski metric with which it was designed would be quite a task. However, if we assume the expansion to be slow enough, we can instead modify the propagation of particles from a flat metric to the previously discussed expanding-universe metric. If the expansion is slow, we

⁵It could in principle also be decreasing, but since this would lead to a contracting universe, the density of the system would increase very quickly, leading to the breakdown of some of the postulates for the validity of the solutions of the Boltzmann equation to be ensured.

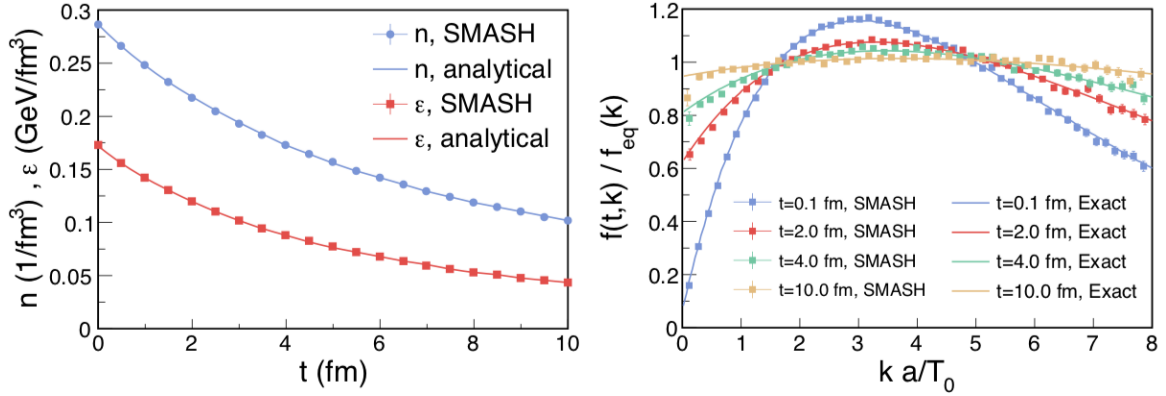


Figure 3.1: Time evolution of the particle and energy densities (left), and ratio of the distribution function over the equilibrium Boltzmann distribution versus a measure of the momentum $\frac{ka}{T_0}$. Both panels compare SMASH (dots) with the corresponding analytical expressions (solid lines). Taken from [196].

can granularize time and modify both the position and momenta (which decrease due to a $1/a(t)$ redshift) of every particle in the system at small regular time intervals, so that

$$x_i \rightarrow x_i + H(t), k_i \rightarrow k_i - H(t), \quad (3.15)$$

where k is the physical momentum in the computational frame (as opposed to the covariant momentum used in the previous equations), and $H(t) = \frac{\dot{a}(t)}{a(t)}$ is the Hubble parameter. Since all collisions are instantaneous and thus have a characteristic time much smaller than $H^{-1}(t)$, they do not feel the expansion of the universe and we can neglect any effect this factor might have on the scatterings.

To perform the comparison, we initialize a sphere of radius $r_0 = 50$ fm with $N = 1.5 \times 10^5$ massless particles. The ratio b_r/l_0 is fixed to 0.1 and the initial “temperature” $T_0 = 0.2$ GeV. Since the exterior of the sphere will immediately start to freeze-out, we only consider the particles located within a sub-sphere of radius $r_{\text{sub}} = a(t)r_0/1.5$. The particle and energy density in this subvolume can be calculated analytically [212] according to

$$n = \frac{\lambda_0 T_0^3}{\pi^2 a^3}, \quad \epsilon = \frac{3\lambda_0 T_0^4}{\pi^2 a^4}. \quad (3.16)$$

The left panel of Fig. 3.1 shows that even for a single event, SMASH’s results are in very good accordance with these formulas. The right panel compares the ratio of the distribution function $f(t, k)$ to the equilibrium distribution at $\lim_{\tau \rightarrow \infty} f(t, k) = f_{\text{eq}}(k) = e^{-\frac{ka}{T_0}}$, at computational times 0.1, 2, 4 and 10 fm; going to longer times would require using larger spheres, since the boundary freeze-out region gets larger with time. We see that the simulations and the analytical solution are very much in agreement, thus confirming our previous assertion that SMASH is equivalent in some regimes to a Monte Carlo solver for the Boltzmann equation.

3.4 Particle properties

3.4.1 Degrees of freedom

We now come back to the description of more physically accurate hadron gases. Section 3.2 mentioned that a certain number of particle species are initialized for every given event; the complete list of hadrons present in a full SMASH run and some of their most relevant properties can be found in Tables 3.1 and 3.2, and reflects the current knowledge of hadrons compiled in the 2018 version of the Particle Data Group Review [213]. The model assumes isospin symmetry, and as such each particle line in these tables corresponds to an isospin multiplet with degeneracy g (also counting anti-particles, which are implicitly included if a multiplet is used), with all particles in the multiplet having the same pole mass m_0 and pole width $\Gamma(m_0)$.

Non hadronic particles such as photons and dileptons are treated perturbatively by SMASH, but since they will not play any role in this work, we refer the reader to [198, 201] for more details.

3.4.2 Resonance widths, lifetimes and decays

All particles with a pole width smaller than 10 KeV (i.e. pions, η , kaons, nucleons, and Λ , Σ , Ξ and Ω baryons, as well as their respective anti-particles) are considered stable for the time frames of the simulations; all other particles are so-called “resonances” which propagate in the same way as their stable counterparts, but which will eventually decay into lighter particles.

SMASH uses the Manley-Saleski treatment to calculate decay widths [214]. Following this, a resonance R with mass m decaying into daughter particles a and b (themselves also possibly resonances) has a partial width

$$\Gamma_{R \rightarrow ab} = \Gamma_{R \rightarrow ab}(m_0) \frac{\rho_{ab}(m)}{\rho_{ab}(m_0)}, \quad (3.17)$$

where the function ρ_{ab} is defined as

$$\rho_{ab}(m) = \int dm_a dm_b \mathcal{A}_a(m_a) \mathcal{A}_b(m_b) \frac{|\mathbf{p}_f|}{m} B_L^2(|\mathbf{p}_f|R) \mathcal{F}_{ab}^2(m), \quad (3.18)$$

and the final-state momentum in the center-of-mass frame $|\mathbf{p}_f|$ is given by

$$|\mathbf{p}_f| = \frac{(m^2 - (m_a + m_b)^2)(m^2 - (m_a - m_b)^2)}{4m^2}, \quad (3.19)$$

with R the interaction radius, assumed to have a universal value of 1 fm. In Eq. (3.18) we also introduced the spectral function \mathcal{A} , the Blatt-Weisskopf functions B_L^2 and the

Unflavored Mesons	Mass (GeV)	Width (GeV)	g
π	0.138	0	3
$\pi(1300)$	1.30	0.4	3
$\pi(1800)$	1.812	0.208	3
η	0.548	0	1
η'	0.958	1.96e-4	1
$\eta(1295)$	1.294	0.055	1
$\eta(1405)$	1.409	0.051	1
$\eta(1475)$	1.476	0.085	1
ρ	0.776	0.149	3
$\rho(1450)$	1.465	0.400	3
$\rho(1700)$	1.720	0.25	3
σ	0.800	0.400	1
ω	0.783	8.49e-3	1
$\omega(1420)$	1.425	0.215	1
$\omega(1650)$	1.670	0.315	1
$f_0(980)$	0.990	0.060	1
$f_0(1370)$	1.35	0.35	1
$f_0(1500)$	1.507	0.109	1
$f_0(1710)$	1.723	0.139	1
$a_0(980)$	0.989	0.075	3
$a_0(1450)$	1.474	0.265	3
ϕ	1.019	4.25e-3	1
$\phi(1680)$	1.680	0.15	1
$h_1(1170)$	1.170	0.360	1
$b_1(1235)$	1.2295	0.142	3
$a_1(1260)$	1.23	0.42	3
f_2	1.276	0.187	1
$f_2'(1525)$	1.525	0.073	1
$f_2(1950)$	1.944	0.472	1
$f_2(2010)$	2.010	0.20	1
$f_2(2300)$	2.297	0.15	1
$f_2(2340)$	2.350	0.32	1
$f_1(1285)$	1.2819	0.0227	1
$f_1(1420)$	1.4264	0.054	1
$a_2(1320)$	1.3183	0.107	3
$\pi_1(1400)$	1.354	0.33	3
$\pi_1(1600)$	1.662	0.24	3
$\eta_2(1645)$	1.617	0.181	1
$\omega_3(1670)$	1.667	0.168	1
$\pi_2(1670)$	1.672	0.260	3
$\rho_3(1690)$	1.689	0.161	3
$\phi_3(1850)$	1.854	0.087	1
$a_4(2040)$	1.995	0.257	3
$f_4(2050)$	2.018	0.237	1

Strange Mesons	Mass (GeV)	Width (GeV)	g
K	0.494	0	4
$K^*(892)$	0.892	0.050	4
$K_1(1270)$	1.272	0.090	4
$K_1(1400)$	1.403	0.174	4
$K^*(1410)$	1.421	0.236	4
$K_0^*(1430)$	1.453	0.27	4
$K_2^*(1430)$	1.429	0.104	4
$K^*(1680)$	1.718	0.32	4
$K_2(1770)$	1.773	0.186	4
$K_3^*(1780)$	1.819	0.264	4
$K_2(1820)$	1.819	0.264	4
$K_4^*(2045)$	2.045	0.198	4

Nucleons	Mass (GeV)	Width (GeV)	g
N	0.938	0	4
$N(1440)$	1.440	0.350	4
$N(1520)$	1.515	0.110	4
$N(1535)$	1.530	0.150	4
$N(1650)$	1.650	0.125	4
$N(1675)$	1.675	0.145	4
$N(1680)$	1.685	0.120	4
$N(1700)$	1.720	0.200	4
$N(1710)$	1.710	0.140	4
$N(1720)$	1.720	0.250	4
$N(1875)$	1.875	0.250	4
$N(1880)$	1.880	0.400	4
$N(1895)$	1.895	0.120	4
$N(1900)$	1.900	0.200	4
$N(1990)$	1.990	0.500	4
$N(2060)$	2.100	0.400	4
$N(2080)$	2.000	0.350	4
$N(2100)$	2.100	0.260	4
$N(2120)$	2.120	0.300	4
$N(2190)$	2.180	0.400	4
$N(2220)$	2.220	0.400	4
$N(2250)$	2.250	0.470	4

Delta Baryons	Mass (GeV)	Width (GeV)	g
Δ	1.232	0.117	8
$\Delta(1620)$	1.610	0.130	8
$\Delta(1700)$	1.710	0.300	8
$\Delta(1900)$	1.860	0.250	8
$\Delta(1905)$	1.880	0.330	8
$\Delta(1910)$	1.900	0.300	8
$\Delta(1920)$	1.920	0.300	8
$\Delta(1930)$	1.950	0.300	8
$\Delta(1950)$	1.930	0.280	8

Table 3.1: List of particles and their properties present in SMASH v1.6. The mass and width columns correspond to the pole mass and width.

Lambda Baryons	Mass (GeV)	Width (GeV)	g
Λ	1.116	0	2
$\Lambda(1405)$	1.405	0.0506	2
$\Lambda(1520)$	1.520	0.0156	2
$\Lambda(1600)$	1.600	0.1500	2
$\Lambda(1670)$	1.670	0.0350	2
$\Lambda(1690)$	1.690	0.0600	2
$\Lambda(1800)$	1.800	0.3000	2
$\Lambda(1810)$	1.810	0.1500	2
$\Lambda(1820)$	1.820	0.0800	2
$\Lambda(1830)$	1.830	0.0950	2
$\Lambda(1890)$	1.890	0.1000	2
$\Lambda(2100)$	2.100	0.2000	2
$\Lambda(2110)$	2.110	0.2000	2
$\Lambda(2350)$	2.350	0.1500	2

Omega Baryons	Mass (GeV)	Width (GeV)	g
Ω^-	1.672	0	2
$\Omega(2250)^-$	2.252	0.055	2

Sigma Baryons	Mass (GeV)	Width (GeV)	g
Σ	1.189	0	6
$\Sigma(1385)$	1.385	0.036	6
$\Sigma(1660)$	1.660	0.100	6
$\Sigma(1670)$	1.670	0.060	6
$\Sigma(1750)$	1.750	0.090	6
$\Sigma(1775)$	1.775	0.120	6
$\Sigma(1915)$	1.915	0.120	6
$\Sigma(1940)$	1.940	0.220	6
$\Sigma(2030)$	2.030	0.180	6
$\Sigma(2250)$	2.250	0.100	6

Xi Baryon	Mass (GeV)	Width (GeV)	g
Ξ	1.318	0	4
$\Xi(1530)$	1.533	0.009	4
$\Xi(1690)$	1.690	0.030	4
$\Xi(1820)$	1.823	0.024	4
$\Xi(1950)$	1.950	0.060	4
$\Xi(2030)$	2.025	0.020	4

Table 3.2: Continued from Table 3.1.

form factor \mathcal{F}_{ab} ; let us now briefly discuss each of those.

The spectral function of a resonance is in general a probability distribution for this particle to have a specific mass. Although it can in principle depend on quantities such as the temperature and density of a system, these medium modifications are currently neglected (for similar reasons as what was discussed in the previous section, e.g. the assumed diluteness of the system). All resonances in SMASH follow the relativistic Breit-Wigner distribution

$$\mathcal{A}(m) = \frac{2\mathcal{N}}{\pi} \frac{m^2\Gamma(m)}{(m^2 - m_0^2)^2 + m^2\Gamma^2(m)}, \quad (3.20)$$

where \mathcal{N} is a normalization factor calculated from $\int_0^\infty \mathcal{A}(m)dm = 1$ (as a corollary, note that if a particle has width zero, the integration over the spectral function collapses to a δ function). The total width can be divided in a sum of partial widths for every possible decay channel; at the pole mass, the width $\Gamma_0 = \Gamma(m_0)$ can be decomposed exactly into the different processes according to the so-called branching ratios $\Gamma_i(m)/\Gamma(m)$, where i denotes an individual decay channel, i.e. the fraction of the total width originating from the different processes (see Fig. 3.2, for example). Note that each process has a minimum mass corresponding to the sum of the pole masses of the daughter particles.

The form of the Blatt-Weisskopf functions [215] depend on the orbital angular

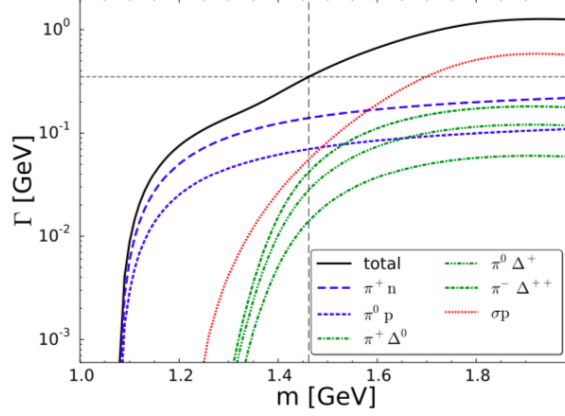


Figure 3.2: Individual contribution of the various processes to the total $N(1440)$ resonance width. The vertical and horizontal dashed lines correspond respectively to the pole mass and pole width. Taken from [48].

Decay type	λ (GeV)
$\pi\rho$	0.8
one unstable meson (e.g. ρN)	1.6
one unstable baryon (e.g. $\pi\Delta$)	2.0
two unstable daughters (e.g. $\rho\rho$)	0.6
two stable daughters (e.g. $\pi\pi$)	∞

Table 3.3: Cut-off parameter λ in Eq. (3.23). Adapted from [48].

momentum L of daughters a and b ; it is given by

$$B_L^2(x) = \frac{x^{2L}}{|g_L|^2}, \quad (3.21)$$

where g_L is given by the recursion relation [216]

$$g_{L+1} = (2L + 1)g_L - x^2 g_{L-1}, \quad (3.22)$$

with the two first expressions being $g_0 = 1$ and $g_1 = 1 - ix$.

The form factor \mathcal{F}_{ab} was not part of the initial Manley-Saleski formalism, but was rather subsequently added in one of the precursors of SMASH, GiBUU [45], since it helped improve the description of heavy ion experimental data. It only has an effect when one or both daughter particles are themselves resonances, and is given by

$$\mathcal{F}_{ab} = \frac{\lambda^4 + 1/4(s - m_0^2)^2}{\lambda^4 + (m^2 - 1/2(s + m_0^2))^2}, \quad (3.23)$$

where we used the Mandelstam variable $s = (p_a + p_b)^2$. The factor λ , following [45], takes the values given in Table 3.3.

Now that we have properly described the width of resonances, we can also de-

fine their lifetime as the inverse total decay width $\tau = 1/\Gamma(m)$. This leads to an exponential probability to decay $P(\text{decay at } t) = \exp(-t/\tau)$; in SMASH, we sample this probability at the creation of the resonance to determine the moment at which it will decay. If it still exists when that time comes (i.e. if it has not collided inelastically with some other particle in between), a decay channel is randomly chosen from the allowed channels according to its off-shell branching ratios $\Gamma_i(m)/\Gamma(m)$, and the daughter particles are created in place of the resonance with appropriate masses and momenta (see Sec. 3.5.5). Note that the channels are conveniently listed in an input file and can easily be modified or turned on and off individually⁶; this will be of use in Section 3.6 and throughout Chapter 4. Let us further comment that the fact that resonances propagate in a transport approaches such as SMASH is not trivial, as this separates it from most approaches that try to directly use the Boltzmann equation. In the latter, it becomes much more complicated to deal with propagating resonances, since they do not have a fixed mass; while not impossible, one in principle then needs to properly implement spectral functions into the propagation terms of the equation; this was notably done in PHSD [46]. This difference between the approaches will have very important consequences on the calculation of some of the transport coefficients which will be the subject of Chapter 4.

3.5 Scatterings

The last core part of the model which remains to be discussed are inter-particle scatterings, or, more specifically, how the cross-sections necessary for the application of the collision criterion (3.1) are obtained, and what these scatterings produce.

3.5.1 $2 \rightarrow 1$ processes

The first type of scattering is essentially the reverse process to the resonance decay which was discussed in the previous section, i.e. the resonance formation. The cross-section for such $2 \rightarrow 1$ processes is also inspired from GiBUU [45]:

$$\sigma_{ab \rightarrow R}(s) = \frac{2J_R + 1}{(2J_a + 1)(2J_b + 1)} \mathcal{S}_{ab} \frac{2\pi^2}{\mathbf{p}_i^2} \Gamma_{ab \rightarrow R}(s) \mathcal{A}_R(\sqrt{s}), \quad (3.24)$$

where J is the spin of a particle, \mathcal{S}_{ab} is a symmetry factor (worth 2 if a and b are of the same species, and 1 otherwise) and \mathbf{p}_i is the center-of-mass momentum of the initial particles, calculated in exactly the same way as previously in Eq. (3.19). The so-called “in-width” $\Gamma_{ab \rightarrow R}$ is closely related to the previously discussed “out-width” $\Gamma_{R \rightarrow ab}$, with the only difference coming from the fact that in the out-width, one has

⁶See [204] for a full list of the pole mass branching ratios $\Gamma_i(m_0)/\Gamma(m_0)$

to integrate over the possible mass of potential resonant daughters, whereas this mass is already known in a scattering involving an existing resonance. Thus, the in-width is written as

$$\Gamma_{ab \rightarrow R} = \begin{cases} \Gamma_{R \rightarrow ab}, & \text{if incoming particles stable,} \\ \Gamma_{R \rightarrow ab}^0 \frac{|\mathbf{p}_{ab}| B_L^2(|\mathbf{p}_{ab}| R) \mathcal{F}_{ab}(m)}{m \rho_{ab}(m_0)}, & \text{otherwise.} \end{cases} \quad (3.25)$$

where $m = \sqrt{s}$ is the mass of the potential resonance. When a collision happens, a resonance is formed halfway between the two scattering particles with the appropriate mass and momentum.

3.5.2 Elastic collisions

There are in SMASH three types of elastic processes. The first one, used to describe low energy meson-meson and meson-baryon interactions, is through intermediate resonance formation and decay (e.g. $\pi\pi \rightarrow \rho \rightarrow \pi\pi$), and has already been discussed in the previous sections.

The second one is a direct $2 \rightarrow 2$ process used for specific interactions, in which fully parametrized cross-sections are used. Specifically, elastic parametrizations for nucleon-nucleon [217], nucleon-antinucleon [44], and all possible kaon-nucleon [45] interactions, as well as their anti-particle equivalents, are implemented⁷. When such a process occurs, both particles keep their position and new momenta are sampled in the center-of-mass frame.

The last type of elastic process is very similar to the previous one, but is extended to all combinations of particles; it will be further discussed when we introduce the Additive Quark Model in section 3.5.7.

3.5.3 Inelastic $2 \rightarrow 2$ processes

SMASH also features a certain number of hardcoded inelastic binary processes; they can be separated in the following subgroups:

1. Single and double nucleon excitation reactions: $NN \rightarrow N\Delta$, $NN \rightarrow NN^*$, $NN \rightarrow N\Delta^*$, $NN \rightarrow \Delta\Delta$, $NN \rightarrow \Delta N^*$ and $NN \rightarrow \Delta\Delta^*$, where the $*$ notation refers to excitations of the nucleon and Δ baryon,
2. Strangeness and charge exchange reactions: $KN \rightarrow KN$, $KN \rightarrow K\Delta$, $K^-N \rightarrow \pi\mathcal{Y}$, where \mathcal{Y} is a Λ , Σ or Ξ baryon,

⁷One should in principle also add to this list the deuteron-pion [199] and deuteron-nucleon [218] parametrizations, but since deuterons are not present in the default SMASH simulations (as showcased by their absence in Tables 3.1 and 3.2) and will not play a role in the remainder of this thesis, we invite the reader to refer to those publications for further details; reference [199] also contains all inelastic deuteron-related reactions in SMASH.

Process	$A_{I=1}$	$A_{I=0}$
$NN \rightarrow NN(1535)$	4.5	91
$NN \rightarrow NN^*$	4.5	14
$NN \rightarrow N\delta^*$	15	-
$NN \rightarrow \Delta\Delta$	45	120
$NN \rightarrow \Delta N^*$	7	-
$NN \rightarrow \Delta\Delta^*$	15	25

Table 3.4: Parameters for matrix elements; the $N(1535)$ gets a higher matrix element to describe the increased η production in [220]. Updated from [48].

3. Resonant nucleon-antinucleon annihilation: $\bar{N}N \rightarrow h_1(1170)\rho$.

The nucleon excitation cross-sections can be expressed in a similar form to what we had in the $2 \rightarrow 1$ case,

$$\sigma_{ab \rightarrow cd} = \frac{(2J_c + 1)(2J_d + 1)}{s|\mathbf{p}_i|} \cdot \sum_I (C_{ab}^I C_{cd}^I)^2 \cdot \frac{|\mathcal{M}|_{ab \leftrightarrow cd}^2(s, I)}{16\pi} \cdot \int \mathcal{A}_c(m_c) \mathcal{A}_d(m_d) |\mathbf{p}_f| (\sqrt{s}, m_c, m_d) dm_c dm_d, \quad (3.26)$$

with C the Clebsch-Gordan factors coupling initial and final state to an isospin I , and $|\mathcal{M}|^2$ the matrix element of the elementary reaction. Here we assume that $|\mathcal{M}|^2$ is independent of the angle of the collision. SMASH uses the one-boson-exchange model [219] for the $NN \rightarrow N\Delta$ reaction,

$$\frac{|\mathcal{M}|^2}{16\pi} = \frac{A}{2(\sqrt{s} - B)^C}, \quad (3.27)$$

where the parameters have the values $A = 68$, $B = 1.104$ GeV and $C = 1.951$. For all other nucleon processes, similarly to what is done in UrQMD [44], a parametrization depending on isospin and the masses of the products is used,

$$\frac{|\mathcal{M}|^2}{16\pi} = \frac{A_I}{2(m_c^2 + m_d^2)}, \quad (3.28)$$

where the value of A_I is given in Table 3.4.

Although it would in principle be possible to use Eq. (3.26) to get cross-sections for the strangeness-related reactions, we make use of the fully parametrized cross-sections which are available for these processes. The charge exchange reactions $KN \rightarrow KN$ follow the framework of GiBUU [45], whereas the hyperon reactions $K^-N \rightarrow \pi\mathcal{Y}$ are based on recent expansions in the strangeness production sector of the UrQMD model [221] and the corresponding experimental cross-sections [222].

Finally, SMASH includes an optional feature that allows for nucleon and anti-

nucleons to annihilate using only resonances, and not via string excitation, as is typically the case [44, 45, 223–226] (see Section 3.5.6 for the usual treatment). As will be discussed in Section 3.6, this is a useful feature in infinite matter calculations. Using an appropriately parametrized cross-section taken from UrQMD [44], we rely on the fact that on average, nucleon-antinucleon annihilation produces 5 pions, as suggested in [227]. Thus we implement the following reaction:

$$\bar{N}N \leftrightarrow h_1(1170)\rho \quad (3.29)$$

In SMASH, the ρ resonance decays exclusively to $\pi\pi$ and the $h_1(1170)$ resonance decays to $\pi\rho$. We then get, after resonance decays, 5 pions from every $\bar{N}N$ interaction. This process is reversible in all steps and we recover detailed balance for nucleon-antinucleon annihilation (see 3.5.4).

3.5.4 Detailed balance

In general, diagram calculations in QCD tell us that a given reaction and its associate counterreaction have the same matrix element; this is one of multiple ways one can define the concept of detailed balance. Although we did not mention it directly at the time, detailed balance is what relates the out-width of a resonance decay to the cross-section of it's associated resonance formation. In the case of inelastic $2 \rightarrow 2$ processes, it relates the forward and backward cross-sections, and can be written as

$$\begin{aligned} \frac{\sigma_{ab \rightarrow cd}}{\sigma_{cd \rightarrow ab}} &= \frac{(2J_c + 1)(2J_d + 1) \mathcal{S}_{ab} |\mathbf{p}_f|(\sqrt{s}, m_c, m_d)}{(2J_a + 1)(2J_b + 1) \mathcal{S}_{cd} |\mathbf{p}_i|(\sqrt{s}, m_a, m_b)} \\ &\times \frac{|\mathbf{p}_f|(\sqrt{s}, m_c, m_d) \int \mathcal{A}_c(m_c) \mathcal{A}_d(m_d) |\mathbf{p}_f|(\sqrt{s}, m_c, m_d) dm_c dm_d}{p_i^2(\sqrt{s}, m_a, m_b)}. \end{aligned} \quad (3.30)$$

This expression is valid for all previously discussed binary processes, and is used throughout SMASH to obtain all reverse cross-sections.

3.5.5 2-particle final state

Once a process that produces two particles is underway, be it a decay or a binary collision, a so-called final state has to be determined using the predetermined produced particle properties and the available phase space. The way this happens is numerically non-trivial, and so we provide here an overview.

First, the mass of the products have to be determined. If both are stable, their mass is fixed and nothing needs to be done. If one of the products is a resonance, its

mass is sampled according to

$$F(m) = \begin{cases} \mathcal{A}(m)|\mathbf{p}_f|(\sqrt{s}, m, m_{stable})B_L^2(|\mathbf{p}_f|R), & \text{for resonance decays,} \\ \mathcal{A}(m)|\mathbf{p}_f|(\sqrt{s}, m, m_{stable}), & \text{for binary interactions,} \end{cases} \quad (3.31)$$

where m_{stable} is the known mass of the stable product, and the possible mass of the final resonance ranges from m_{min} to $\sqrt{s} - m_{stable}$. If both outgoing particles are resonances, their masses have to be sampled simultaneously from

$$F(m_1, m_2) = \begin{cases} \mathcal{A}(m_1)\mathcal{A}(m_2)|\mathbf{p}_f|(\sqrt{s}, m_1, m_2)B_L^2(|\mathbf{p}_f|R), & \text{for resonance decays,} \\ \mathcal{A}(m_1)\mathcal{A}(m_2)|\mathbf{p}_f|(\sqrt{s}, m_1, m_2), & \text{for binary interactions.} \end{cases} \quad (3.32)$$

Note that the different cases presented in Eqs. (3.31) and (3.32) simply correspond to the integrands of Eqs. (3.18) and (3.26).

Once both masses are known, momenta can be distributed among the outgoing particles. For resonance decays, this is always done isotropically in the center-of-mass frame. For binary collisions, it can either be performed according to the same isotropic picture, or according to some anisotropic parametrizations following Cugnon et al. [228]. Although these anisotropic distributions are important to reproduce some experimental data, we will in the next chapters be neglecting them to conserve detailed balance (see Section 3.6).

Note that in principle SMASH can also deal with 3-particle final states, but since this feature will not be used in this thesis, we shall not detail it further.

3.5.6 Strings

Strings are a way to model high energy collisions between quarks and hadrons. In essence, a string excitation gets formed when two particles interacting strongly start moving away from each other, creating a color flux tube between them. This tube, or string, if it has enough energy, will eventually break somewhere in the middle and create a (di)quark-anti(di)quark pair, thus separating the string into two strings. As long as the energy (sometimes also referred to as mass) of the string is sufficient, this can happen any number of times, thus potentially creating many quarks and anti-quarks which subsequently form hadrons, in a process called the string fragmentation. The following discussion is based in great part on [203], we refer the reader to it for more information.

3.5.6.1 Excitation

In SMASH, several types of string are treated in different ways, all of which use PYTHIA (v8.235) to some extent [229, 230]. Specifically, we differentiate between

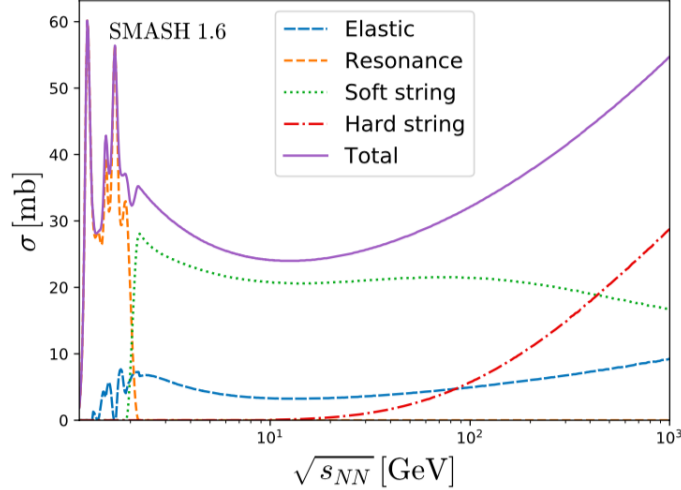


Figure 3.3: π^- -p cross-section at all center-of-mass energies. The total cross-section is split into the contributions coming from various channels. Taken from [203].

hard and soft strings. Hard strings arise directly from partonic interactions present in pQCD calculations, and are based on the p_T -ordered multiparton interaction framework [231]; once a hard string process has been selected by SMASH, it is fully handled by PYTHIA. In the intermediate region where the energy is too large for resonance formation but too low for pQCD strings (see Fig. 3.3), the so-called soft strings come as a phenomenological model to fill the gap. Soft strings are excited directly within SMASH, which essentially means that their mass, three-momentum p_{CM} , longitudinal momentum p_{\parallel} and transverse momentum p_{\perp} are calculated directly in the model, before being fed to PYTHIA for the fragmentation of the string.

Following UrQMD [44, 232], we then differentiate between four processes:

1. **Single diffractive soft strings:** In a single diffractive process, one of the two incoming hadrons is excited into a string X , i.e. by separating into a quark-diquark string:

$$A + B \rightarrow A + X \quad \text{or} \quad A + B \rightarrow X + B.$$

2. **Double diffractive soft strings:** In a double diffractive process, after a momentum exchange via one or more gluons between the two hadrons, both initial hadrons are excited into strings, i.e. form a quark-diquark string:

$$A + B \rightarrow X_A + X_B.$$

3. **Non diffractive soft strings:** In a non-diffractive soft string, the hadrons exchange a valence quark which carries a fraction of the longitudinal momentum

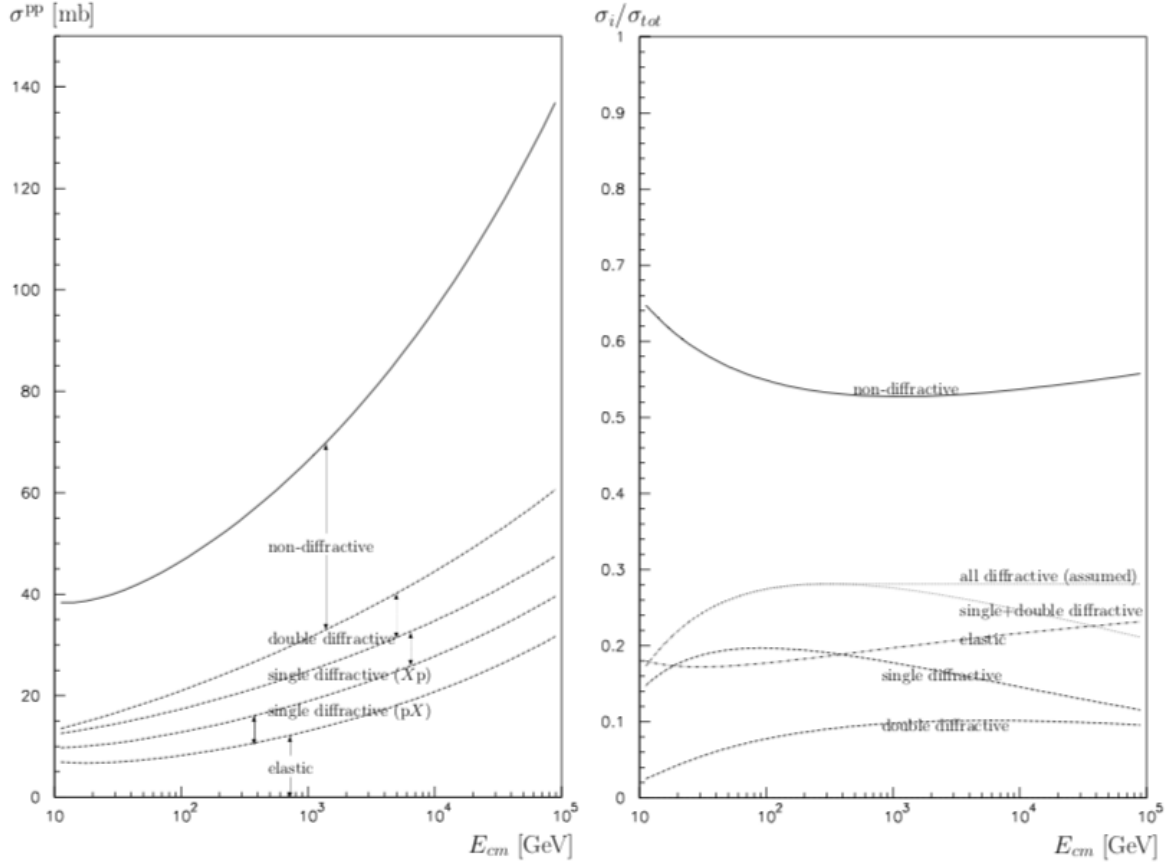


Figure 3.4: Left: Proton-proton cross-section at high energies with the various contributions of the subprocesses highlighted. Right: Relative contributions of the subprocesses to the total. Taken from [233].

of their original hadron, a string is formed from each thus modified hadron:

$$A + B \rightarrow X_1 + X_2.$$

4. **Non diffractive hard strings:** Finally, non-diffractive hard strings are direct pQCD quark-quark interactions which are only possible at the highest energies; there can in principle be as many strings produced as there are quark pairs present:

$$A + B \rightarrow X + \dots$$

Additionally, we note that the treatment of baryon-antibaryon annihilations does not fit within this framework. In this case, still following [44, 232], one (anti)quark from each incoming hadron is selected to annihilate with the other. The remaining components are separated into two mesonic strings, each with half of \sqrt{s} .

3.5.6.2 Cross-sections

Figure 3.3 shows the total cross-section of pion-proton scatterings; at high energy, the relevant contributions are exclusively coming from strings and elastic processes⁸. Since the total and elastic cross-sections are known experimentally and have high-energy parametrizations (at least for πN , NN and $\bar{N}N$; see Section 3.5.7 for all other cases), we can determine the inelastic contribution from

$$\sigma_{inel} = \sigma_{tot} - \sigma_{el}. \quad (3.33)$$

This inelastic cross-section can then be divided between the various previously described subprocesses (see Fig. 3.4). Specifically, the single-diffractive and double-diffractive cross-sections are known from [233], and the hard non-diffractive cross-section from pQCD can be used to divide the remaining part of the inelastic cross-section between soft and hard non-diffractive processes.

Once again, the case of baryon-antibaryon annihilations is somehow distinct. Since the total and elastic cross-sections are known and only one process exists in this case, then the full inelastic cross-section can be assigned to it according to (3.33).

3.5.6.3 Fragmentation and particle formation

Once the process is selected according to the previously discussed cross-sections and excited in the appropriate manner, a string is fragmented into hadrons using PYTHIA. Internally, the species of the produced hadrons are determined from the flavor of the (di)quark-anti(di)quark which are produced. Note that some empirical suppression factors are used for heavier quasi-particles. Each hadron then samples a longitudinal momentum from the symmetric Lund fragmentation function [229]

$$f(z) \propto \frac{1}{z}(1-z)^a \exp\left(-b\frac{m_T^2}{z}\right), \quad (3.34)$$

where z is a momentum fraction, m_T is the transverse mass of the hadron, and a and b are free parameters ($a = 0.2$ and $b = 2 \text{ GeV}^{-2}$ for leading baryons, and $a = 2$ and $b = 0.55 \text{ GeV}^{-2}$ for internal baryons).

Although all hadrons are instantly created in SMASH, in a dynamical picture the pair production does not happen simultaneously. As shown on Fig. 3.5, the different (di)quarks and anti(di)quarks each follow their own trajectory in the light cone. Additionally, the different string fragments which are depicted take some approximately constant proper time to recombine. To simulate this effect, we scale down all cross-sections of the newly formed hadrons by a factor which gradually increases. After a

⁸Note that a special treatment has to take place in the transition region between resonances and strings, see Sec. 3.5.8.

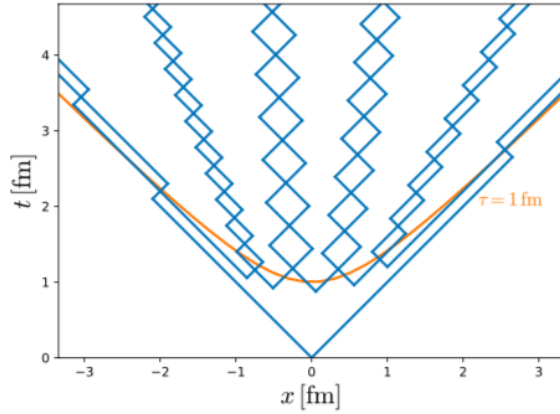


Figure 3.5: Picture of the string fragmentation in the yo-yo model. Taken from [203].

constant proper time (for simplicity) of $\tau = 1$ fm, the cross-sections of all produced hadrons are back to their nominal values.

3.5.7 Additive Quark Model

The alert reader will have noted that the previously discussed processes, while numerous, do not encompass the full combinatorics of all possible binary collisions between the different species listed in tables 3.1 and 3.2, because it is highly non-trivial to obtain experimental cross-sections for such reactions. The Additive Quark Model (AQM) [234] is an empirical prescription for the prediction of the cross-sections of such processes. The AQM cross-section for any reaction is written as

$$\sigma^{AQM} = 40 \cdot \left(\frac{2}{3}\right)^{n_M} \cdot (1 - 0.4x_i^s) \cdot (1 - 0.4x_j^s), \quad (3.35)$$

where n_M is the number of colliding mesons and x_i^s is the ratio of strange to non-strange quarks in the i -th incoming hadron. Following what is done in UrQMD [44], we then use this AQM cross-section as a scaling factor to known and physically related cross-sections. For example, all meson-baryon interactions between particle species i and j can be scaled from the known πp cross-section $\sigma_{\pi p}$, such that

$$\sigma_{ij} = \frac{\sigma_{ij}^{AQM}}{\sigma_{\pi p}^{AQM}} \sigma_{\pi p}. \quad (3.36)$$

Specifically, in SMASH, elastic and total cross-sections are scaled according to the contents of Table 3.5.

When an AQM process is selected, it either produces an elastic scattering as described in Section 3.5.2, or a string similar to what was done in Section 3.5.6. In the case of the string excitation, since PYTHIA can only handle collisions between pions and nucleons, a way of mapping an arbitrary hadron to either of those recognized

Process	Total	Elastic
Baryon-Antibaryon, same species	$\bar{p}p$	$\bar{p}p$
Baryon-Antibaryon, diff species	$\bar{n}p$	$\bar{p}p$
Baryon-Baryon, same species	pp	pp
Baryon-Baryon, diff species	np	pp
Meson-Baryon	π^-p	π^+p
Meson-Meson	π^+p	π^+p

Table 3.5: Cross-section scaling for AQM processes.

cases was implemented, both for the excitation and fragmentation steps of the string routine. Specifically, all baryons with a positive electric charge are mapped onto a proton, and others are matched to a neutron. Mesons with a positive or vanishing charge are mapped to a π^+ , and other to a π^- . Before the final fragmentation into hadrons within PYTHIA, light (anti)quarks are swapped to their original flavor⁹ and momenta of all particles are rescaled to reflect the mass difference, thus conserving energy and all quantum numbers.

3.5.8 Transition region

As can be seen on Fig. 3.3, there exists a certain region in which strings and resonances both have contributions to the total cross-section. This is known as the transition region, and needs to be treated as a special case, since the contributions from the resonances are not implemented in the string model (see Sec. 3.5.6.2). Explicitly, we define a transition energy window in which the cross-sections of both regimes are linearly scaled down (with the resonances gradually losing their contribution while strings are gaining theirs). In general, this window is 1 GeV wide and starts at an energy corresponding to the sum of the masses of the incoming particles plus 0.9 GeV. In order to protect the calibrated existing low-energy cross-sections, special treatments include:

1. πN , from 1.9 to 2.2 GeV,
2. NN, from 4 to 5 GeV,
3. $\pi\pi$ from 1.12 to 2.12 GeV,
4. KN, from 15.15 GeV to 16.15 GeV.

⁹If no appropriate quark can be found due to annihilation processes, a gluon is split into the desired pair.

3.6 Equilibrium and thermodynamics in SMASH

In this section we describe how we define and achieve equilibrium within SMASH, and how to extract thermodynamic quantities from such a state.

In the following chapters, a system will be considered in equilibrium if a steady state (allowing for fluctuations) is achieved over long periods in terms of its chemical composition (i.e. the multiplicity ratios of different particle species remain constant on average) and in terms of its momentum distribution (i.e. a constant temperature can be observed). Many of the main results shown in this thesis, i.e. the calculation of the transport coefficients according to the Green-Kubo formalism as presented in Chapter 2, require that this equilibrium be strictly enforced over very long periods (several hundred fm/c); thus, the only initialization scheme in which SMASH can produce such a steady state is the box calculation described in Section 3.2, since it is the only one that still conserves energy density over this kind of time frame. In order for a stable state to be reached in the box, only processes which respect the principle of detailed balance (see Sec. 3.5.4) can be allowed to take place. This immediately rules out all string excitations, as well as three-body decays and $2 \rightarrow 3$ processes, since the geometric criterion simply cannot deal with the reverse reactions of those processes. It should also be mentioned that all electro-weak decays (of which there are not many, and all of which have rather small branching ratios) should be turned off in the list of allowed decays. Finally, all angular distributions for binary processes must be isotropic, as the anisotropic mode of SMASH currently does not adapt the incoming cross-section of such collisions in a consistent way with how the final state is created; in this sense we conserve the symmetry between the isotropy of the geometric criterion and that of the final state rather than introducing angular distributions (even though it is expected that these could have an effect on transport coefficients, as will be discussed in Section 4.2.3).

As we just discussed, in complex systems where inelastic collisions are present, the chemical composition of the system, its temperature and the chemical potential can change from the initial state if this one is not directly equilibrated. This is indeed almost never the case, except for the very simplest systems, since many numerical and physical effects can contribute to having a system which is close to but not quite in equilibrium. These effects include:

1. The expectation value of the initial thermal multiplicity is typically a fractional number. Since SMASH only deals with integer numbers of particles, this can introduce some biases, especially for rare heavy particles;
2. Resonance multiplicities have to be initialized according to a specific mass, which is chosen to be their pole mass; this pole mass might however be different from their average mass at a given temperature, thus creating either too many or too

few of a specific resonance species on average;

3. The process by which a given event is made immobile discussed in Section 3.2 (i.e. $p_{tot} = 0$) involves slightly modifying all particles' momenta, which has the additional effect of modifying the thermal distribution;
4. Imperfections in the detailed balance of specific reactions (for example due to a numerical maximum distance of interaction, or similar) can lead to reactions which are favored in one direction or the other, skewing the multiplicities of their participants;
5. Poissonian sampling of multiple members of a same multiplet can yield different numbers of particles; for example, in a given event more π^+ than π^- could be created, again leading to slightly skewed dynamics (this last effect is mostly negligible for systems with many species, but could be more significant in simpler ones).

One thus needs a way to calculate the actual values of these thermodynamic quantities in the system after equilibration. The temperature is obtained by fitting momentum distributions of given particle species:

$$\frac{dN}{dp} \propto p^2 e^{-\frac{\sqrt{p^2+m^2}-\mu}{T}} . \quad (3.37)$$

Note that the extracted temperatures differ slightly from one species to the next. It is therefore necessary to distinguish between the temperature of a particle species and the temperature of the system. In concrete terms, we consider the temperature of the system to be the weighted average of the most abundant stable particles in any system (in the case of the full hadron gas used throughout the next two chapters, this will always be pions, kaons and nucleons, where their respective multiplicities are taken as weights; see left panel of Fig. 3.6).

Although there is in theory a different chemical potential for every particle species, we will here only be interested in true conserved quantum numbers; specifically, the baryon chemical potential. For simplicity, it is assumed that the chemical potential of baryons μ_B can be approximated by that of nucleons μ_N , since they are the most abundant stable baryonic species. It is obtained by using the ratio of the momentum distributions (Eq. 3.37) of nucleons to that of anti-nucleons, such that

$$\frac{dN_N/dp}{dN_{\bar{N}}/dp} = \exp\left(\frac{2\mu_N}{T}\right) \simeq \exp\left(\frac{2\mu_B}{T}\right) . \quad (3.38)$$

This ratio is flat on average in the region which is used for the temperature determination. Its momentum average in this region is calculated and used as a proxy for the baryon chemical potential.

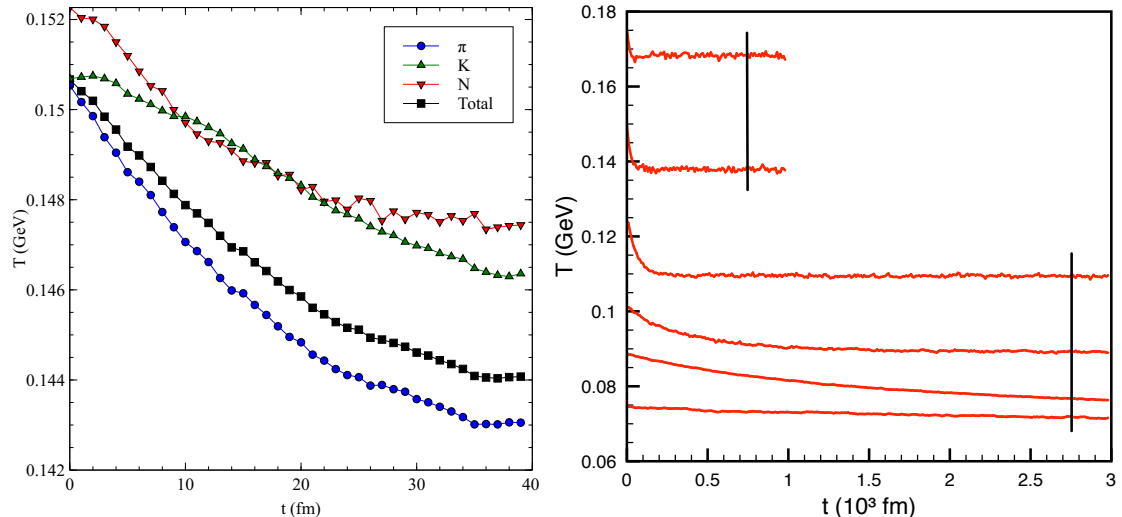


Figure 3.6: Left: Temperature evolution of different species and of the hadron gas at a given starting temperature. Right: Temperature evolution of the box over time, for different initial temperatures. The vertical bar shows which part of the evolution is considered as in equilibrium in calculations in Section 4.2.

Finally, let us mention that we use the definition of the Gibbs free energy to calculate the entropy density,

$$s = \frac{w - \mu_B n_B}{T} = \frac{\epsilon + P - \mu_B n_B}{T} \quad (3.39)$$

where we introduce the enthalpy w , energy density ϵ and pressure P . ϵ and P are obtained directly from the diagonal components of the averaged energy-momentum tensor, the temperature T and baryon chemical potential μ_B from Eqs. (3.37) and (3.38) and the baryon number density n_B by counting baryons and anti-baryons in a given volume of the system.

As described in Section 3.2, all species are initialized with thermal multiplicities. The infinite matter simulation is thus left to equilibrate for an appropriate time, and the chemical equilibrium is checked by verifying that the multiplicities of the individual species in the box saturate to a stable value (see [48] for examples). Similarly, the thermal equilibrium requirement is checked by monitoring the temperature of the box and waiting for it to reach a saturation value (see right panel of Fig. 3.6). We observe that thermal equilibration typically takes much longer than chemical equilibration.

Equilibration times depend strongly on the complexity of the content of the system, more degrees of freedom corresponding to longer equilibration times. In the trivial case of the pion gas presented in Section 4.1, only one species of particles is allowed to interact elastically. In this setup, the system is almost directly initialized into chemical and thermal equilibrium, since no particle number changing processes can occur. For the full hadron gas, the equilibration process however lasts markedly longer,

especially at low temperatures (which is expected, as the initial density increases fast as a function of temperature, see Eq. (3.4)). As seen on the right panel of Fig. 3.6, thermal equilibration times for such a system usually range from a couple hundred fm at higher temperatures ($T = 150$ MeV and higher) to several thousand fm at lower temperatures ($T = 100$ MeV and lower).

3.7 A note on versioning

The development of SMASH being an ongoing process, it should be mentioned specifically which version of the code was used. All the information available in this Chapter refers to SMASH v1.6 [235], which is also the version used for most results in this thesis. Exceptions to this are the discussions held in sections 4.1 and 4.2, for which a slightly modified¹⁰ version of SMASH v1.0¹¹ was used. Along with a slew of minor changes to cross-sections following updates to the Particle Data Group Review from 2015 [236] to 2018 [213], the main relevant structural changes in SMASH between these versions concern:

1. The treatment of potentials, which we exclude in all calculations, as mentioned at the beginning of this chapter;
2. The treatment of strings, which is in any case turned off in Sections 4.1 and 4.2 for the sake of conserving detailed balance, as discussed in Section 3.6;
3. The implementation of the AQM prescription discussed in Section 3.5.7, which gives a cross-section to all combinations of particles which did not previously have one. While the inelastic part of the AQM functions through strings and is thus incompatible with the Green-Kubo calculations performed in Chapter 4 and has to be excluded, the elastic part is very much expected to have an effect on transport coefficients on its own; some comments are made concerning the effects of the inclusion of the AQM in Section 4.2.3.

¹⁰The modifications essentially concern the baryon-antibaryon treatment into resonances that was discussed in Section 3.5.3, which were at the time not included in the main version of the code as an option.

¹¹As the official public release of SMASH happened with v1.5, this version is not directly available online.

Chapter 4

Hadronic transport coefficients

In this chapter we will be presenting and discussing many of the main results of this thesis and the more technical considerations that have to be taken into account in order to obtain them. Specifically, we will be obtaining results for the shear viscosity, bulk viscosity and cross-conductivity of hot QCD matter in the hadron gas phase for a wide range of temperatures and baryon chemical potentials.

4.1 Technical considerations and calibration of Green-Kubo calculations

Let us start by reminding the reader of the final expressions obtained from the Green-Kubo formalism in Chapter 2. The shear viscosity, bulk viscosity and cross-conductivity are given respectively by

$$\eta = \frac{V}{T} \int_0^\infty dt' \langle \pi^{xy}(0), \pi^{xy}(t') \rangle_l, \quad (4.1)$$

$$\zeta = \frac{V}{T} \int_0^\infty dt' \langle p(0), p(t') \rangle_l, \quad (4.2)$$

$$\sigma_{QQ, QB, QS} = \frac{V}{T} \int_0^\infty \langle j_{Q,B,S}^x(0), j_x^Q(t') \rangle_l dt', \quad (4.3)$$

where

$$\langle A(t), B(t') \rangle_l \equiv \langle (A(t) - \langle A \rangle_l)(B(t') - \langle B \rangle_l) \rangle_l \quad (4.4)$$

For convenience, we define the autocorrelation (or simply correlation) functions $C^{xy} \equiv \langle \pi^{xy}(0), \pi^{xy}(t) \rangle_l$, $C^\Pi \equiv \langle p(0), p(t) \rangle_l$ and $C_j^{QQ, QB, QS} \equiv \langle j_{Q,B,S}^x(0), j_x^Q(t') \rangle_l$. As covered in detail in Chapter 3, we remind the reader that simulations provide us with the complete phase-space information of all particles in the system, which are in this case discrete, and given at discrete times. For this discrete situation, we can define the

previous components of the correlation functions as

$$T^{\mu\nu}(t) = \frac{1}{V} \sum_{i=1}^N \frac{p_i^\mu(t) p_i^\nu(t)}{p_i^0(t)}, \quad (4.5)$$

$$j_{Q,B,S}^\mu = \frac{1}{V} \sum_{i=1}^N (q, b, s)_i \frac{p_i^\mu(t)}{p_i^0(t)}, \quad (4.6)$$

where N is the total number of particles, p_i^μ is a component of the energy-momentum 4-vector associated with particle i and $(q, b, s)_i$ its associated appropriate charge (i.e. electric, baryonic or strange). Here we use the fact that in the local frame $\pi^{xy} = T^{xy}$ and $p = T_i^i$. The averaging contained within the correlation functions also has to be redefined for the discrete times at which the information is available; rather than Eq. (2.20), it will take the form

$$C(t) = \langle A(0)A(u\Delta t) \rangle_l = \lim_{K \rightarrow \infty} \frac{1}{K-u} \sum_{s=0}^{K-u} A(s\Delta t)A(s\Delta t + u\Delta t), \quad (4.7)$$

where K is the total number of considered time steps, u is a positive integer with $u < K$ and Δt is the time interval between each time step (i.e. the time before which the information of the system becomes available again).

Let us now look in more detail into the case of the shear viscosity; the remainder of the discussion in this section is very similar for any transport coefficient, so for the sake of brevity we will not repeat it for the cases of the bulk viscosity and cross-conductivity, although we will occasionally refer to some particularities of the one or the other where necessary.

As one can see from Eq. (4.1), the calculation of the viscosity requires integrating C^{xy} from zero to infinity. It is rather straightforward however to see that it is numerically quite challenging to take the limit of $K \rightarrow \infty$ in Eq. (4.7). Consequently, the relative error of any numerical computation of the correlation function necessarily increases rather quickly with time $t \equiv u\Delta t$ and eventually reaches a state of pure noise, as one can see in the thick red curve of Fig. 4.1. To circumvent this limitation, some assumption is made about the analytical shape of the correlation function.

It is generally assumed [78–80] that for dilute systems, it takes the form of a decaying exponential,

$$C^{xy}(t) = C^{xy}(0) e^{-\frac{t}{\tau}}, \quad (4.8)$$

where τ is the relaxation time of the system. For the shear viscosity, it follows that

$$\eta = \frac{C^{xy}(0)V\tau}{T}. \quad (4.9)$$

One of the simplest hadron gas systems that one can think of is composed of one

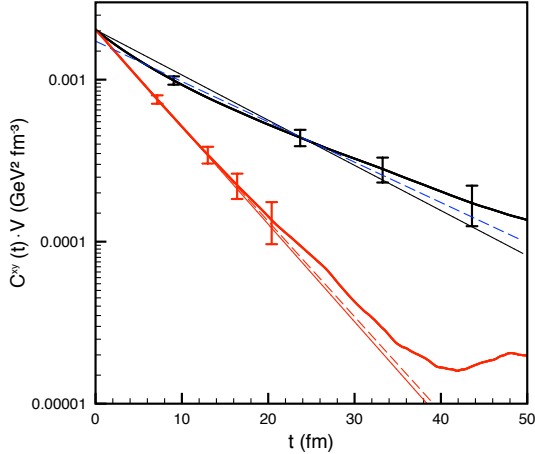


Figure 4.1: Average volume-independent correlation function as a function of time for a system of particles with constant cross-section (red, bottom set of curves) and energy-dependent pion cross-section (black, top set of curves). Thinner lines are exponential fits, respectively with (solid) and without (dashed) a fixed intercept.

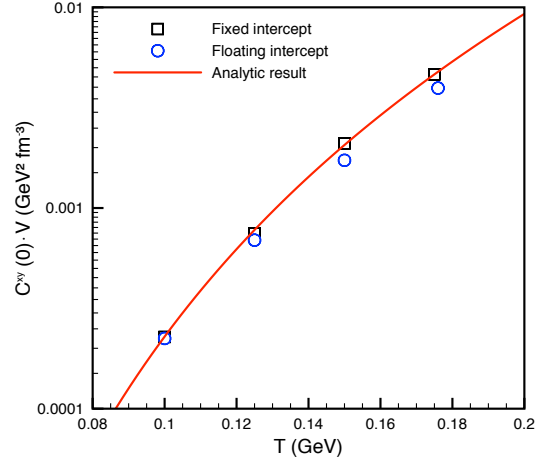


Figure 4.2: Volume-independent initial value of the correlation function as a function of temperature for a system of particles interacting via the energy-dependent pion cross-section. Statistical error bars are smaller than the symbol size.

species of particles that only interacts elastically, either via a constant isotropic cross-section (like hard spheres¹) or through an energy dependent cross-section based on a single resonance. These systems have been studied extensively and, as briefly discussed in Chapter 2, their shear viscosity can be extracted analytically by linearizing the collision term of the Boltzmann equation using the Chapman-Enskog approximation [80, 237]. As such, this system constitutes the perfect playground for a proof of concept. The main goal of this first study is the evaluation of the systematic error of the present calculation by comparing it to a well-known and understood case.

We first take a look at the shape of the correlation function in this simple case. The thick lines of Fig. 4.1 correspond to the average correlation functions of the two versions of the test system at $T = 150$ MeV. In the first (red), massive particles ($m = 138$ MeV) interact through a constant isotropic cross-section of $\sigma = 20$ mb, whereas in the second (black), the same particles interact through an isotropic energy-dependent cross-section corresponding to the ρ resonance. In all cases here and further on, the correlation function is obtained by averaging 1000 simulations of the same system. The behavior of the correlation function of these two systems is definitely different. While

¹Formally speaking, the time of interaction might be slightly different in the hard sphere scenario vs the SMASH criterion of the time of closest approach; this should however not be an appreciable difference in the dilute gas limit.

in the case of the constant cross-section interaction, the behavior is quite close to the previously mentioned decaying exponential, we observe a slight deviation from it in the energy-dependent case. This phenomenon is more apparent at high temperatures and densities; the deviation of the shown curve is thus more pronounced than most others used in the rest of this thesis, for the purpose of illustration.

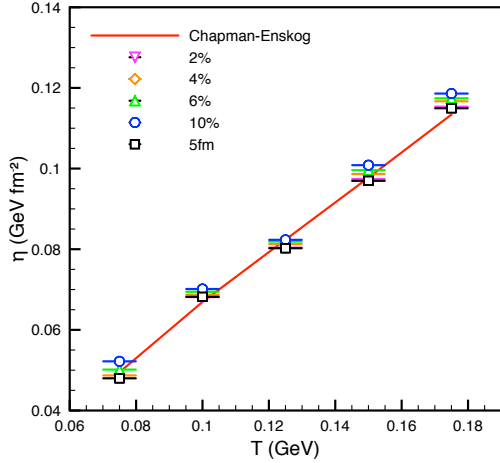


Figure 4.3: Shear viscosity of a system of particles interacting via constant cross-section for various fitting schemes, compared to a semianalytical Chapman-Enskog calculation. ($\sigma = 20$ mb, $m = 138$ MeV)

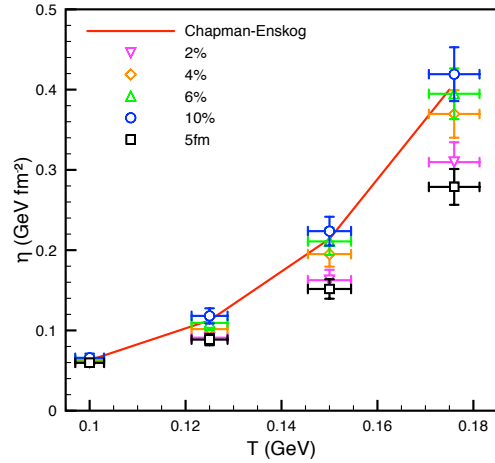


Figure 4.4: Shear viscosity of a system of particles ($m = 138$ MeV) interacting via the energy-dependent pion cross-section for various fitting schemes, compared to a semianalytical Chapman-Enskog calculation.

For N_{spec} stable particles, the initial value of the correlation function is given by taking the continuum limit of

$$C^{xy}(0) = \left\langle \sum_i \frac{(p_i^x)^2 (p_i^y)^2}{V^2 (p_i^0)^2} \right\rangle \rightarrow \sum_{a=1}^{N_{spec}} \frac{g_a z_a}{30\pi^2 V} \int_0^\infty dp \frac{p^6}{m_a^2 + p^2} \exp\left(-\frac{\sqrt{m_a^2 + p^2}}{T}\right), \quad (4.10)$$

where i sums over all particles, $z_a = \exp(\mu_a/T)$ is the fugacity of the species a and g_a its degeneracy factor. Since $C^{xy}(0)$ is known analytically, it is reasonable to fix it in the fit of the correlation function. Indeed, Fig. 4.2 shows that a fit using a floating intercept systematically undershoots the analytical value of $C^{xy}(0)$ at higher temperatures. Even though such a fit might lead to a better fit of the original curve, a precise value for the initial value is required in our final viscosity calculation (4.9). Therefore, $C^{xy}(0)$ needs to be fixed.

Let us now turn our attention to the question of how many points to consider when fitting (i.e. how far to go on the time axis of Fig. 4.1). We tried two different schemes to this effect. The first one is to consider a fixed interval from $t = 0$ to $t = 5$ fm; this interval is small enough that it always very closely fits the earliest part of the curve.

The second scheme takes into account that the growth rate of the relative error of the correlation is much larger at higher temperatures, which is done using a fitting interval for which the cutoff depends on this relative error. This is illustrated by the four points which have error bars on both thick curves of Fig. 4.1: they correspond in each case to the point where the relative statistical error reaches 2%, 4%, 6% and 10%. The plotted fits correspond here in all cases to using all points up to 6% relative error.

In order to determine which of these cutoffs to use, we now compare the final shear viscosity yielded by each to an analytical calculation of the shear viscosity of the two previously mentioned variants of the simple pion gas using the Chapman-Enskog approximation to solve the Boltzmann equation [75]. Fig. 4.3 shows the effect of varying the cutoff on shear viscosity in the case of a system interacting through constant cross sections, whereas Fig. 4.4 shows the same for the case of energy-dependent interactions. In the second case, resonance lifetimes have been decreased to zero in SMASH, so that the comparison is carried out between comparable systems using point-like 2-to-2 interactions². All calculations use an isotropic cross-section.

As expected from looking at the correlation function on Fig. 4.1, the final effect of varying the cutoff is rather limited when cross-sections are constant. All proposed cutoff schemes and values appear to describe well the analytical calculation, with the largest deviations remaining under 8% in all cases. If one now looks at Fig. 4.4, where cross-sections are energy dependent, the picture is different. It is here very clear that there are cases where the sensitivity to the cutoff is large. Cutoffs at 4%, 6% and 10% relative error manage to fit the Chapman-Enskog calculation within systematic errors. While it appears that in this regime it is still possible to use exponential fits, one should keep these deviations in mind when using this ansatz, and possibly look into different ones if deviations become larger.

Now that these considerations have been taken into account, we explore the systematics of the constant cross-sections case. Fig. 4.5 shows the result of a comparison between the SMASH infinite matter calculation employing the Green-Kubo formalism to a 15th order Chapman-Enskog calculation [75]. The first three panels show the dependence of the shear viscosity on the three physical parameters that appear in this calculation, namely the temperature (a), the constant elastic cross-section (b) and the mass of the particles (c), all of these being otherwise kept equal. We remind the reader that the kinetic theory estimates of η for a system of ultrarelativistic particles interacting with a constant cross section is $\eta \sim T/\sigma$ [43, 80] and for nonrelativistic particles is $\eta \sim (Tm)^{1/2}/\sigma$ [75]. We observe that the shear viscosity increases with temperature and mass, and decreases with cross-section. This behavior is expected,

²We will come back to this non-trivial difference between the calculations later in Sections 4.2.1, 4.2.3, 4.3.2 and 4.4.

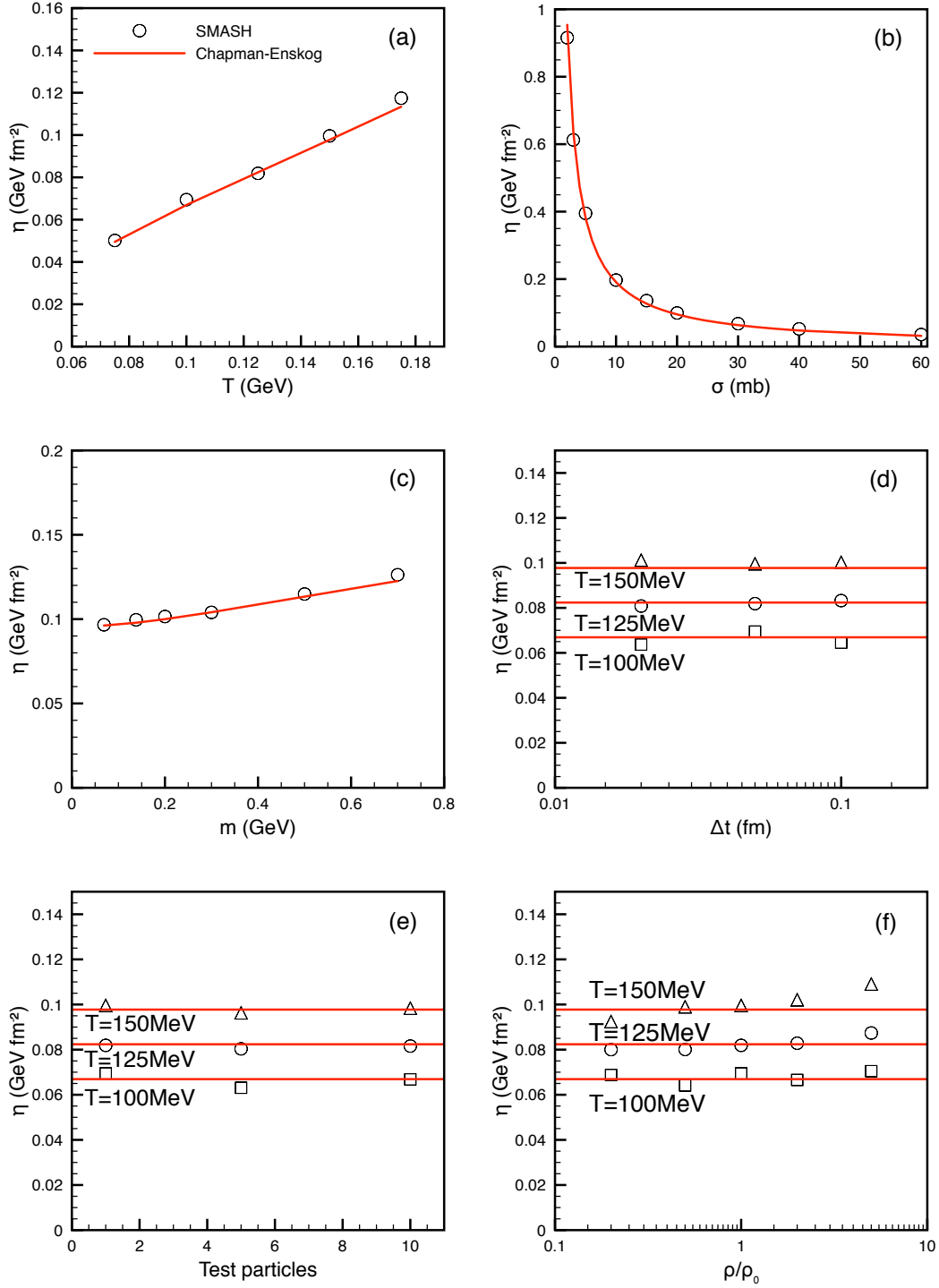


Figure 4.5: Single-species gas systematics. Viscosity of a massive gas interacting through constant elastic cross-section, as computed in SMASH (symbols) and a Chapman-Enskog approach (red lines), plotted versus temperature (a), cross-section (b), mass of the particle (c), time step size between calculations of T^{xy} (d), number of test particles (e) and density ratio n/n_0 (f), where n_0 is the particle density at zero chemical potential. When not mentioned directly on the plot or on an axis, $T = 0.15$ GeV, $\sigma = 20$ mb and $m = 0.138$ GeV.

since the relaxation time to equilibrium decreases as the cross section and thus the number of collisions increases. The dependence on the cross section is very well approximated by $1/\sigma$, while the precise scaling with T and m follows an intermediate behavior between the nonrelativistic and ultrarelativistic cases.

The three last panels of Fig. 4.5 refer to the method's dependence on more technical parameters. Panel (d) shows that, provided the use of a sufficiently small timestep size, the result converges to the analytical value. We find that the range of timestep sizes considered is appropriate; all further calculations use a timestep size of 0.05 fm. Plot (d) shows the effect of including test particles. In this case each physical particle is divided into multiple ones while correspondingly scaling down each components' cross-section, thus approaching the continuum limit. Very limited effects are observed. Hence, for simplicity, and since the use of many test particles implies heavy computational costs, all further calculations are made using only one physical particle. Note that this result differs from what is found in the literature [80], where the use of hundreds of test particles is recommended. Since τ is independent from N_{test} in a local collision kernel, it follows that the non-locality of the geometrical collision criterion could explain differences in viscosity from the number of test particles [238]. The apparent discrepancy can be explained by the fact that we use similarly large numbers of box calculations instead of test particles for computational convenience. The last plot (f) explores the effect of altering the density of the system at a constant temperature. In principle, it is well known that the shear viscosity is independent of the density [239]. Within our calculation however, it is possible that numerics have an effect on observables in some limits. Yet, as the last panel shows, these effects prove to be negligible in most cases, with the exception of very large densities at higher temperatures. In any case, these non-zero deviations remain small with respect to the value of the analytical calculation.

This first test scenario shows that, as expected, the results of the method are mostly unaffected by the variation of non-physical parameters. Thus it is applicable in a wide range of more complex situations. The maximum deviation from analytical calculations is observed to be less than 8% for the case of the shear viscosity (this will vary for other coefficients, notably the cross-conductivity, see Section 4.4). Statistical error bars being smaller than the symbol size in all plots, this systematic error value is assigned to be our total error in all further calculations³ (this is also where the error bars come from in Fig. 4.4, although we neglected to mention it earlier).

³An exception to this is the calculation of the bulk viscosity in the simple constant cross-section elastic pion gas; this will be further discussed in Section 4.3.1.

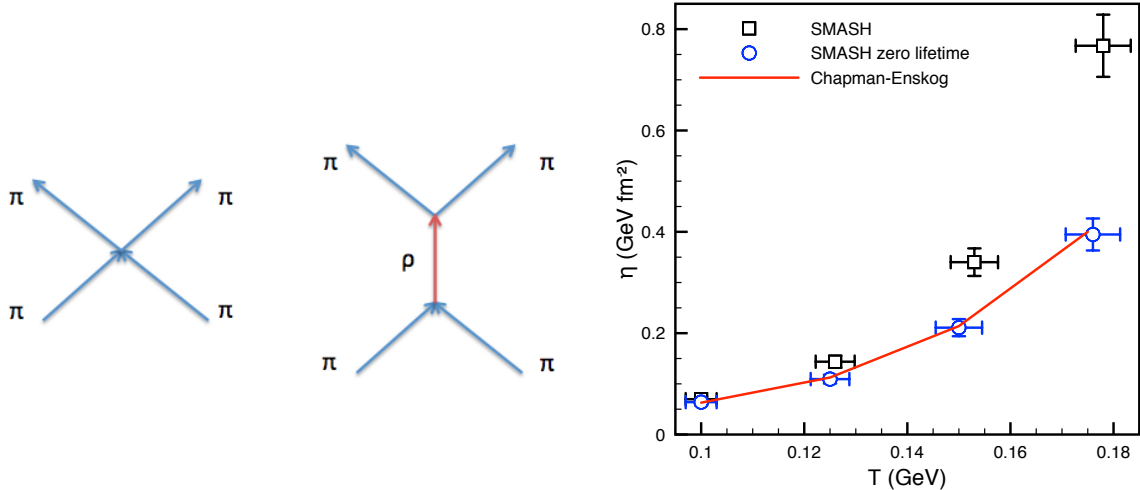


Figure 4.6: Left: Sketch of the point-like vs resonant picture of interactions. Right: Shear viscosity vs temperature in a $\pi - \rho$ gas, for different lifetimes and compared to the Chapman-Enskog analytical result.

4.2 Shear Viscosity

Now that a firm basis for the calculation has been established, we use it to calculate the shear viscosity in a succession of systems of increasing complexity.

4.2.1 $\pi - \rho$ system

We first revisit the system consisting of pions interacting through a ρ resonance which is described by a Breit-Wigner mass distribution. Remember that the pion pair is produced isotropically in the rest frame of the resonance.

Analytical calculations of the viscosity of such systems using the Chapman-Enskog formalism exist [66, 67, 75, 240]. These analytical calculations consider a system of pions interacting via a cross-section that reproduces the ρ peak, but the resonance is actually never produced, the outgoing pions being directly created in a point-like interaction. The left panel of Fig. 4.6 illustrates the schematic difference between the two descriptions; as one can see, the main difference between the two pictures is the fact that in SMASH, the ρ resonance has a finite non-zero lifetime.

For the sake of comparison, several modifications have been made in the approach presented in [75]: 1) only the $(I, J) = (1, 1)$ channel (relevant for the ρ meson) is kept in the $\pi\pi$ scattering, whereas the isoscalar and isotensor channels are neglected, 2) in spite of the genuine p -wave scattering in the isovector channel, the differential cross section is tuned to be isotropic for consistency with SMASH ⁴, and 3) we implement

⁴The shear viscosity is inversely proportional to the “transport cross section”, $\sigma_{tr}(s) = \int d\Omega \sin^2 \theta d\sigma/d\Omega(s, \theta)$ [80]. For an s -wave isotropic interaction one has $\sigma_{tr} = 2/3\sigma_{tot}$, where σ_{tot} is the total cross section. For a p -wave interaction one has $\sigma_{tr} = 2/5\sigma_{tot}$. Therefore, the shear

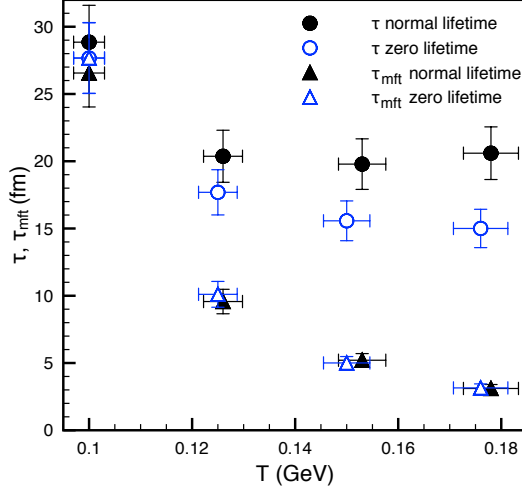


Figure 4.7: Relaxation time τ and mean-free time τ_{mft} versus temperature in a $\pi - \rho$ gas, for different lifetimes.

the same squared scattering amplitude from SMASH, but multiplied by a factor $6/9$. This is due to the fact that in [75] an average scattering amplitude for all possible 9 initial states $(\pi^\pm, \pi^0) \otimes (\pi^\pm, \pi^0)$ was used, whereas in the simulation we consider only 6 of these combinations (more specifically, scatterings between pions of the same charge are not possible, if including only the ρ meson).

The right panel of Fig. 4.6 shows the effect of this difference on viscosities, as well as the effect of forcing resonances to decay immediately in our transport model, which effectively sets the lifetime of the ρ resonance to zero and makes interactions point-like. This has the effect of bringing the two results much closer together, to the point where the two calculations are once again in strong agreement.

As shown in Fig. 4.7, the lowering of the shear viscosity when setting the resonance lifetimes to zero is explained by looking at the relaxation time of the system in both cases. As one can easily see, the relaxation time appears to be increasingly reduced as one goes to higher temperatures; this suggests that the lifetime of resonances can have a large impact on the relaxation time when the lifetime is not negligible with respect to the mean free time of the particles in the system. This latter case is consistent within error bars with τ reaching a plateau at high energies. Intuitively, the finite lifetime of the ρ meson delays the momentum transfer and therefore affects the relaxation dynamics. Note as well that the time between pion collisions (or mean free time) τ_{mft} remains unaffected by this change in lifetimes.

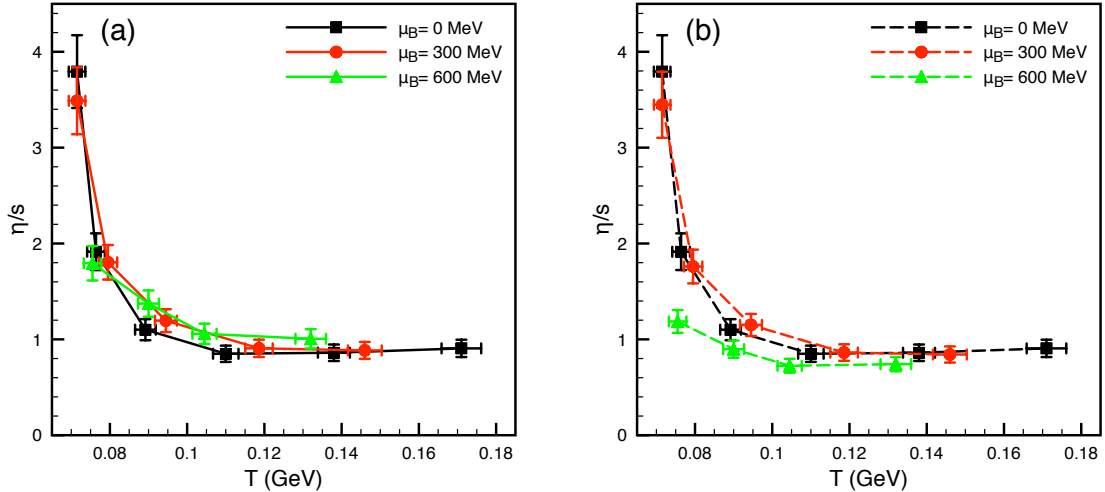


Figure 4.8: Shear viscosity to entropy (a) and enthalpy (b) density ratios vs temperature, for various baryochemical potentials.

4.2.2 Full hadron gas

We now proceed to calculate the shear viscosity of a hadron gas as simulated in the SMASH transport approach. Fig. 4.8 shows both the ratio of shear viscosity to entropy density (a) and the ratio of shear viscosity to enthalpy density (b). Although the former is used as an input to hydrodynamic simulations [26, 27], it has been argued that the latter provides more insight into the transport properties of dense hadronic matter as this combination appears in the sound attenuation length [22]. Here, both ratios are displayed. If we first look at the zero baryonic chemical potential curves (which are identically the same, as expected), we see that they display a decreasing profile at low temperatures, which corresponds to the expected behavior of a liquid approaching a phase transition [241]. One also notices that the shear viscosity to entropy/enthalpy density ratio reaches a plateau around a temperature of 110 MeV, and stays flat until around 170 MeV, that is, for the whole region around the temperature of 155 MeV at which the phase transition is situated [3]. The ratios start to increase slowly at temperatures higher than 170 MeV, but this is also the temperature above which quark and gluon degrees of freedom are becoming important. In SMASH, the cross-sections via resonance excitation decrease at high energies and therefore our calculation is only meaningful in the hadronic region of the phase diagram.

Moving on to non-zero net baryon chemical potential, it appears that the ratio of shear viscosity to entropy density is relatively independent of μ_B at every plotted temperature, at least until values of the chemical potential of approximately 600-650 MeV. On the other hand, the ratio of shear viscosity to enthalpy density displays a difference when going to higher chemical potential. The difference between the two

viscosity of a p -wave interaction is a factor 5/3 larger than the isotropic scattering.

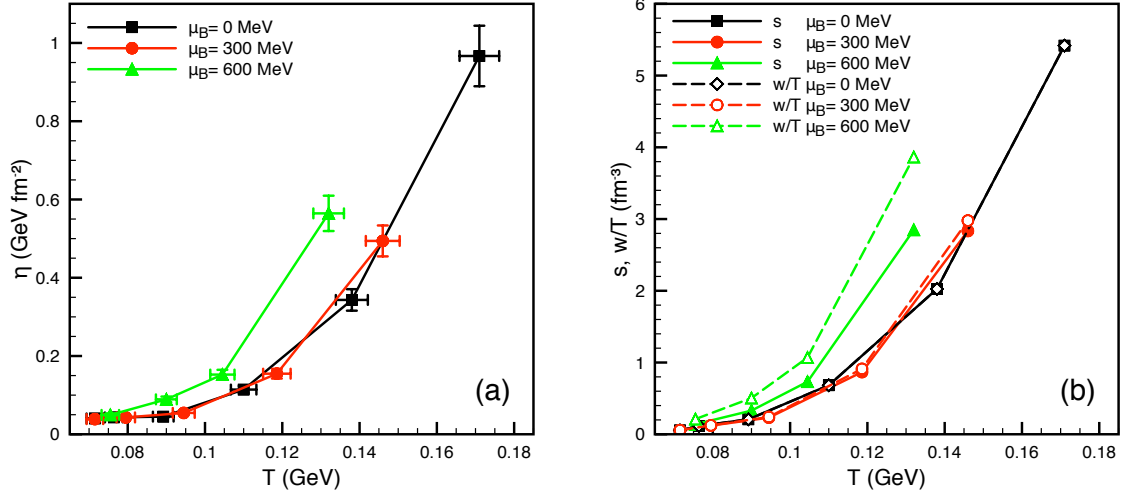


Figure 4.9: Shear viscosity (a), entropy and enthalpy densities (b) vs temperature, for various baryonic chemical potentials.

ratios highlights that the inclusion of the baryonic chemical potential term in the entropy calculation (see Eq. (3.39)) can at times obscure some trends in the physical picture.

For future reference and to help shed some light on the various features of Fig. 4.8, we now plot all components individually, namely the shear viscosity, entropy density and enthalpy density (Fig. 4.9). Panel (a) of Fig. 4.9 shows the behavior of shear viscosity, which we find at all values of the chemical potential to be an increasing function of temperature, as expected. Increasing the chemical potential also raises the shear viscosity at equal temperature for all temperatures, which is also expected.

The second panel (b) of Fig. 4.9 simultaneously shows entropy and enthalpy densities as functions of temperature. Since both of these quantities depend primarily on the energy density of the system, it comes as no surprise that increasing the temperature or baryon chemical potential leads to large increases here as well. Note here that in this plot one sees very well the effect of including the baryonic chemical potential in the entropy calculation, with the difference increasing from zero at $\mu_B = 0$ MeV to differences of 30% at 600 MeV. This can at least partly explain the shape of the corresponding curves in Fig. 4.8.

In Fig. 4.10, let us now further decompose the previous results by plotting the shear relaxation time τ , which comes into play in the calculation of the shear viscosity (see Eq. (4.9)). One should first note that the overall profile of these curves is relatively similar to those of Fig. 4.8. This is expected, since as seen on Fig. 4.9, η rises with the temperature in a way that is approximately matched by the rise in entropy/enthalpy density, so that the final characteristic shape of η/s or $\eta T/w$ is approximately mirroring the shape of the relaxation time.

Fig. 4.11 shows the same data in a different way: instead of taking temperature

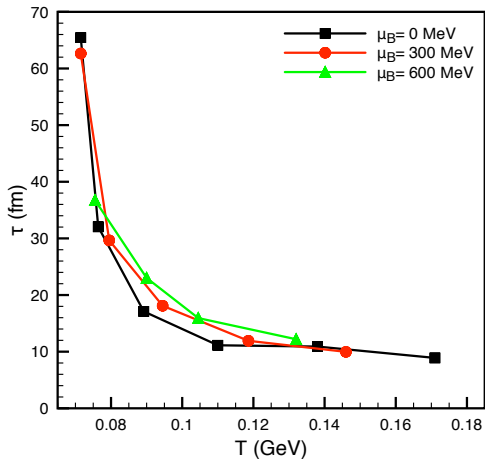


Figure 4.10: Shear relaxation time vs temperature, for various baryonic chemical potentials.

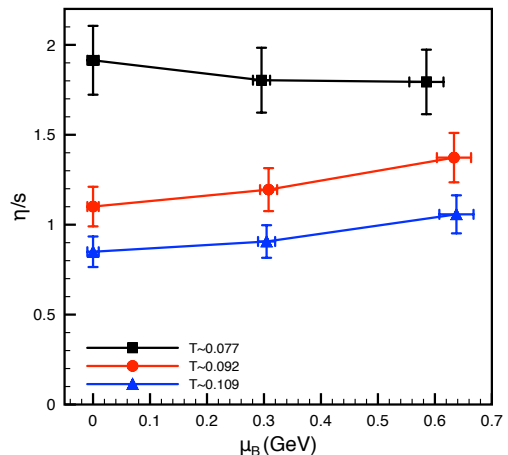


Figure 4.11: Shear viscosity to entropy density ratio vs baryonic chemical potential, for various temperatures.

profiles at approximately constant baryonic chemical potential, the μ_B dependence of the shear viscosity to enthalpy ratio is investigated at approximately constant temperature. As one can see, we observe for all temperatures a slightly increasing plateau at these values of chemical potential; note that within error bars, this calculation is still consistent with no increase at all. The calculated profile of the shear viscosity to entropy ratio at fixed temperature with respect to the baryon chemical potential is actually quite close to what was computed in [71]. Notice that for the current range of temperatures and baryon chemical potentials, it has been checked that the use of Fermi-Dirac instead of Boltzmann statistics has a negligible effect on the observables.

As a reference, we include some typical auto-correlation functions at $\mu_B = 0$ (Fig. 4.12). As one can readily see, the slope of the function gets steeper with rising temperature; this was directly visible from the previous Fig. 4.10, where we saw the relaxation time (the inverse of the slope) steadily falling. The slightly non-exponential behavior that one observes was discussed in more detail in section 4.1 and [242].

4.2.3 Discussion and comparison

In this section, let us first summarize previous calculations of the shear viscosity over entropy density ratio of a hadron gas and then discuss in detail how they compare with our results. As mentioned in Chapter 1, the shear viscosity of the hadron gas is an active subject of discussion within the field of heavy ion collisions, and multiple comparable calculations of its value were performed previously, especially for the zero baryon chemical potential case. A comparison of these available calculations is presented in Fig. 4.13. The Demir & Bass [78] calculation uses a similar Green-Kubo

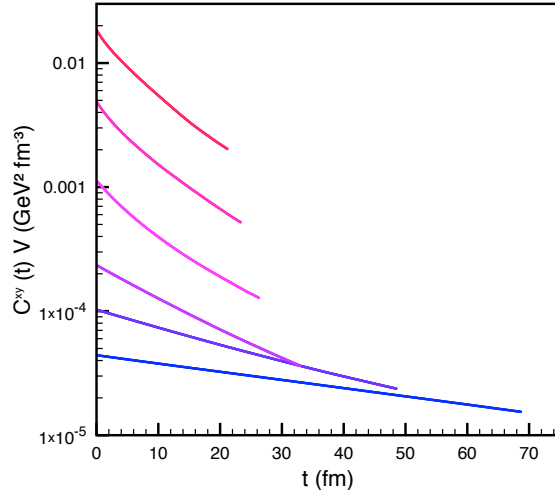


Figure 4.12: Typical volume-independent correlation functions for various temperatures at $\mu_B = 0$. From blue to red, or bottom to top, the fitted corresponding temperatures are respectively 71.5, 76.4, 89.2, 110, 138 and 171 MeV. The plotting stops when the relative statistical error reaches 6% in each case, and thus corresponds to the part of the curve which is fitted.

formalism, but in the context of the UrQMD transport code [44]. The Pratt, Baez & Kim [82] curve is computed using the B3D code [226], but this time by extracting the viscosity from Israel-Stewart equations, while obtaining the necessary other transport coefficients from the Kubo formalism. The Romatschke & Pratt [94] one uses once again the B3D cascade code, with the viscosity η/s being assimilated directly to the response of the energy-momentum tensor to a velocity gradient. The Rougemont et al. curve [88] is computed from a holographic correspondence using the Einstein-Maxwell-Dilaton model. Ozvenchuk et al. [81] use the relaxation time approximation for η applied to the Parton-Hadron-String Dynamics approach [225]. Moroz [76] is an analytical calculation of the hadron gas shear viscosity using the relaxation time approximation and modified UrQMD cross-sections (in this reference the EQCS2s set was used). The Wiranata et al. [240] calculation use a Chapman-Enskog expansion to solve the Boltzmann equation using K-matrix parametrizations for cross-sections. Finally, the χ PT curve also uses a Chapman-Enskog expansion but this time by relying on the lowest-order scattering amplitude from chiral perturbation theory for the massive pion interaction [75] (see Fig 4.14).

Let us now discuss the comparisons for each result starting from the low temperature region. Chiral perturbation theory [243] is the low-energy effective theory of QCD describing the dynamics of the pseudo-Goldstone bosons, associated to the spontaneous symmetry breaking of the chiral symmetry. At lowest order in the chiral expansion, the effective Lagrangian provides the scattering amplitude for the $\pi - \pi$ scattering [244].

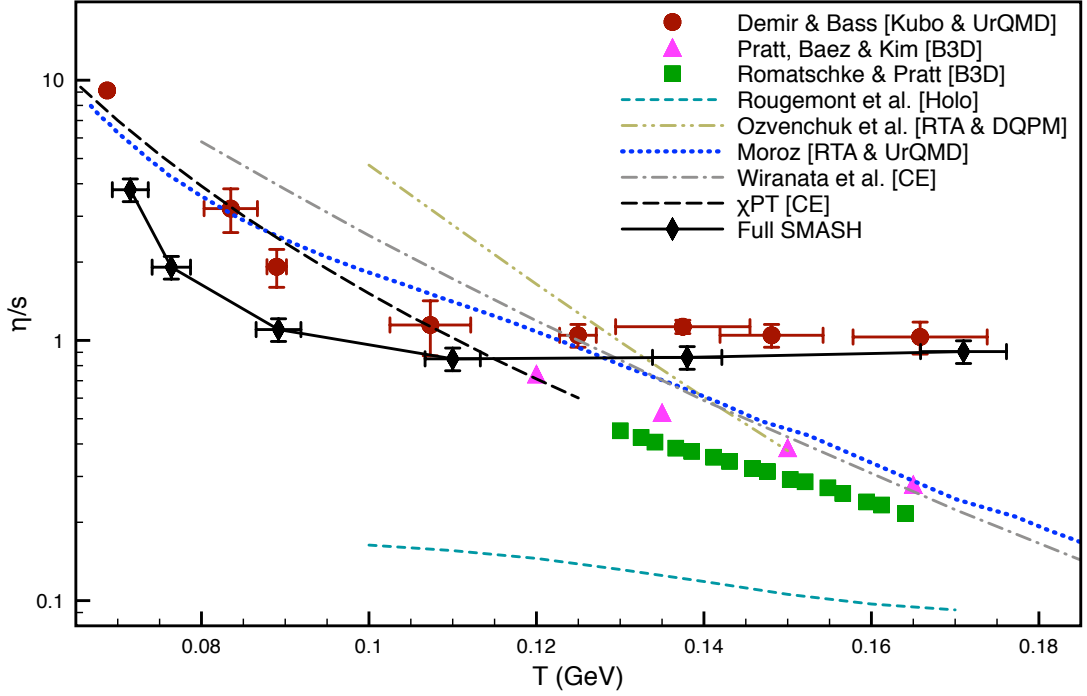


Figure 4.13: Comparison of several calculations for the hadron gas η/s at $\mu_B = 0$; see text for details.

The LO χ PT calculation with massive pions provides a model-independent reference value for η/s . However, its validity is restricted to very low temperatures where the system can be approximated to a gas of low-energy pions (up to $T \sim 70$ MeV [71]). At low temperature, SMASH gives values of η/s of the same order of magnitude, but one should not expect a perfect matching to the LO χ PT with our results: in the former, the $I = 1$ channel carries an angular dependent differential cross section (the lowest allowed partial wave is a p -wave) as opposed to isotropic emissions in SMASH (as mentioned earlier, this accounts for differences of the order of up to $5/3$ lower viscosity in pion dominated systems). Further differences exist between the transport model and χ PT calculations. As seen on Fig. 4.14, the dominant $\pi^+\pi^-$ cross section at these low temperatures (which corresponds to the early part of the curve, $\sqrt{s} > 0.7 - 0.8$ GeV) is significantly larger in SMASH (especially when going to higher energies, where χ PT cannot describe any kind of resonant interaction), which also contributes to lower viscosities. The χ PT result additionally contributes to the elastic $\pi^\pm\pi^\pm$ scattering, which is not taken into account in the transport model, although it is expected this will have a more limited effect. Finally, in SMASH the pion scattering occurs by the formation of an intermediate resonance containing the inherent time delay due to its lifetime, which is not implemented in the χ PT calculation. This was mentioned in section 4.2.1 and will be explained in more detail later on in this discussion, although it should remain much smaller than the other effects at such small

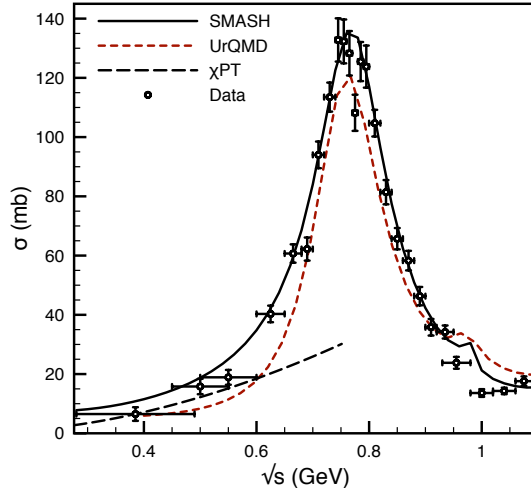


Figure 4.14: Total $\pi^+\pi^-$ cross-section in SMASH, UrQMD and LO χ PT, compared to experimental data.

temperatures (see discussion around Fig. 4.6).

Differences between the SMASH and UrQMD description of $\pi\pi$ cross-sections can explain the low temperature discrepancy between our calculation and that of Demir & Bass [78] which used a comparable Green-Kubo method with this other transport code. Fig. 4.14 is useful in this regard: although both transport approaches describe reasonably well the experimental data, at low energies SMASH tends to slightly overshoot it while UrQMD slightly undershoots it; this results in a cross-section that is sometimes twice as large in SMASH at low energies. UrQMD also includes a flat 5mb elastic cross-section for all $\pi\pi$ processes, which could have a slight cancellation effect (although this very small cross-section compared to the much larger inelastic one should not affect viscosity results so much). Similarly to SMASH, UrQMD does not account for the p -wave nature of the ρ resonance.

Therefore, a perfect agreement between transport models such as SMASH or the conceptually similar UrQMD and χ PT remains unlikely, and it is then no real surprise that our results remain lower than these calculations at low temperature. As a corollary, although the result from Demir & Bass appears to agree very well with χ PT, this can be accidental to a certain extent.

The Moroz calculation [76] employs an approach to calculate viscosity analytically from the relaxation time approximation in the full hadron gas. The calculation uses a set of improved cross sections from the UrQMD model, including elastic plus quasielastic processes (EQCS2s set). The cross sections are implemented in analytical expressions for the shear viscosity obtained from simplifying Boltzmann equation using the relaxation time approximation, a formalism analog to that presented in Section 2.2. Although information from resonances is encoded in the cross sections, the collision kernel only contains elastic processes, and no retardation effects from finite lifetimes

are considered. It matches quite well the simpler χ^{PT} expectation at low temperatures; our results however appear to remain consistently larger than this analytical curve for temperatures larger than 130 MeV.

Wiranata et al. [240] obtain very similar results (although slightly larger at low temperature) using the Chapman-Enskog approximation in a four-component mixture of $\pi - K - N - \eta$. These interact through cross-sections computed using K-matrix parametrizations (which respects the unitarity of the scattering matrix) including many resonances with masses going up to 2 GeV. All interactions remain here once again point-like and no resonance propagation happens.

In Ozvenchuk et al. [81] the relaxation time approximation is used to simplify the Boltzmann equation and obtain a simple formula for the shear viscosity. Even when resonance formation is implemented in PHSD simulations, the relaxation time is identified with the mean-free time extracted from collision rates in a box simulation. In this approach, the relaxation time contains no feedback from the resonance lifetimes.

Although exact values differ quite a bit, the general consensus appears to confirm the expectation that the viscosity should generally decrease when approaching a phase transition. That being said, two tendencies are appearing in this plot: some calculations are constantly decreasing for the available data in this range of temperatures, and others appear to saturate at some point and form a plateau at higher temperature; our calculation is among the latter.

Of note, the calculation by Demir & Bass [78] appears to have a similar behavior as ours as temperature increases, with the viscosity also saturating at high values of T . Even though our results are otherwise somewhat smaller, this similarity in the behavior is striking when compared to the other tendency, which predicts a steadier decrease to sometimes much lower values around the phase transition. One of the common points between UrQMD and SMASH is the treatment of interactions through resonances, which have a non-zero lifetime as illustrated in the left panel of Fig. 4.6. In contrast, almost all other calculations use point-like interactions for a great portion of the considered hadronic interactions, if not all. The B3D transport code includes many long-lived resonances, but simultaneously includes an overall constant cross-section of $\sigma = 10$ mb [226], which introduces many point-like interactions, and is thus somewhat hybridized in this regard⁵. Rougemont et al. [88] use the completely different framework of holography, and is therefore excluded from this categorization.

To understand how resonance lifetimes affect the relaxation dynamics, consider a

⁵In principle, at the time [78] was published, UrQMD also included a point-like elastic cross-section extracted from the Additive Quark Model between all particles. However, on inspection, this elastic cross section turns out to be much smaller than the non-elastic resonance contribution (maximum of 1.35mb in the largest cases, on average almost an order of magnitude smaller). In consequence, only a small number of collisions were point-like in this previous version UrQMD; this has since been updated to provide the same treatment as was described in Section 3.5.7, although no new calculation of the shear viscosity was performed since.

system without physically present resonances. The relaxation time is the characteristic time in which the system approaches equilibrium after a slight departure from it. This time is of microscopic origin, and it is assumed to be of the order of the collision time (or the inverse of the scattering rate). Under a shear perturbation, particles with different momentum will collide redistributing their energy to approach the thermal distribution. This collision occurs on a time scale of the order of the mean free time, and therefore the relaxation time should be of the same order. If the lifetime of the resonances is finite, but much smaller than the mean free time, then the same picture holds, because the resonance will decay long before the next collision is expected to happen. Therefore, the transport process is unaffected by the generation of a resonance if $\tau_{lifetime} \ll \tau_{mft}$. Again one expects that the relaxation time $\tau \sim \tau_{mft}$. On the other hand however, if the resonance lifetime is comparable to the mean free time (or larger), then the transport process is blocked until the resonance eventually decays, because it is only at that instant that the momentum exchange is finally performed. The relaxation time is thus now limited by the lifetime of the resonance, becoming independent of τ_{mft} , as we have checked numerically for the full hadron box (top right panel of Fig. 4.15).

This picture breaks down if a sufficient portion of the interactions are point-like. If our explanation is correct, this breakdown in [82] is caused by the large amount of elastic point-like collisions, which happen because of the inclusion of a constant 10 mb cross-section in B3D. To see if the physical picture that we are depicting holds, we apply the same constant 10 mb isotropic cross-sections to all interactions in SMASH, so that a significant portion of the collisions will now be point-like. The top left panel (a) of Fig. 4.15 shows the effect of such an adjustment, and we note two differences. The first one is that all points are now at a lower value of shear viscosity, which is explained by the increase in all cross-sections. The second difference is more interesting, and concerns the profile of the curve: rather than saturating at a given value, it now decreases constantly for this range of temperatures, which is what we would expect from a system in which a large part of the interactions is now point-like, so that the relaxation time is not as strongly affected by the lifetime of unstable particles anymore⁶. Alternatively to these constant cross-sections, switching to version 1.6 of

⁶As shown previously in Fig. 4.6 for a simpler system, the effect of these lifetimes can be significant; however, note that in the present case, there might also be another cause to the change in the profile of the curve coming directly from the inclusion of constant cross-sections. Indeed, one can generally approximate that $\eta/s \sim \frac{1}{s} \frac{T}{\sigma}$; if σ is fixed, then η/s will decrease if s is more than linearly dependent on temperature, which it typically is (in massless ideal gases $s \sim T^3$ for example). One could check whether one of these effects is dominant by taking the lifetime of resonances to zero once again. However, removing all resonance lifetimes in such a complex gas is not easily done, as it completely breaks the assumption that resonances must propagate in order to conserve the detailed balance of most reactions, and thus it is unclear whether the obtained gas would be chemically comparable to the current one.

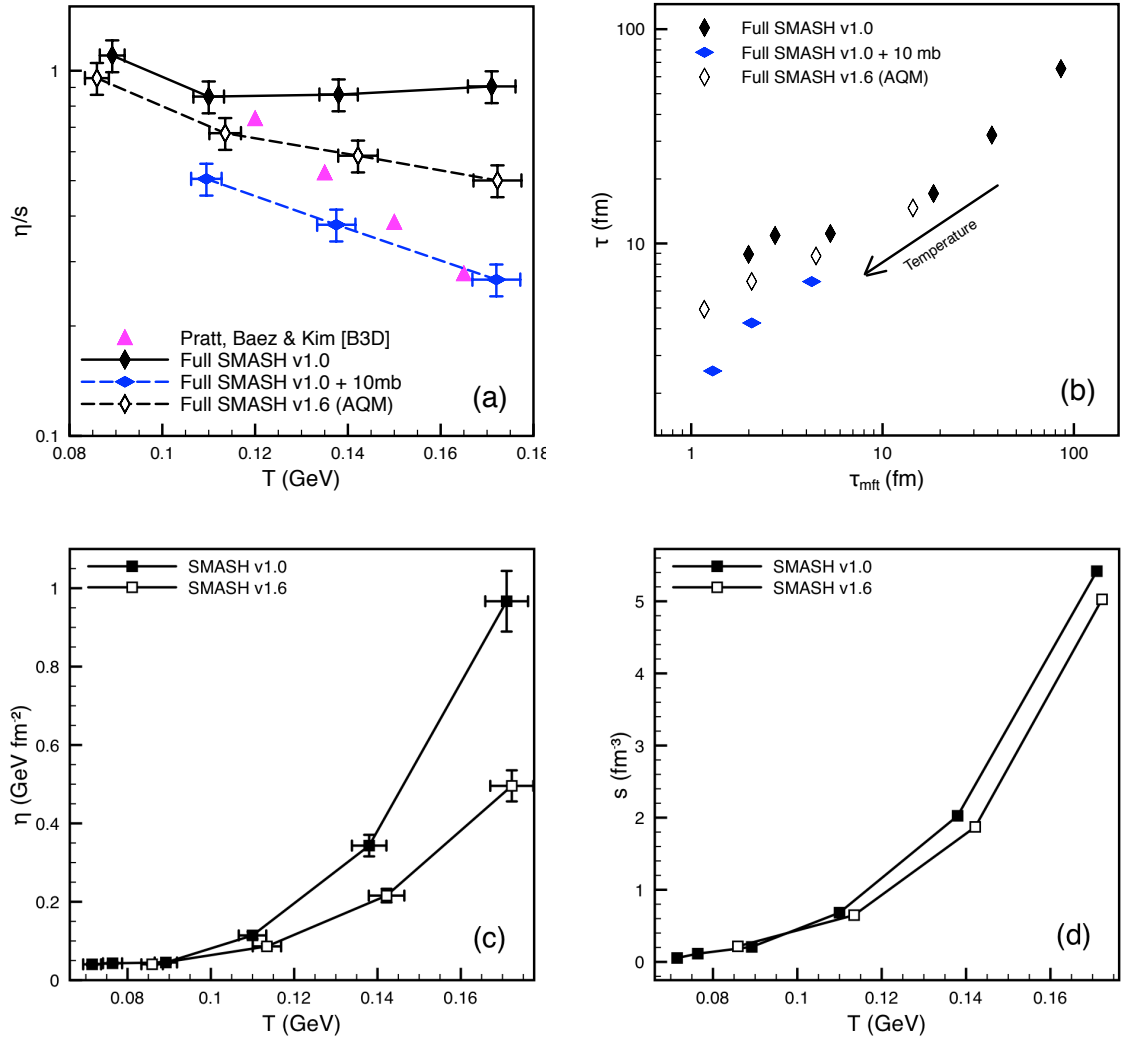


Figure 4.15: Effect of adding a constant cross-section to all interactions on the viscosity (a) and on the characteristic times τ and τ_{mft} (b).

SMASH⁷ allows us to also study the effect of activating the elastic part of the AQM for exotic cross-sections; as described in Section 3.5.7, this prescription scales known energy dependent cross-section parametrizations according to the quark content of incoming particles, such that almost all combinations of particles can now interact. If one refers to Fig. 3.3 and Table 3.5, the large majority of these newly added cross-sections (i.e. meson-meson and meson-baryon) have values around 4-7 mb, with the rarer baryon-baryon collision $\sim 30\%$ higher (not shown here); this essentially means that on average this AQM cross-section should be slightly larger than half the 10 mb present in B3D. One would thus expect that the inclusion of the AQM should interpolate between the two previous results, which is shown to be the case for the viscosity over entropy density ratio in panel (a) of Fig. 4.15. As can be seen in panels (c) and (d), although the entropy density does slightly decrease when including the AQM in SMASH v1.6, which can be attributed to slightly different particle lists between the versions, we see that the bulk of the difference in η/s comes from the large decrease of the shear viscosity η ; this is fully expected as the AQM only affects cross-sections, which do not have an effect on the calculation of the entropy density.

For further evidence of the importance of resonance lifetimes, let us look at the relation between the relaxation time τ and the inverse of the scattering rate, the mean-free time τ_{mft} . In the case of no resonances [82] the relaxation time increases linearly with the collision time, with a proportionality factor of order 1. As seen on panel (b) of Fig. 4.15, this expectation is fulfilled in SMASH for low temperatures, when the collision time of particles is much larger than the lifetime of resonances. However, it breaks down at high temperatures, when the collision time decreases to a value where the lifetime of resonances is now large enough to impact the relaxation time of the system, thus forming a plateau around $\tau \sim 10$ fm. When one includes a large number of elastic point-like collisions into SMASH, either through the inclusion of a constant 10 mb cross-section for all particles or to a lesser extent the slightly smaller elastic cross-sections of the AQM, the plateau disappears and we recover a linear dependency of order 1, even at high temperatures. This is once again in line with the expectations of our resonance lifetime hypothesis.

As a final remark, let us now consider the case of non-zero baryon chemical potential, where literature proves to be a lot scarcer, although not inexistent. In this regard we present two comparisons with other calculations (Fig. 4.16). The first one (a) was made with the similar calculation from [78] with UrQMD, and the second one (b) from a holographic approach [88]. In both cases, they observe a difference between the zero and non-zero baryochemical potential results, with the non-zero case yielding a smaller viscosity. In our calculation, both cases are constant within errors. This discrepancy

⁷See 3.7 for a list of notable differences; as the astute reader will already suspect, the only one which really has a sizable impact is the AQM.

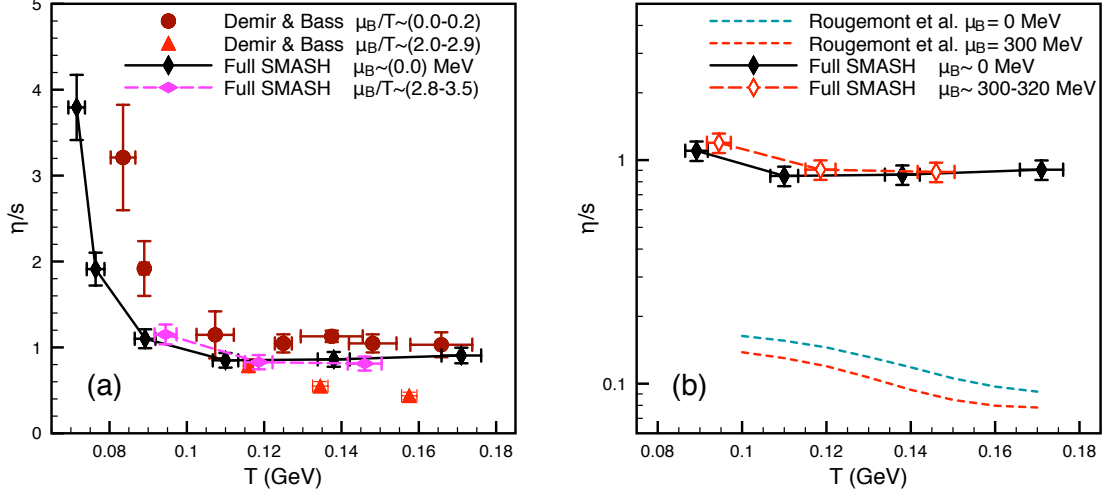


Figure 4.16: Non-zero chemical potential comparison with other models of shear viscosity. Comparison is possible with a previous Kubo calculation [78] (a), and a result obtained from holography [88] (b)

might be explained in the case of Demir & Bass by different methods of calculating the chemical potential term in the entropy (which would also explain why the difference in their curves is growing with temperature); a potential way of seeing whether this is a difference in the actual models would be to compare the shear viscosity to enthalpy ratio instead. The approach in [88] is very different in nature, since it goes beyond the quasi-particle picture and assumes strong coupling without confinement. Being close to the holographic result $\eta/s = 1/4\pi$, it is natural that the resulting values of the shear viscosity to entropy ratio are smaller than in our approach. Still, it is interesting to note that the decrease for higher baryon chemical potentials is also observed just for lower values of the chemical potential than in our calculation, where the differences become significant only around $\mu_B = 600$ MeV. Although not shown here, let us mention that significant differences in the shear viscosity over entropy density ratio were also found in [237] between the zero and non-zero baryochemical potential. However, the use of constant isotropic cross-sections in this calculation instead of energy-dependent ones strongly limits comparability, as the observed decrease in η/s when including a non-zero μ_B can then mainly be attributed to the increase in entropy this provokes.

4.3 Bulk Viscosity

We now turn our attention to the case of the bulk viscosity as calculated using the Green-Kubo formalism (see Eq. (4.2) and discussion around it at the beginning of the chapter), for which we first look back to the simple elastically interacting pion gas before moving on to the full hadron gas.

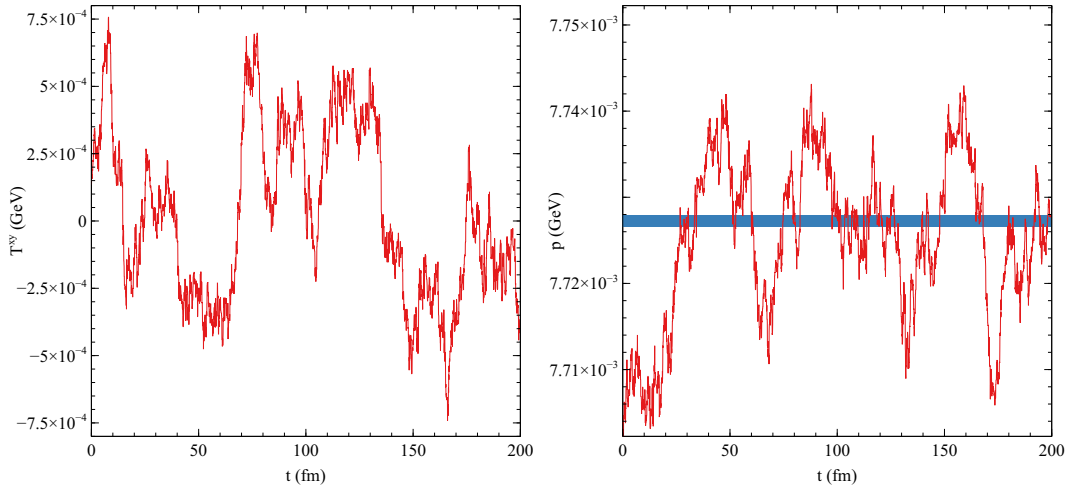


Figure 4.17: Sample fluctuations for the shear (left) and bulk (right) cases for a pion ($m = 138$ MeV) gas interacting via constant $\sigma = 20$ mb cross-sections at a temperature of 125 MeV in a $(20 \text{ fm})^3$ volume. The thick band on the right is the average pressure, with errors.

4.3.1 Elastic pion gas

In this section we look at the details of the Green-Kubo bulk viscosity calculation in a system composed of pions which interact through a constant cross-section. Since bulk viscosity can be thought of as a measure of the resistance to expansion of a system through phenomena such as the vibration or excitation of particles (in the case of the hadron gas, we can thus expect large contributions from resonances), it can come as a surprise that such a simple system would be chosen as a testing ground, as it does not feature any such phenomena. For this system (and many others), the bulk viscosity is expected to be identically zero both in the relativistic and zero temperature limits [95], with some residual signal only perceptible at intermediate energies. Unfortunately, it is also the only available case for which semi-analytical Chapman-Enskog calculations exist for the bulk viscosity in a readily comparable state, and so it remains the only way to calibrate the Green-Kubo calculation.

It is instructive to look at a sample of the measured fluctuations of the pressure in such a system and to compare it to the off-diagonal energy-momentum fluctuations T^{xy} associated with shear viscosity, as done on Fig. 4.17. While the two signals can appear relatively similar at first glance, there are some significant differences between them. The first is the amplitude of the signal, which is roughly 25 times smaller in the case of the pressure. Second, and even more importantly, is the fact that pressure does not oscillate around zero, and thus an average pressure needs to be calculated. This is not as trivial as one could think, as the average pressure then also introduces a statistical error which can be non-negligible. While the calculation of the correlation function is done over 4000 timesteps spanning 200 fm as in the case of the shear viscosity, we find

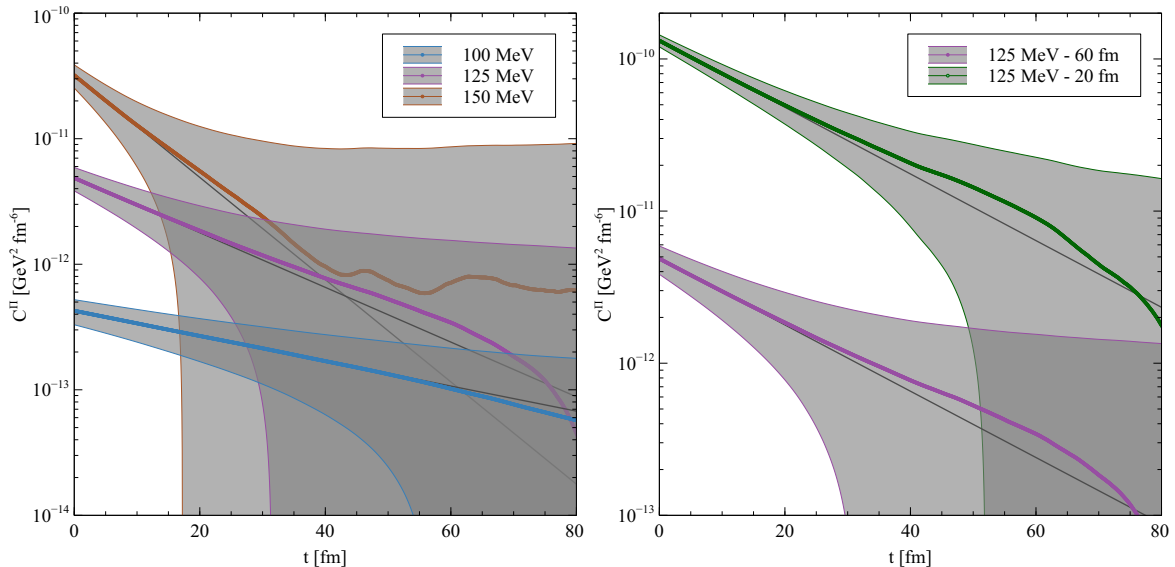


Figure 4.18: Bulk correlation function for a pion gas interacting through constant cross-section $\sigma = 20$ fm at various temperatures (left) and system volume (right), as well as exponential fits, fitting from 0-10fm.

that in order to get results in which the statistical error does not completely wash out the signal, the averaging of the pressure requires much larger datasets. We determined that for the studied cases in this chapter, an averaging going over 100 000 timesteps spanning 5000 fm was sufficient, in the middle of which we perform the previously mentioned calculation of the correlation function⁸.

Fig. 4.18 shows a collection of such correlation functions. The left panel illustrates how a rising temperature leads to an increased steepness of the function (which translates to shorter relaxation times) as well as the general increase in the statistical error as time progresses, which is very similar to the previously explored shear viscosity case. What is quite different in the case of the bulk viscosity however is that even the initial value $C^{\text{II}}(0)$ can have a relatively large statistical error, up to 20% in this case, whereas previously the error on the shear correlation function was never larger than 6% (which would barely be visible, for example in Fig. 4.12). This of course invalidates the previously described scheme to determine at which point one should stop the fitting to a decaying exponential (see discussion around Figs. 4.1-4.4); thus, for the remainder of the discussion on bulk viscosity, we will simply use fixed points at which to stop (in the currently discussed pion gas case, the function is fitted using points up to 5 fm). The right panel of Fig. 4.18 additionally shows that the size of the box used for the calculation matters. Although the slope remains similar and the multiplication

⁸Note that in principle, the thermodynamic pressure can be calculated analytically to a high precision for such a pion gas, which could seem to the reader to be preferable to this numerical calculation, and for future reference, one obtains similar results as presented here, with of course a lower statistical error. However, calculating the average pressure using this analytic way is highly non-trivial for basically any other gas that we will try to study, because of the equilibration processes discussed in Section 3.6, so that using this leads to being unable to go to more involved cases.

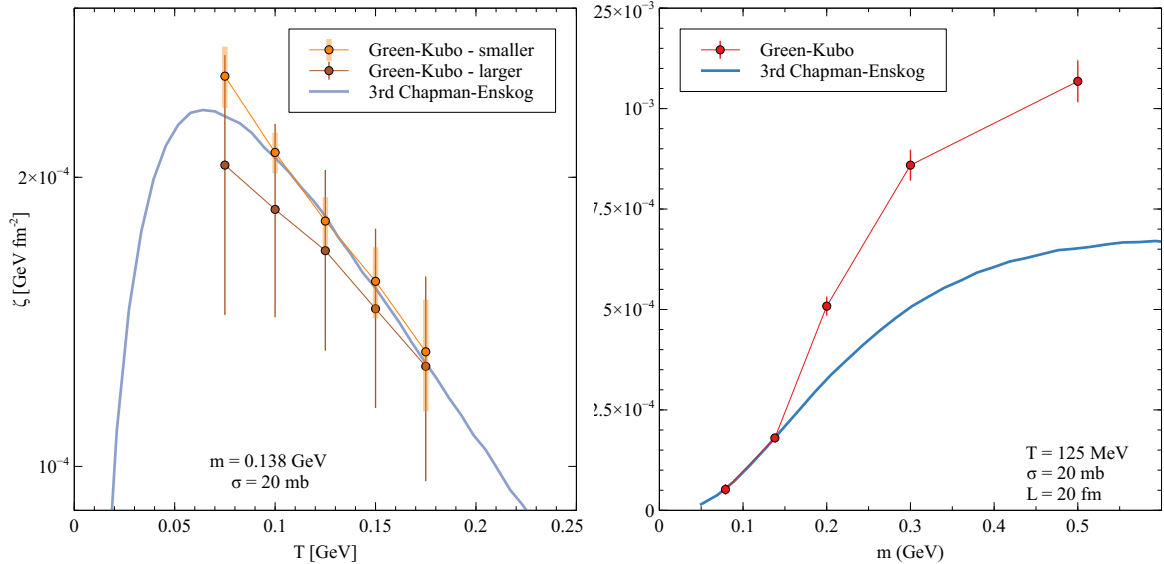


Figure 4.19: Bulk viscosity of a pion gas interacting through constant $\sigma = 20$ fm, as computed with the Green-Kubo formalism and compared to the 3rd order Chapman-Enskog calculation. Left: Bulk vs temperature for two different box sizes: “smaller” corresponds to box lengths, from lower T : 60, 20, 20, 20 and 20 fm, while “larger” has box lengths, from lower T : 200, 100, 60, 40 and 30 fm. Right: Bulk vs mass of the pion.

of $C^{\Pi}(0)$ with the volume V is also roughly constant, we see that reducing the size of the box also reduces the relative error, as the size of the fluctuations with respect to the average pressure diminishes as volume increases. To calculate the bulk viscosity, one then has to strike a balance between having a system which is large enough for thermodynamic quantities to be calculated, but small enough that the signal does not get washed out by the statistical error; note that this volume can also be temperature dependent.

The bulk viscosity of this system as calculated using the Green-Kubo formalism is compared to the semi-analytic Chapman-Enskog expansion in Fig. 4.19 for a variety of temperatures and pion masses. As one can see on the left panel, the agreement is quite good for temperatures between 100 and 175 MeV, even for smaller system sizes. At low temperatures, the agreement starts to break down, and, although not shown here, crumbles completely at even lower temperatures⁹. A possible explanation for this could be that for smaller colder systems, the fluctuations caused by individual collisions become relatively more important, since the density and thus scattering rate is much lower. This could break one of the assumptions that was made in Chapter 2 to obtain the final bulk Green-Kubo equation (4.2), which was that thermodynamical forces (or in this case the corresponding fluctuation) were small; it is as of yet unclear precisely how small this should be, and it is possible that bulk viscosity is more sensitive to this

⁹Although we observe the correlation function to still be exponential in nature at these low temperatures, it simply does not reproduce the CE bulk viscosity.

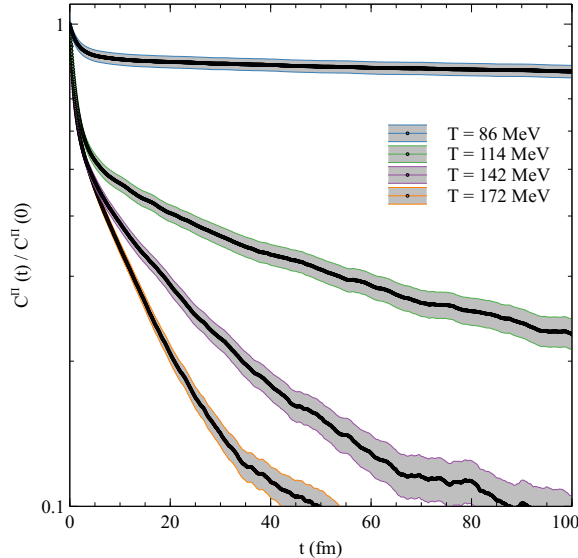


Figure 4.20: Bulk correlation functions for a full hadron gas, where every curve is normalized with its initial value.

than its shear counterpart. Thus it is not unlikely that the Green-Kubo formalism could not be sufficient for the calculation of the bulk viscosity in dilute systems in which the mass of particles is significant with respect to the temperature. This is further reinforced by the right panel of Fig. 4.19, in which, at equal volume and temperature, one sees a disagreement between the Chapman-Enskog and Green-Kubo pictures as the mass increases; this increase of the mass has both the effect of making the gas more dilute (since the thermal density depends on the mass) and to make each collision create fluctuations which are proportionally larger, since individual particles have more impact.

4.3.2 Full hadron gas

Now that a solid baseline has been established for the calculation of the bulk viscosity at temperatures between 100 and 175 MeV using a simple pion gas with constant cross-section, we proceed to the case of the full hadron gas as described by SMASH. Note that in order to calculate the average pressure of this system, we now require simulations to provide at least 5000 fm of equilibrium data; this is extremely costly in terms of computational power, and as such limits the breadth of the exploration of the parameter space.

Let us first consider the normalized (i.e. divided by their value at $t = 0$) correlation functions presented on Fig. 4.20. As is readily visible, these offer a considerably different picture as what we observed in the previous case in Fig. 4.18. First, the statistical errors are here much less significant than they previously were. This is expected, as the introduction of resonances (and thus of mass changing processes)

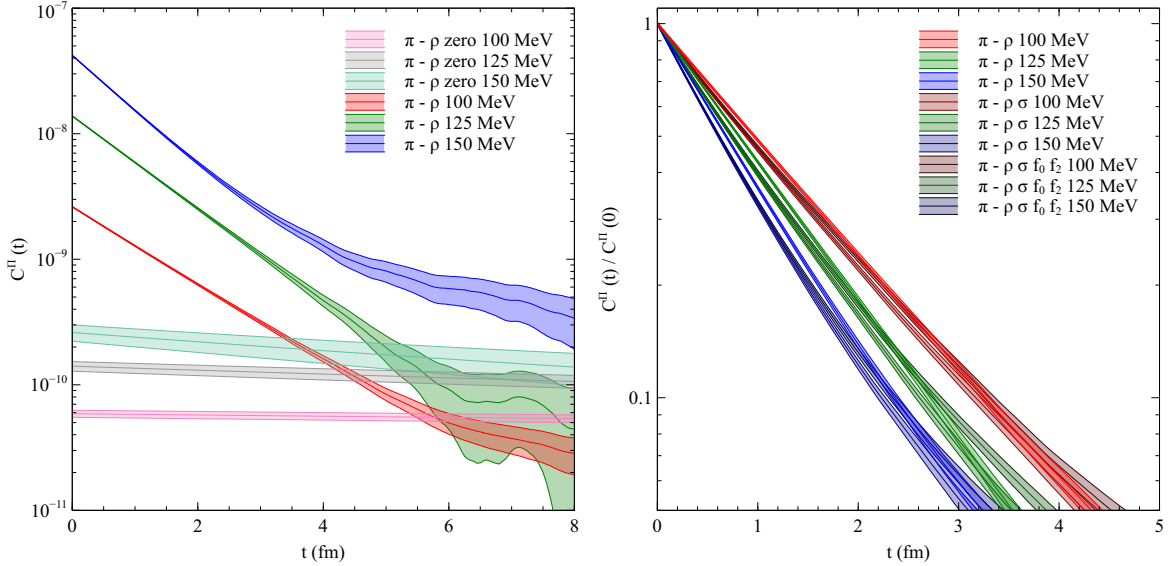


Figure 4.21: Bulk correlation functions for pion gas using the ρ resonance for the cross-section for the cases where the ρ has zero or finite lifetime (left) and for a pion gas interacting through increasing numbers of resonances (right), at various temperatures; the second panel normalizes every curve with its initial value.

leads to a massive increase in the magnitude of the fluctuations with respect to the average pressure, and as such, it should be expected that the error on the pressure should play a lesser role in this case (see left panel of Fig. 4.21 for a concrete example using pions). Second, the correlation functions at all temperatures display a somewhat peculiar shape, as they first observe in the first 2-3 fm a period of rapid decorrelation, followed later on by a less abrupt exponential decay over relatively long times before the relative error finally increases to a point where the signal is dominated by noise.

In order to understand whether this non-exponential shape can be understood physically, we look at a simplified case where pions interact via a rising number of resonances, such as shown on the Fig. 4.21. First looking at the left panel, which shows the correlation function of systems in which the lifetime of the ρ has been taken to zero vs the same system in which it is allowed to propagate, our previous assertions about the importance of including resonances in bulk calculations take their full meaning, where both the initial value $C^{\Pi}(0)$ and the slope of the correlation functions are significantly modified; however, the addition of a single resonance does not appear to produce an inflexion point as we see in Fig. 4.20. This picture changes in the right panel of Fig. 4.21, where increasing numbers of resonances are included in the pion cross-section, and are allowed to propagate. We note that, at any given temperature, as the complexity of the system increases, so does the "curvature" of its correlation functions, which start out with a lightly steeper slope than the one towards which it eventually stabilises. We extrapolate from this picture that as the proportion of the energy of the system which is contained in resonances grows, so does

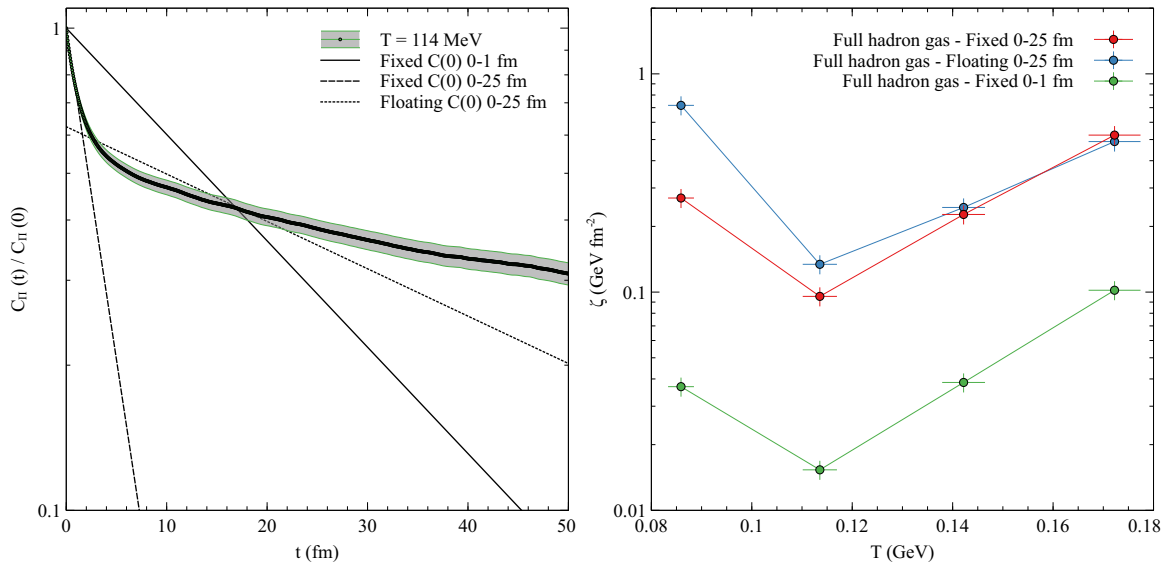


Figure 4.22: Various possible decaying exponential fitting schemes of the correlation function for a full hadron gas at $T = 114$ MeV with curves normalized to their initial value (left) and the resulting bulk viscosity ζ for the different schemes (right).

this early inflexion; note that this picture does not completely rule out the possibility of this inflexion of the distribution being partly or completely due to numerical factors, although the fact that the relative error does not increase significantly with time does lend it some credibility.

The Green-Kubo relation for bulk (4.2) relates the bulk viscosity to the integral of its correlation function. This correlation function only being known at small times, we previously used the exponential decay ansatz to extrapolate it and get a final result. Thus this non-exponentiality of the decay of the correlation function poses a problem when we try to integrate it, as it is unclear how to proceed without employing such an ansatz. For simplicity, we continue to use it to provide at least an idea of the magnitude of the coefficient using this model. To do so, we consider three different exponential fitting schemes: using a fixed intercept, we use the data points from 0-1 fm and 0-25 fm, and using a floating intercept we do the same for the 0-25 fm case; these schemes are illustrated for $T = 114$ MeV in Fig. 4.22, where the left panels shows examples of the various fits compared to one of the correlation functions, and the right panel depicts the corresponding bulk viscosity. The 0-1 fm scheme can be considered as an absolute minimum case, if one completely neglects the late-time inflexion of the distribution; the two 0-25 fm schemes can be seen as a maximum case, albeit not absolute, as the choice to stop the fitting specifically at 25 fm remains somewhat arbitrary.

Maximum and minimum estimates using these three schemes for the bulk viscosity to entropy ratio ζ/s can be found on the left panel of Fig. 4.23, whereas the right panel explores the system size dependence. Both maximum and minimum limits behave in

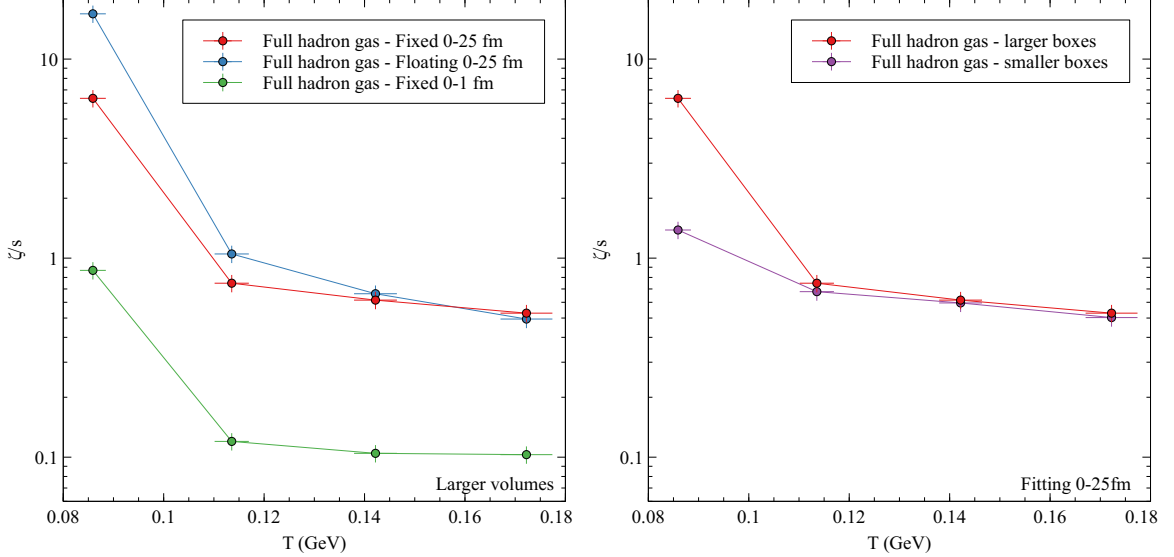


Figure 4.23: Bulk viscosity over entropy density ratio at various temperatures, according to multiple exponential fitting schemes (left) and system size (right). Larger corresponds, from lower T , to box lengths of $L = 100, 60, 40$ and 20 fm, and smaller, similarly, to $L = 60, 40, 20$ and 10 fm.

roughly the same way, with there being a plateau (or slightly decreasing) region from $T = 114$ MeV to $T = 172$ MeV, and the ratio increasing sharply at lower temperatures. This last increase however should be considered with some care, as the unphysical parameter corresponding to the box size still appears to have an influence at the lowest temperatures; note that this discrepancy at low temperature is also compatible with the previously discussed possible breakdown of the validity of the Green-Kubo formalism for the bulk viscosity in cold dilute systems.

4.3.3 Discussion and comparison

In this section we attempt to contextualize the present calculation by testing it against previous calculations of the bulk viscosity or relations involving it.

In a weakly coupled gas, previous calculations using the Boltzmann equation and kinetic theory have shown that the relation between shear and bulk viscosity should be proportional to the squared non-conformality parameter [195, 245, 246]

$$\frac{\zeta}{\eta} \propto (1/3 - c_s^2)^2, \quad (4.11)$$

where we introduced the speed of sound $c_s^2 = \frac{dp}{de}$. Since we now have results for both shear and bulk viscosities, we only need to calculate this speed of sound within SMASH. This is done in Fig. 4.24, where we parametrize the dependence of the pressure to the energy density in order to do so¹⁰. The last panel shows that at least in the high

¹⁰Although the approximate values at high temperature are relatively similar, our results for the

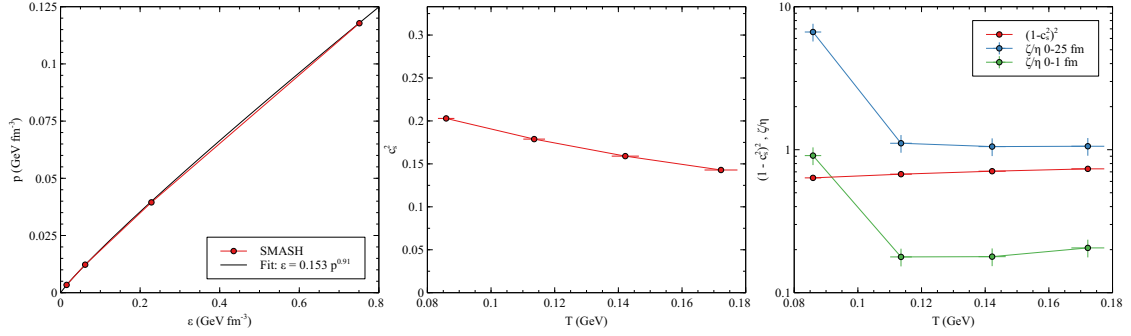


Figure 4.24: Left: pressure vs energy in SMASH, along with an appropriate parametrization. Middle: speed of sound in SMASH vs temperature. Right: proportionality of the bulk to shear viscosity ratio with the squared non-conformality parameter.

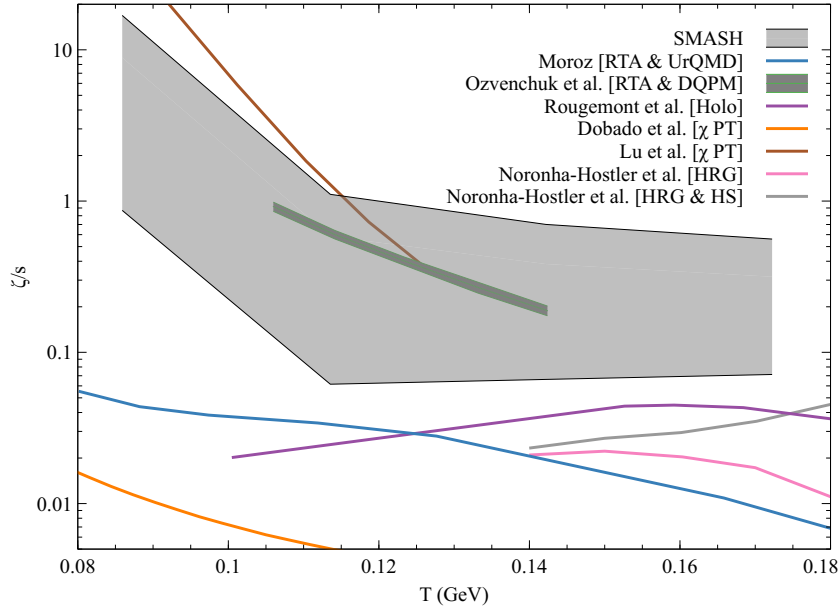


Figure 4.25: Comparison of several calculations for ζ/s at $\mu_B = 0$; see text for details.

temperature plateau region, the proportionality relation between the shear and bulk viscosity does appear to be verified, which further lends credence to the calculation in this region.

Finally, a comparison of available calculations for the bulk viscosity to entropy density ratio is presented in Fig. 4.25. The Moroz [76], Ozvenchuk et al. [81] and Rougemont et al. [88] curves are calculated in a similar way as previously discussed around Fig. 4.13 for the shear viscosity. Noronha-Hostler et al. [103] use a hadron resonance gas model which they supplement with an exponentially increasing density of Hagedorn states (HS), as well as the small-frequency spectral ansatz presented in

temperature dependence of c_s^2 appears inconsistent with previous calculations of it in UrQMD by Bravina et al. [247], which shows an increasing rather than decreasing behavior; this could be explained by the fact that they approximate $c_s^2 \simeq p/e$.

[95] to calculate the bulk viscosity. This calculation is according to the authors to be taken qualitatively rather than quantitatively, to show the effect of including those states; as such, the case without HS appears to be quite similar to our own results, with an approximate plateau being reached from 140 to 170 MeV. As previously, discussed, the Rougemont et al. calculation is performed in the very different framework of holography, and as such is hard to compare to our own results; it is interesting to note that contrarily to almost all the other presented models with the exception of Dobado et al. [106]), this one uses strong coupling and thus predicts a vanishing bulk viscosity to entropy density ratio at very low temperatures.

Dobado et al. [106] and Lu et al. [105] both use the previously mentioned chiral perturbation theory for massive pions (seediscussion around Fig. 4.14) to obtain results for the bulk viscosity, whose validity is usually restrained to lower temperatures than what is shown here [71]. Interestingly however, one sees that although both tend to increase relatively fast in this regime, these two calculations do not really agree with each other, with Dobado et al. being extremely low, while Lu et al. are only slightly larger than the prediction of our own calculation. While the calculation of Lu et al. presents a diverging behavior of ζ at $T = 0$ which was corrected to the limit of zero bulk viscosity at low temperature in Dobado et al. using finite pion chemical potentials, the former also includes number (and thus mass) changing processes, in the form of the $\pi\pi \leftrightarrow \pi\pi\pi\pi$ scatterings, providing a way for energy to be dissipated into mass rather than redistributed into purely kinetic exchanges. As this calculation does not include any kind of resonance, this suggests that bulk viscosity can grow large provided mass-changing processes are present, rather than resonances, whose propagation then rather ensures that energy can be dissipated into mass.

Much more comparable to our own are the remaining two calculations. Interestingly, the PHSD calculation from Ozvenchuk et al. [81] agrees relatively well with our results, which can once again be explained from PHSD also propagating resonances, and thus including mass changing processes. Using their discrete test particle representation, the bulk viscosity is computed from a discretized version of the relaxation time approximation,

$$\zeta = \frac{1}{9TV} \sum_i \frac{\Gamma_i^{-1}}{E_i^2} ((1 - c_s^2)E_i^2 - m_i^2)^2, \quad (4.12)$$

where the sum is taken over all particles in the system, which also includes all the resonances. By contrast, the Moroz calculation uses the relaxation time approximation to calculate analytically the viscosities of the hadron gas in a similar fashion as to what was presented with the Chapman-Enskog formalism in Chapter 2. In this framework, although all resonances are incorporated in the various cross-sections of the collision term, they do not per se exist as propagating particles in the calculation, and only

Particle	Mass (GeV)	Width (GeV)	Present in
π	0.138	0	1,1h,1z,2
η	0.548	0	2
σ	0.800	0.400	2
ρ	0.776	0.149	1,1z*,2
K	0.494	0	1,1h,1z,2
K(892)	0.892	0.050	1,1z*,2
N	0.938	0	1,1h,1z,2
N(1440)	1.440	0.350	1,1z*,2
N(1520)	1.515	0.110	2
N(1535)	1.530	0.150	2
N(1650)	1.650	0.125	2
Δ	1.232	0.117	2
Λ	1.116	0	2

Table 4.1: Properties of particles present in the simpler considered hadron gases: πKN (case 1), $\pi KN - h$ (case 1h), $\pi KN - z$ (case 1z) and $\pi KN\Lambda$ (case 2); asterisks (*) denote a resonance which is used for the cross-section interaction but does not propagate. Many more particles are present in the full hadron gas, see Tables 3.1 and 3.2 for a full list.

binary elastic collisions are considered. In a similar fashion as previously, since resonances are the primary way for energy to be dissipated in something else than kinetic energy and no other mass changing processes are present, the system thus exhibits a much lower bulk viscosity in their absence.

4.4 Cross-conductivity

The previously introduced cross-conductivity $\sigma^{QBS} = (\sigma^{QQ}, \sigma^{QB}, \sigma^{QS})$ is in this section computed according to the Green-Kubo formalism (see Eq. (4.3) at the beginning of the Chapter) following the same general procedure as outlined in Section 4.1. Contrarily to the case of bulk viscosity, no additional technical hurdles must in this case be overcome, and so we can directly present our results.

In the following we will be looking at three different chemical compositions for the hadron gas, all of which are initialized with thermal multiplicities. The first one is a simple mixture of pions, kaons and nucleons, and is the simplest example of a hadron gas containing all three relevant charges (electric, baryonic and strange). In the following pages we will be investigating cases where this gas interacts as hard spheres through constant cross-sections (dubbed $\pi KN - h$), elastically through resonances with zero lifetime ($\pi KN - z$) and through regular resonance formation (πKN)¹¹.

¹¹The difference between the $\pi KN - z$ and πKN cases essentially amounts to what is depicted in the left panel of Fig. 4.6, i.e. pictures in which binary interactions are $2 \rightarrow 2$ vs $2 \rightarrow 1 \rightarrow 2$ in nature.

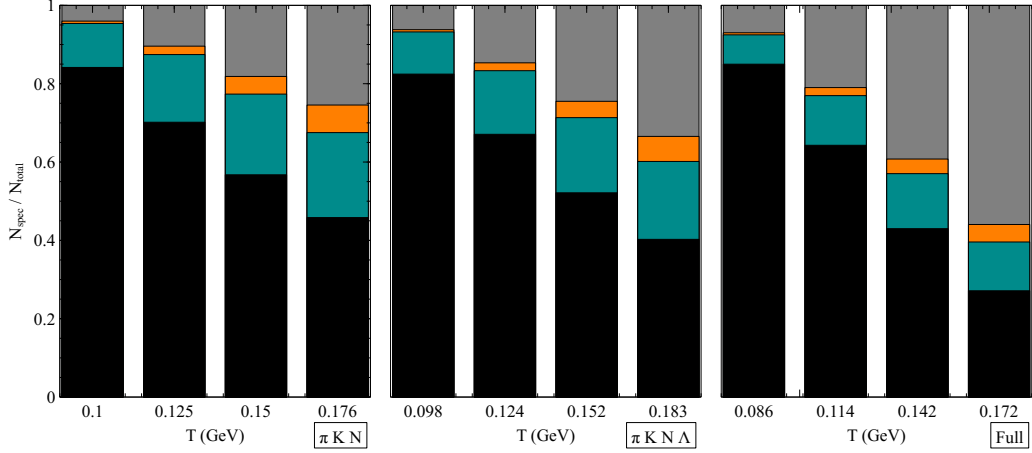


Figure 4.26: Chemical composition of the $\pi K N$, $\pi K N \Lambda$ and full hadron gases at various temperatures. Pions are depicted in black (first from bottom in every column), kaons in dark cyan (second from bottom), nucleons in orange (third from bottom), and all other species compose the grey section (top).

The second one is a mixture of pions, kaons, nucleons and lambdas (which carry both baryonic and strange charge), and which interacts through a larger number of resonances ($\pi K N \Lambda$). The third one consists of the full SMASH simulation, which as previously mentioned includes all particles included by the PDG 2018 recension [213] up to masses of ~ 2.3 GeV. Table 4.1 presents a summary of the present particles and resonances in the first two gases, and Fig. 4.26 an overview of the chemical composition of each gas at various temperatures.

4.4.1 Simple systems

As for the cases of shear and bulk viscosity, we first calibrate non-physical parameters of the Green-Kubo exponential fitting by comparing the result to a semi-analytical calculation based on the Chapman-Enskog formalism [115, 248, 249]. Specifically, as shown on the left panel of Fig. 4.27, we calculate the electric, baryonic-electric and strange-electric conductivities for the previously introduced $\pi K N - h$ hadronic gas with a constant cross-section of 30 mb. We see that the agreement is very strong at all temperatures for the case of the electric and strange-electric conductivities (although the latter appears to be slightly overestimated by the Green-Kubo procedure). The baryonic-electric conductivity shows more variation, especially at low temperatures; this can be attributed in large part to using the same simulations to calculate all three coefficients, and since nucleons have a much higher mass than pions and kaons, there are thus much fewer interactions involving baryons compared to the number of collisions involving only mesons, leading to larger potential systematic errors (especially numerical in this case, as the fluctuations of this correlation function are much smaller

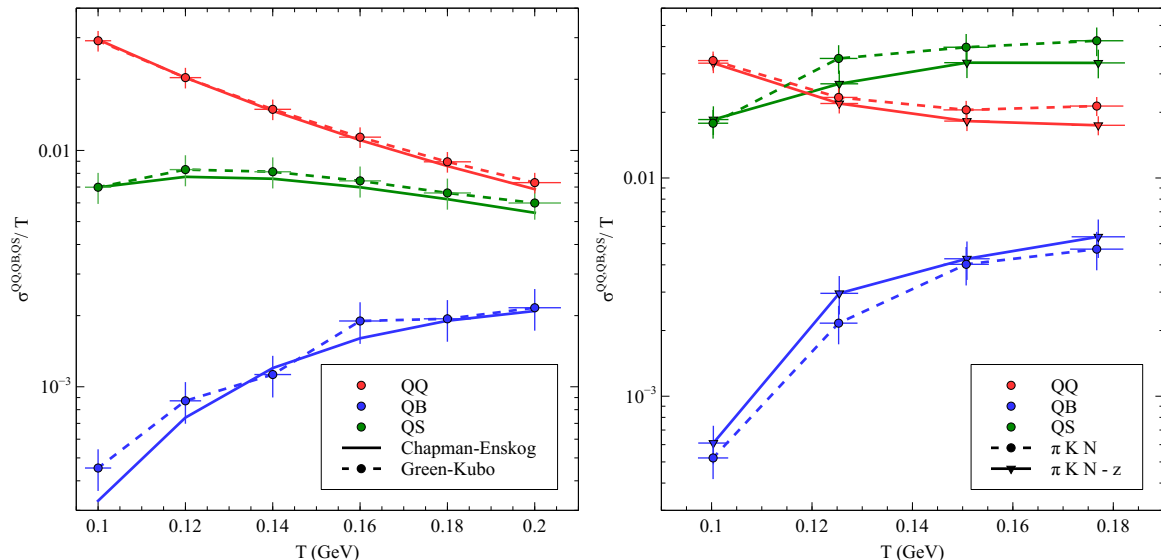


Figure 4.27: Left: Cross-conductivity of a $\pi KN - h$ gas interacting through a constant cross-section of 30 mb, as computed following a Chapman-Enskog approach (dashed lines) and using the Green-Kubo formalism (dotted lines and symbols). Right: Effect of setting resonance lifetimes to zero in a similar resonant gas ($\pi KN - z$ vs πKN ; see text for details).

than for the other two cases). We use this calibration calculation to establish this systematic error to 10% for the electric conductivity, 20% for the baryonic-electric conductivity and 15% for the strange-electric conductivity. Statistical errors are smaller than the symbol size, and are thus neglected for the remainder of this section; all errors on further figures come from this estimation of the systematic error.

Before proceeding further, we note that in the case of the conductivities, contrarily to the previously discussed viscosities, the presence of propagating resonances appears to have a very limited effect on the transport coefficients, as can be seen by comparing the $\pi KN - z$ and πKN cases in the right panel of Fig. 4.27, where for all conductivities there is no significant difference between the two cases within errors at every temperature. Remember notably that in the case of the shear viscosity large effects (up to 50% decrease, see right panel of Fig. 4.6) were observed from setting the lifetime of resonances to zero. This led to suggesting that the redistribution of a conserved quantity allowing for the equilibration of a local perturbation might be effectively blocked within times of the order of the resonance lifetime, which should have a large effect especially at high temperatures, when the resonance lifetime is large enough compared to the mean free time between collisions (see Section 4.2.3 for the full discussion).

This difference in behavior between the different transport coefficients can be explained by looking at the realization of the transport process at the microscopic level. For the shear viscosity one needs to equilibrate the momentum excess of particles

(with respect to the fluid's cell velocity) between different regions. Collisions between particles isotropize the momentum distribution to reach equilibrium. When this mechanism is entirely produced via resonance formation, it is necessary to wait until the formed resonance decays for the total momentum to be distributed between the decay products. Large parts of the real transport is only effective at the moment of the decay, but not before. If the lifetime is larger than the mean-free time, then, on average, it will dominate the value of the relaxation time τ . Although one would think the case of the various currents should follow the same logic, there are some differences when charges enter into play.

If one for example looks specifically at the case of the electric conductivity, from all possible interaction processes, there are several cases in which the equilibration (the disappearance of a fluctuation of the electric current) does not need to wait until the decay of the resonance. An initial fluctuation in the current might vanish at the interaction point, directly upon the resonance creation. As an example, one can think of a local electric current fluctuation due to a $\pi^+\pi^-$ pair with an imbalanced total momentum. At the collision point a ρ^0 resonance with non zero momentum is formed. One might think that the ρ^0 is required to decay into a pair with balanced momentum, to erase the electric current. However, the resonance is charge neutral and the initial fluctuation is already blurred at its formation, so the lifetime does not play any role in the relaxation time. We now instead consider a local current created by a charged and a neutral pion, with a similar momentum but opposed in direction. After they collide, a nearly static charged ρ meson is formed, which will live for some time. But again, the local current decreases close to zero at the formation time. In such a simple hadronic gas, we have many particles of different charges creating local fluctuations and colliding in many different charge combinations. While the whole situation is much more complicated and difficult to analyze, we can still convince ourselves by these examples, that the lifetime of the resonances should here play a relatively minor role as compared to the shear case.

4.4.2 Exploring the parameter space

We now take our attention to the differences between the three previously discussed resonant hadronic gases, and the effect of including a non-zero baryon chemical potential in the full hadron gas. The left panel of Fig. 4.28 takes a closer look at the electric conductivity for all three gases. All three curves show a decreasing behavior as temperature increases, which eventually levels into a plateau around $T = 150$ MeV (and possibly a slight increase onwards for simpler gases; this is consistent with previous calculations [115, 248]). We observe that as the number of degrees of freedom increases in the system, the general observed behavior is a decrease at every temperature, with this decrease being more marked at larger temperatures. This is expected, as adding

more resonances into the gas mostly amounts to increasing the cross-sections of the stable particles (i.e. pions, kaons, nucleons and eventually heavier strange particles such as the Λ). An interesting example of this can be found by looking at the low temperature end of the three curves: there is a marked decrease when going from the πKN to the $\pi KN\Lambda$, but not a large difference between the $\pi KN\Lambda$ and full hadron gas. This can be explained by remembering that at such low temperatures, the vast majority of particles are pions (see Fig. 4.26), and as such the inclusion of the σ resonance (which is the second largest contribution to the total $\pi\pi$ cross-section after the ρ) in the $\pi KN\Lambda$ gas makes a large difference to the total electric conductivity; adding all the other resonances contributing to the $\pi\pi$ cross-section in the full hadron gas still makes a small difference, but its magnitude is much less, since there is simply not enough energy density in the gas to produce these heavier resonances at this low temperature.

The right panel of Fig. 4.28 shows the behavior of the electric conductivity when a non-zero baryon chemical potential is added. As can readily be seen, up to $\mu_B = 300$ MeV, we observe no significant variation of this conductivity at essentially every temperature in the computed range. This effect is similar to what was obtained previously in the case of the shear viscosity to entropy density ratio (see Fig. 4.8), and can be similarly understood: since such an increase in the baryonic chemical potential only corresponds at these temperatures to a modest modification of the relative densities of mesons and baryons (with this difference growing larger at low temperatures), with pions still largely dominating charged particle multiplicities, one should also not expect massive variations in the electric conductivity for such systems. Note that due to an observed loss of the exponentiality of the decay of the correlation function for the different correlations at high μ_B (likely for the same reason as for the shear viscosity, i.e. that large densities lead to a breakdown of the transport description), we do not display any results at chemical potentials larger than $\mu_B = 300$ MeV, as their trustworthiness would be questionable.

The left panel of Fig. 4.29 shows the baryonic-electric conductivity as a function of temperature for the same increasingly complex gases. The general trend is in this case that this conductivity increases with temperature, which is expected as the proportion of baryons in a gas should increase with temperature, since they have a comparatively higher mass than mesons (this is something we do observe in Fig. 4.26). Although large uncertainties blur the picture up to 140 MeV, we once again see an ordering in the three cases, with the baryonic-electric conductivity decreasing as the complexity increases, since, as mentioned previously, one of the main effects of increasing the number of degrees of freedom is to increase the cross-sections of the abundant stable particles. We observe a clear separation between the full hadron gas case and the other two simpler cases at temperatures above 160 MeV, with the full hadron gas

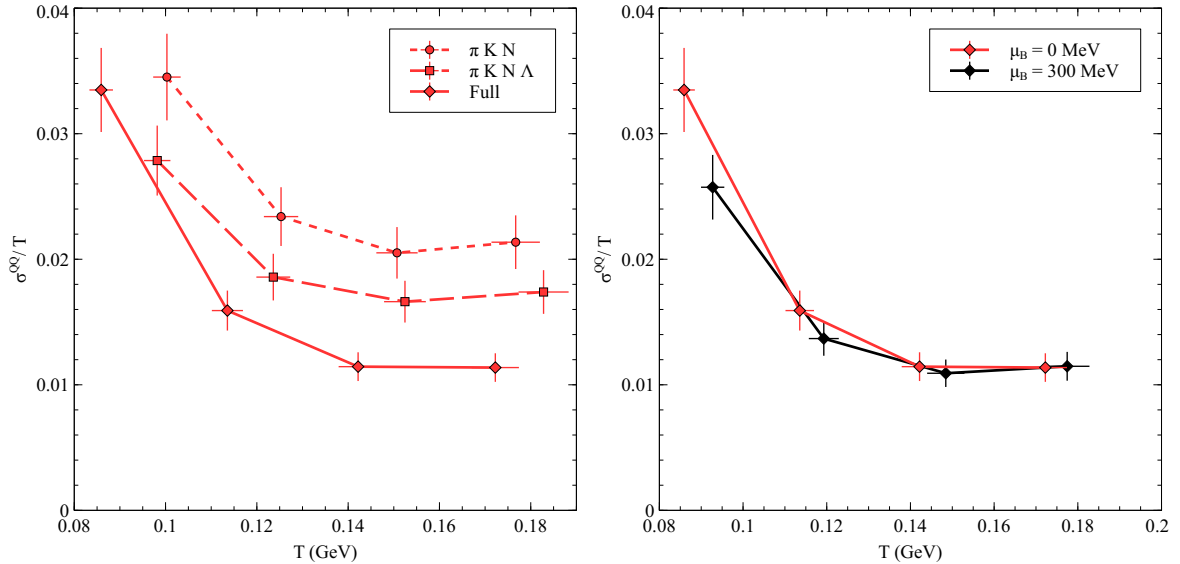


Figure 4.28: Left: Electric conductivity for resonant hadron gases of increasing complexity. Right: Effect of non zero μ_B on the electric conductivity.

being markedly lower, which can be explained by the fact that at these temperatures many heavy baryonic resonances which were not included in the simpler gases become relevant.

We show on the right panel of Fig. 4.29 the effect of including a non zero baryonic chemical potential on the baryon-electric conductivity, which results in a very strong increase at low temperatures. This is very much expected, as this coefficient is essentially designed to be sensitive to changes in baryon densities;. Since the relative baryon and meson densities do not change in a meaningful way at large temperatures for such a low μ_B , we obtain only a moderate effect on σ^{BB} in this range; at low temperature however, the relative density of baryons is much more significant (see Eq. (3.4); this can amount to as much as 20 times as many charged baryons at these low temperatures), which means that the cross-charge effect of applying an electric current perturbation is felt much more keenly in the baryon current, hence an increase in the corresponding conductivity.

Lastly, the strange-electric conductivity as a function of temperature is presented in the left panel of Fig. 4.30. All three curves exhibit a rapidly increasing behavior at low temperature, which then appears to slow down as temperature increases, with all three gases also being fully consistent within uncertainties with reaching a plateau around 120 MeV. This behavior can be understood by looking at the chemical composition of the gases: at low temperature, the proportion of the light strangely charged kaon increases very fast with respect to other types of particles, but eventually slows down because of the inclusion of more and more non-strange heavier particles; a plateau is reached at larger temperatures when similar numbers of strange and non-strange particles are added into the system. This coefficient exhibits a much larger response

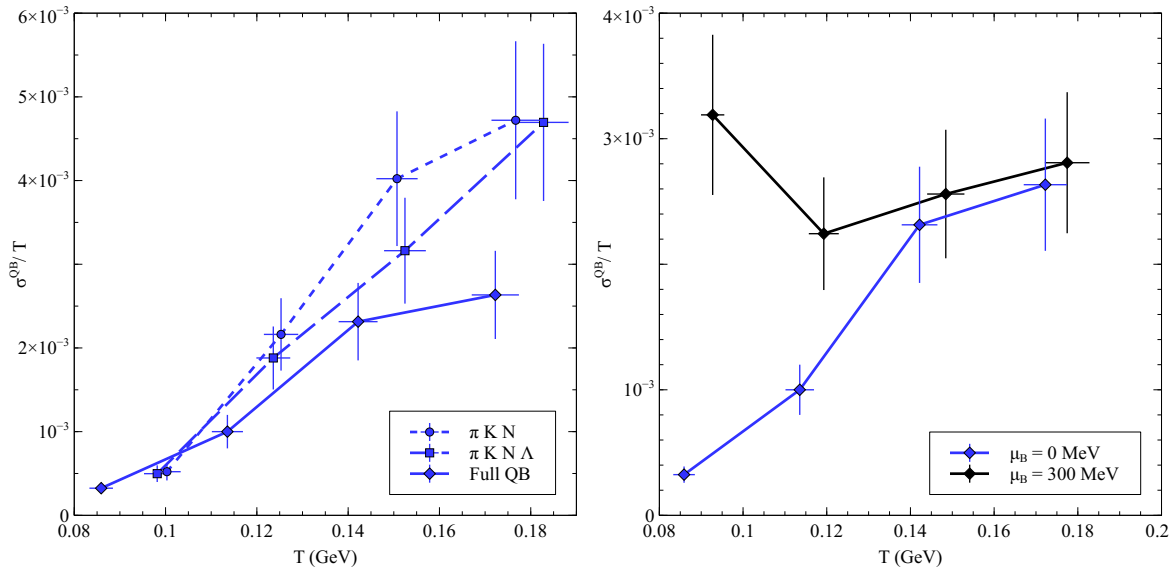


Figure 4.29: Left: Baryonic-electric conductivity for resonant hadron gases of increasing complexity. Right: Effect of non zero μ_B on the baryon-electric conductivity.

to adding large amounts of states into the mixture as the previous ones, as the two simpler cases remain consistent within error bars at all temperatures. We note that a small difference at high temperature between the $\pi K N$ and $\pi K N \Lambda$ cases is most likely due to the introduction of a fourth strange stable particle, the Λ , which becomes more relevant at these high temperatures and could explain the small dip in the value of the strange-electric conductivity. The full hadron gas' conductivity remains resolutely lower, which could be very helpful to discriminate between sufficient and insufficient amounts of states in a given hadron gas model if the exact value of this transport coefficient can be confirmed for example with lattice QCD calculations.

As can be seen on the right panel of Fig. 4.30, we register a slight decrease in the strange-electric conductivity at every temperature when including a 300 MeV chemical potential μ_B , although this decrease is within error bars consistent with there being no effect at all. The same reasoning as for the electric conductivity can here be applied to explain this absence of large effect, with the additional note that since the dominant particle contributing to this coefficient is still the kaon at every temperature, and since the kaon is a meson, seeing a moderate increase in many non-strange (which are more numerous - and lighter - than strange ones) could easily result in a slight decrease of this conductivity.

All three of these conductivities exhibit variations with respect to their hadronic content at various temperatures. As such, these new observables could for example be used to constrain the number of degrees of freedom which are relevant in a wide (T, μ_B) parameter space by comparing the present results with that of other models, for example in lattice QCD. Some calculations of the electric conductivity have actually been performed already on the lattice [107, 124–126]; it should however be noted that

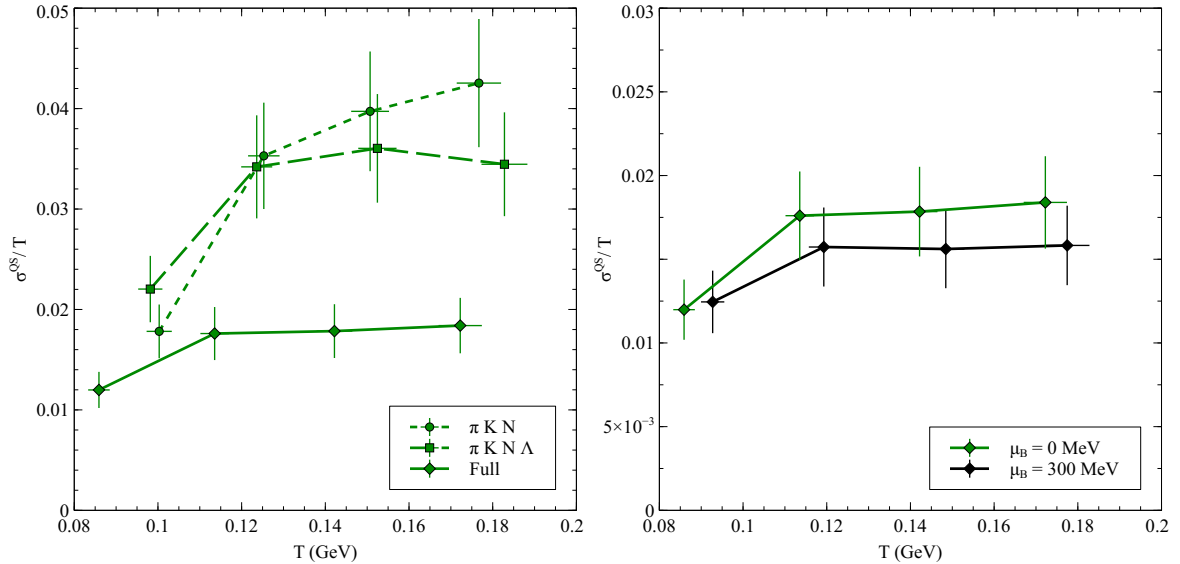


Figure 4.30: Left: Strange-electric conductivity for resonant hadron gases of increasing complexity. Right: Effect of non zero μ_B on the strange-electric conductivity.

comparison with these works is currently ambiguous at best, as the calculations in [124, 125] lack hadronic interactions, those of [126] use unphysical pion masses and finally Ref. [107] does not include any dynamical quarks (quench approximation); to the authors' knowledge, no lattice calculations in which all of these issues have been addressed simultaneously have computed the electric conductivity in our region of interest.

4.4.3 Electric conductivity theory comparison

Although comparison to other models could be arduous in the case of the baryon-electric and strange-electric conductivities since they were first proposed as interesting quantities in this work, such is not the case for the electric conductivity, for which some calculations do exist for the hadronic phase; a selection of these are presented in Fig. 4.31, along with our own results.

The results from Greif et al. [115] use a kinetic approach and a similar approach to linearize the Boltzmann equation as what we discussed in Section 2.2. Their calculation uses a gas of pions, kaons and nucleons which are allowed to interact through energy dependent cross-sections reproducing the Breit-Wigner shape of some common resonances, as well as many constant cross-sections for elastic processes (see Table 1 in [115]). Although the elastic cross-sections which are present in this calculation and those which are generated through the AQM in the case of SMASH are not expected to be the same (or even similar in some cases), this calculation compares advantageously with our own πKN resonant gas, which provides some further (albeit perhaps anecdotal) support to our previous calibration using the non-resonant πKN gas.

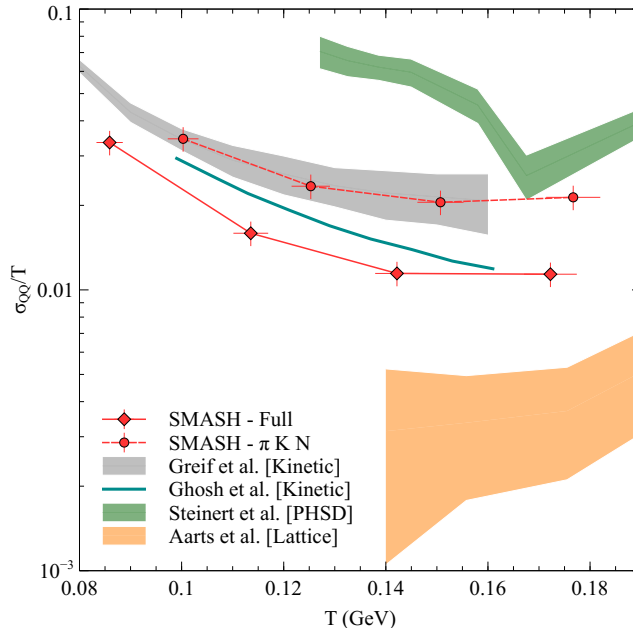


Figure 4.31: Comparison of several calculations for $\sigma_Q Q/T$ at $\mu_B = 0$; see text for details.

Ghosh et al. [133] compute the electric conductivity of a pion gas, also using a similar Chapman-Enskog approach. Although one should not be surprised to see a pion gas and a full hadron gas have different conductivity, they add to their calculation a modification of the cross-sections due to in-medium effects, which they show to have a significant impact, increasing the conductivity by up to 30% around the critical temperature.

Similar in-medium effects are also considered in the calculation of Steinert et al. [118, 119], in which they apply an electric field to a full hadron gas as described by PHSD and compute the conductivity directly from the constitutive relation (2.31). This result is significantly larger than our own, and it is at this time still not completely clear why this should be the case, as PHSD and SMASH are both transport approaches which can to an extent describe the same hadronic phase. It is probable that the previously mentioned in-medium effects, which can in PHSD modify the spectral function of resonances and particles, are partly responsible for the discrepancy, as they should tend to increase the conductivity as found in [133]. Additionally, the applicability of using directly the constitutive relation to calculate the conductivity might be limited, as thermodynamic ensembles tend to develop an internal reaction to being subjected to external electric fields [194], in the form of an internal electric field which then counteracts the external one; the effective electric field felt by particles might then be significantly different from the one which is applied to the system, affecting the calculation of the conductivity.

Finally, we shortly discussed the Aarts et al. [124, 125] lattice QCD results at the

end of the previous section, where we mentioned that the lack of hadronic interactions casts a doubt at the applicability of their method in this temperature regime; note that although not shown here, Brandt et al. obtain very similar results with double the pion mass [126], and Ding et al. [107] do not present any results for the conductivity below the critical temperature. This discrepancies with the purely hadronic descriptions could explain why their conductivity is so much lower than the other presented models, although lattice calculations do in principle remain the most fundamental representation of QCD.

Chapter 5

Jets in the hadronic phase

In this chapter we study the hadron resonance gas' transport properties under a somewhat different angle. As briefly discussed in Section 1.2.4, one of the more prominent subfields of the field of heavy ion collisions is that of “jet quenching,” that is, of how very highly energetic particles and the shower of particles they radiate are affected by traversing some length of the QCD medium. As mentioned in Chapter 1, many descriptions currently exist modeling the various mechanisms by which such high transverse momenta partons (hereafter referred to as high- p_T particles or probes) lose energy in the high temperature QGP phase of the medium, notably through the calculation of the transverse and longitudinal energy loss transport coefficients \hat{q} and \hat{e} . However, the actual value of the hadronic counterpart of these coefficients has not yet been successfully calculated, which is one of the goals of this exploratory study. This additional probe into the hadronic medium also allows us to revisit our shear viscosity calculation, as the transverse energy loss \hat{q} has been directly related at high temperatures to this previously discussed transport coefficient [188], and inspect whether this relation also holds below the phase transition. Finally, we explore angular distributions of momentum (so-called “jet shapes”) in a simple expanding model to show that the hadronic medium can indeed have an effect on the jet substructure observables.

In the following sections we will consider both the box and sphere initialization schemes described in Section 3.2 for the study of high- p_T particles within SMASH. For consistency with the nature of the investigation, string excitation and fragmentation need to be activated, which in principle breaks the detailed balance requirement for thermodynamic quantities to be conserved in the box setup. Since we will however only be interested in what happens at relatively early times (typically less than 10-20 fm), we simply neglect this effect (over such times, the temperature typically will not decrease by more than 3%).

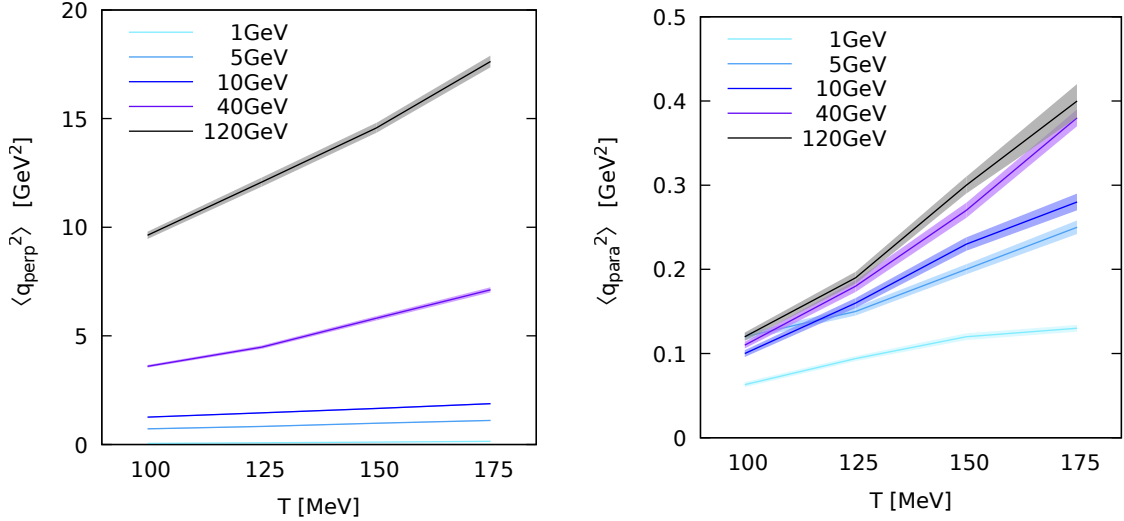


Figure 5.1: Transverse (left) and longitudinal (right) momentum vs temperature for various high- p_T particle momenta.

5.1 Energy loss in the hadronic medium

We introduce a high- p_T particle in the previously discussed box simulating infinite matter and analyse only its first interaction with the medium averaged over many simulations. This is significantly different to what is normally done in the QGP, where the interaction of such particles with the medium is often modeled through a succession of small momentum kicks over some distance. The reason for this change is twofold. First, in a hadronic transport approach, inelastic collisions are not only possible but frequent (typically in the form of a string excitation, see Fig. 3.3), resulting in the loss of the original particle and thus making it impossible to continue to follow it. Second, even in the cases where the first interaction is elastic, it will typically not be in the form of many relatively small kicks to the particle; in this case, a single collision can strongly affect the momentum of the high- p_T particle, and as such its final longitudinal momentum can vary a lot, making it difficult to compare subsequent collisions. By only studying the first collision, the control parameters are kept fixed.

In the QGP phase, \hat{q} is typically estimated from kinetic theory [250],

$$\hat{q} = \rho \int q_{\perp}^2 \frac{d\sigma}{dq_{\perp}^2} dq_{\perp}^2, \quad (5.1)$$

where ρ is the number density of the system, q_{\perp} is the transverse momentum transfer and $d\sigma/dq_{\perp}^2$ is the differential cross-section of the particle with the medium. Since in SMASH the cross-section only depends on the properties of the incoming particles, the quantity $d\sigma/dq_{\perp}^2$ in this definition is consistent with zero, leading to the conclusion that Eq. (5.1) should not be used in this context. However, this does not mean that

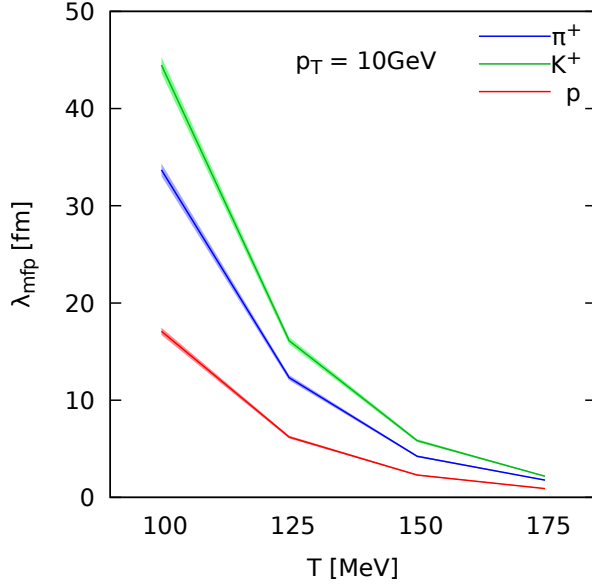


Figure 5.2: Mean free path vs temperature for various high- p_T particle species.

it is not possible to describe the energy loss in the hadronic medium. At the most fundamental level, the transverse and longitudinal energy losses are simply

$$\hat{q} = \frac{\langle q_{\perp}^2 \rangle_L}{L}, \quad \hat{e} = \frac{\langle q_{\parallel}^2 \rangle_L}{L}, \quad (5.2)$$

where $\langle q_{\perp}^2 \rangle_L$ and $\langle q_{\parallel}^2 \rangle_L$ are the average cumulative transverse and longitudinal momentum change suffered by a propagating particle in a medium over a length L . As previously mentioned, this typically assumes that the medium acts through many small elastic scatterings on the particle; this is not quite valid in the case of the hadron gas, as we rather usually observe one very large (and likely inelastic) momentum influx. To account for these differences in the description, we propose the following definitions for similar quantities denoted as \tilde{q} and \tilde{e} ,

$$\tilde{q} = \frac{\langle q_{\perp}^2 \rangle}{\lambda_{mfp}}, \quad \tilde{e} = \frac{\langle q_{\parallel}^2 \rangle}{\lambda_{mfp}}, \quad (5.3)$$

where $\langle q_{\perp}^2 \rangle$ and $\langle q_{\parallel}^2 \rangle$ are now the average transverse and longitudinal momentum of the first collision with the medium, and λ_{mfp} is the mean free path of the high- p_T particle before this first interaction.

The left panel of Fig. 5.1 shows the effect of varying the energy of the high- p_T particle on $\langle q_{\perp}^2 \rangle$, which is shown to increase with temperature at every energy; moreover, the effect of temperature appears to be markedly more important as the energy of the particle increases. The right panel shows a similar picture for the longitudinal case, where we also see $\langle q_{\parallel}^2 \rangle$ increase with temperature at every energy; note however that

in this case there is already a relatively strong temperature dependence even at low beam energies. Fig. 5.2 shows that the choice of species for the high- p_T particle has a large impact on its mean free path, which mainly comes from the fact that cross-sections depend quite strongly on the type of particle. Although not shown here, the temperature dependence of the transverse and longitudinal momenta are as expected very similar for each species, pointing to a main kinematic effect. In fact, the longitudinal momentum transfer is much smaller than the transverse one due to momentum conservation. Since the high momentum probe has initially rather high momentum, there has to be a significant amount maintained in the longitudinal direction, while any re-distribution into the transverse plane implies a large change since the transverse momentum is zero before the scattering. The mean free path on the other hand is in comparison insensitive to the energy of the particle, as expected from the invariance of the string fragmentation versus the particle species and from the fact that the average cross-section only slightly varies with the energy of the particle (see for example Fig. 3.3).

Using this prescription, we explore the temperature and particle energy dependence of \tilde{q} and \tilde{e} for the specific case of a high- p_T pion (Fig. 5.3). As one readily sees, we observe that both \tilde{q} and \tilde{e} increase significantly both with temperature and particle energy. This parameter space exploration allows us to introduce the following parametrizations (also shown on the figures) to estimate the value of the hadronic transverse and longitudinal energy losses at temperatures between 100 and 175 MeV, for particles with momenta between 1 and 120 GeV:

$$\tilde{q}_\pi(p_T, T) = 5.14 \cdot 10^{-18} \frac{\text{GeV}^2}{\text{fm}} \left(\frac{p_T}{\text{GeV}} \right)^{0.87} \left(\frac{T}{\text{MeV}} \right)^{7.35}, \quad (5.4)$$

$$\tilde{e}_\pi(p_T, T) = 9.31 \cdot 10^{-19} \frac{\text{GeV}^2}{\text{fm}} \left(\frac{p_T}{\text{GeV}} \right)^{0.17} \left(\frac{T}{\text{MeV}} \right)^{7.59}. \quad (5.5)$$

We observe that while both these quantities depend on the momentum of the high-energy particle, the dependence is much stronger in the case of the transverse coefficient. These parametrizations can be directly employed in future studies of hadronic jet quenching.

Although it is not yet completely clear that the hat and tilde definitions are equivalent, we attempt a comparison between numerical values. In the QGP, a cross-model study [187] (see Fig. 1.4) has recently found that $\hat{q} = 1.9 \pm 0.7 \text{ GeV}^2/\text{fm}$ at $T=470 \text{ MeV}$ and $\hat{q} = 1.2 \pm 0.3 \text{ GeV}^2/\text{fm}$ at $T=370 \text{ MeV}$ [187] for a 10 GeV quark traveling through the medium. Our approach shows that for a pion with the same energy in a relatively hot hadronic medium at 150 MeV (i.e. just below the phase transition), we obtain from (5.4) that $\tilde{q} = 0.38 \text{ GeV}^2/\text{fm}$. This result, while as expected below its QGP counterpart, does remain significant, as will be discussed in Section 5.2.

In [188] it is suggested that a heuristic connection between η and \hat{q} can be es-

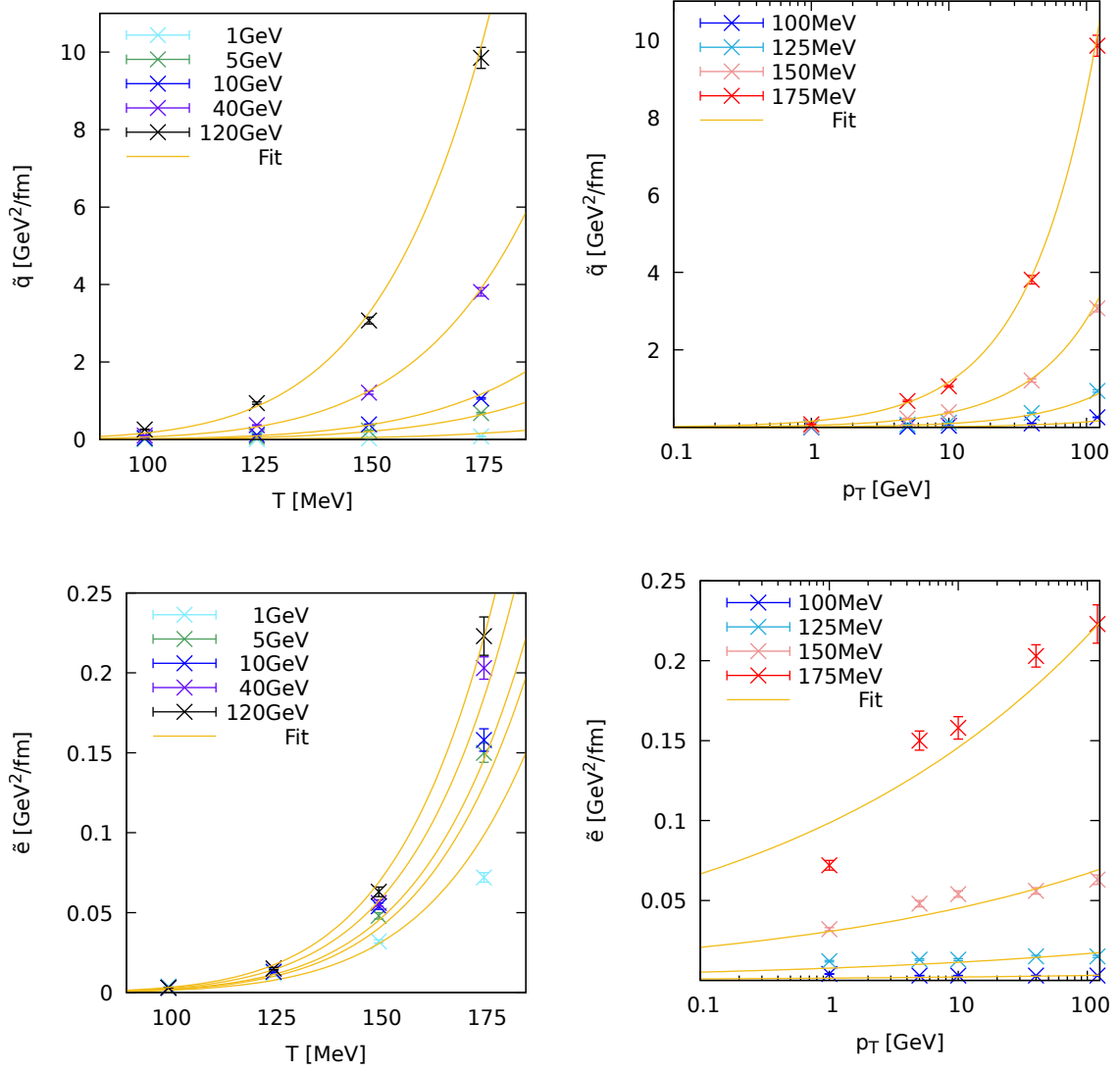


Figure 5.3: Medium modification factor \tilde{q} as a function of temperature and high- p_T pion momentum. Lines show the fit of parametrizations (5.4) and (5.5).

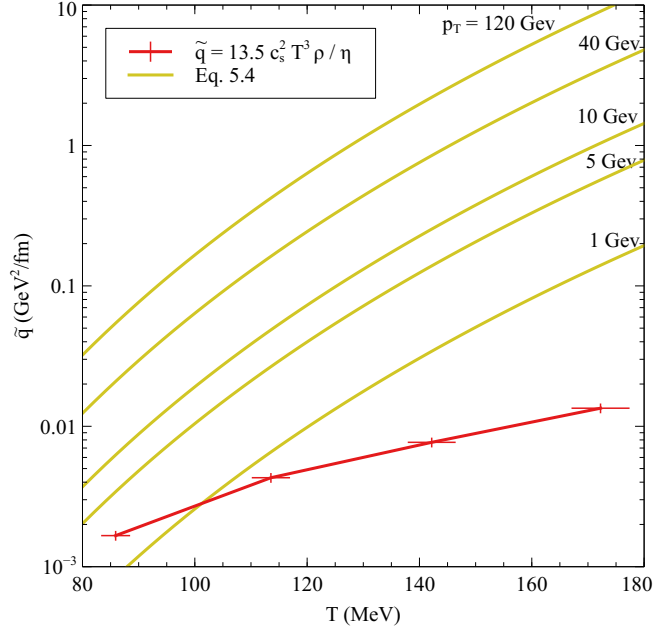


Figure 5.4: Transverse energy loss \tilde{q} as computed from our previous shear viscosity results; the yellow lines correspond to various probe energies using the (5.4) parametrization.

established. This relation was developed in a context where soft scatterings dominate, which, as mentioned previously, is far from the case in the hadron gas as described by SMASH. Specifically, in the case of massless particles, it is shown that

$$\eta \approx 13.5 c_s^2 \frac{T^3 \rho}{\hat{q}}, \quad (5.6)$$

where $c_s^2 = \frac{dp}{de}$ is the previously introduced speed of sound (see discussion around Fig. 4.24). Although we are here also not dealing with a massless gas of particles, in principle this assumption could hold for very high- p_T particles, as the mass of the medium particles would then be negligible with respect to the high momentum of this probe.

Since our direct results for \tilde{q} are dependent on the probe energy and the shear viscosity is not, it would be difficult to expect a direct correspondence between the previously presented parametrization and the transverse energy loss parameter that we can obtain using the shear viscosity calculated in Chapter 4. However, we still proceed with the comparison in the spirit of extracting some additional insights. Using the full hadron gas results (including AQM) that were presented in Fig. 4.15, we thus proceed to use Eq. (5.6) to provide another calculation of \tilde{q} . As one readily sees, the obtained transport coefficient is very low compared to our previous calculation, with it being up to three orders of magnitude smaller than the highest values obtained at high temperature with a very energetic probe. Interestingly, as mentioned, the highest $p_T = 120 \text{ GeV}$ particle should in principle see the gas as essentially massless, which

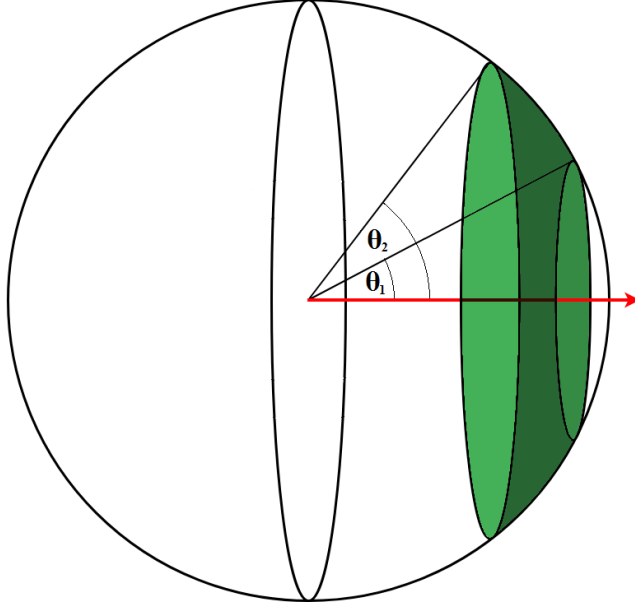


Figure 5.5: Illustration of the solid angle around the direction of initial propagation (red arrow).

makes it the closest conceptually to the framework in which Eq. 5.6 was developed. It should be noted that in [188] it is mentioned that systems which are strongly coupled (for example those in which confinement is present, such as the hadron gas) should exhibit a much larger viscosity than what the heuristic predicts, which is in this case quite true; it is suggested that this could be a way to ascertain the strength of the underlying QCD coupling. We additionally note that while the \tilde{q} predicted through the relation with the shear viscosity does increase with temperature, it does not appear to match the slope of our very fast rising previous calculation, leading to the observation that these two methods also do not produce results which are simply proportional to each other. This means that some additional factors which take into account the hard scatterings and non-zero masses need to be included for this heuristic to really hold in the hadronic phase.

5.2 Jet Shapes

Now that we quantified the energy loss of a high- p_T particle through the hadron gas and found it to be smaller than its QGP counterpart, but not to the point of insignificance, we demonstrate that the hadronic medium has an effect on the angular momentum distributions of shooting a single high- p_T particle through it.

In this section we add a high- p_T particle in the middle of the previously described thermally initialized sphere at a temperature of $T = 150$ MeV, and measure the angular distribution at large times, after freeze-out. To some extent, one can consider this scenario as similar to what would happen to a high- p_T particle in the late stages of

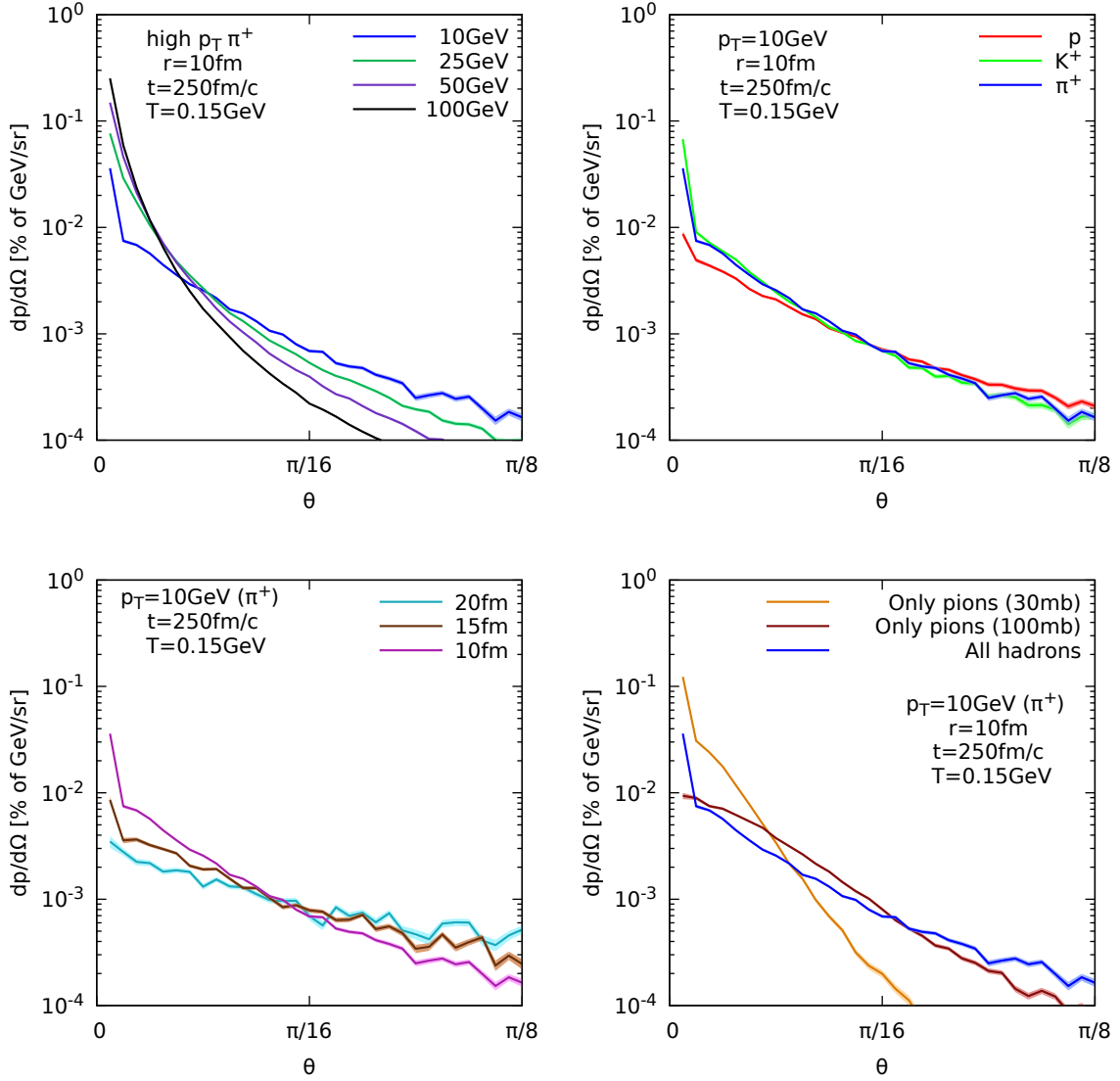


Figure 5.6: Jet shapes as a function of leading particle energy (top left), leading particle species (top right), medium size (bottom left). The bottom right plot compares the full hadron gas jet shape to that of a pion gas with constant cross-section.

a heavy ion collision, after the hadronization has taken place: at that point, it crosses a rapidly cooling and decreasingly dense hadronic medium; the main difference is here the absence of flow. It is not trivial to predict how flow would affect these distributions at all energies. On the one hand, such an outwards movement of the particles will lead to a faster cooling and eventual freeze-out of the sphere; on the other, depending on the momentum of the high- p_T particle, there are some cases in which lower p_T particles would have a larger average cross-section with the medium since they would now be more likely to be (at least partially) comoving (see Fig. 3.3 at $\sqrt{s} = 10$ GeV or lower, for example). Thus, while in the high- p_T limit our results should represent a maximum as to what effect can be expected, the situation is not so clear at lower momentum.

We determine the angular momentum distribution, or jet shapes, shown in Fig. 5.6

by measuring the amount of energy such a high- p_T particle adds on average at an angle θ of its original propagation direction. Specifically, this is done by simulating both a set of spheres in which this high- p_T particle is present and one in which it is absent. At a given angle θ_1 corresponding to a solid angle Ω (see Fig. 5.5), the momentum $dp/d\Omega$ of the latter is subtracted from the momentum of the first, in what can be thought of as a background subtraction. We then normalize this by dividing it by the maximum value it could take, i.e. if all the momentum was still at $\theta_1 = 0$ (which corresponds to the case where the particle flies out of the medium without interacting). This gives us a quantity which can be compared for a wide variety of scenarios.

The top left panel of Fig. 5.6 explores the energy dependence of the high- p_T particle. As one can readily see, less energetic particles tend to affect the momentum distribution at wider angles than their more energetic counterparts. This is expected, as we would indeed think that a 100 GeV particle, even if it does interact with the medium, should retain or transfer most of its momentum in the initial direction of propagation when colliding elastically or inelastically with a medium component with energy of the order of 1-3 GeV. Conversely, using the same considerations, a much larger part of the momentum is found at wider angles in the case of a 10 GeV particle. The peak around zero angle, e.g. for the 10 GeV probe, reflects the particles that escape from the medium without any disturbance.

We see in the top right panel of Fig. 5.6 that various species of particles are differently affected by the hadronic expansion. This is due to different hadrons having on average larger or smaller cross-sections with the particles of the medium. Remembering the discussion about the Additive Quark Model in Section 3.5.7, we then see that the proton, as a baryon, typically has larger cross-section with the medium, and its jet shape is more skewed towards larger angles; the pion shape is less affected, but still slightly more so than the strange kaon one, with the smallest average cross-section.

The medium size dependence (here probed through varying the radius of the initial expanding sphere) is inspected in the bottom left panel of Fig. 5.6. As one would expect, increasing the size of the medium (and thus the number of possible collisions between the high- p_t and medium particles) generally broadens the angular distribution. Note that while the size of the hadronic part of the medium in heavy ion collisions is not precisely known, estimations usually place it between 10 and 15 fm [251].

Finally, the bottom right panel compares shooting a high- p_T pion through a full hadron gas as described by SMASH and through a much simpler pion gas interacting only through constant cross-sections, which corresponds in essence to the hard spheres scenario. Although the 30 mb case is much closer to the actual average cross-section the pion would encounter in a full hadron gas, we see that the angular distribution of the 100 mb case is in fact much closer to that of the full hadron gas due to the much

larger density than in the pure pion gas. In order to get an intuition of the degree at which the 30 mb and 100 mb cases differ, we calculate the proportion of volume at thermal densities which is occupied by particles in this hard sphere scenario. For an initial temperature of 150 MeV, we thus see that $\sim 5\%$ of the volume is occupied in the case of the 30 mb cross-sections, whereas $\sim 33\%$ of space is filled in the case of the 100 mb cross-sections. Although this is a simplified model, it should provide the reader with some sense of how dense such a hadron gas still is at the time of hadronization.

This explorative investigation shows that the angular distributions can be affected by the hadronic phase rescatterings in a significant manner. In particular, let us note that fully reconstructed jets rely on information of particles at much lower transverse momenta as well. Since the probe hadron would be of similar energy as the medium particles, making it hard to distinguish it clearly, in our radially expanding sphere it does not make sense to lower the momenta beyond the displayed 10 GeV. However hadrons around 2 GeV of energy would certainly be re-shuffled and found at different angles than without hadronic rescattering, sizeably affecting the tail of the distributions of observables such as the ‘jet shapes’ computed in [163, 177, 252–255].

Chapter 6

Summary

In this work we provided additional insights into our understanding of bulk QCD matter through the study of the transport coefficients which govern the non-equilibrium microscopical processes of statistical ensembles. Specifically, we focused on the low energy regime corresponding to the hadron gas, as the properties of this region of the phase diagram are still relatively unknown, and existing calculations for the transport coefficients are either scarce, contradictory, or somewhat limited in scope; this thesis' main goal was thus to shed some light on this by providing new independent calculations of these quantities.

We subsequently presented two formalisms which can be used to calculate transport coefficients. The first one (which also was the main tool we used in the following chapters to produce our results) relies on the development of so-called Green-Kubo formulas, which relate non-equilibrium dissipative fluctuations with transport coefficients; notably, the off-diagonal components of the energy-momentum tensor are shown to be related to the shear viscosity, its diagonal components to the bulk viscosity and fluctuations in the electric current can be related to the electric conductivity. We additionally introduced two new conductivities, namely the baryon-electric and strange electric conductivities, which we dubbed, together with the already known electric one, the “cross-conductivity”, which encodes information about how electric fluctuations are correlated to changes in electric, baryonic or strange currents, or vice-versa. The second way of calculating transport coefficient which we discussed consists in linearizing the collision term of the Boltzmann equation through the Chapman-Enskog formalism. While in principle providing direct semi-analytical results for the transport coefficients, this approach is complicated to implement when more than a few species are considered, and as such was then mostly used as a tool to calibrate our Green-Kubo calculations.

The hadron gas model that we used for all calculations, namely the transport approach SMASH, was then presented. The main features of the model were explained, such as the collision criterion, the considered degrees of freedom and the specific way

in which they microscopically interact with each other. It was verified that SMASH does reproduce analytical results of the Boltzmann equation in an expanding universe scenario, thus showing the equivalence of this transport approach and the associated kinetic theory results. A special care was taken to detail the ways in which a state of thermal and chemical equilibrium (which is necessary for Green-Kubo relations to be valid) can be reached and described using SMASH.

We then presented the decaying exponential ansatz to help calculate the Green-Kubo correlation functions, which allows one to solve the integrals at the cost of introducing some systematic errors. After full systematic studies, the shear viscosity η , bulk viscosity ζ and cross-conductivities ($\sigma^{QQ}, \sigma^{QB}, \sigma^{QS}$) were calculated, compared to previous calculations, and comments on the properties of the transport coefficients and their dependencies were made. It is shown that the detailed microscopic way in which interactions between particles are performed in different models can have a large impact on some coefficients; notably, the implementation of resonance lifetimes appears critical for the appropriate treatment of the shear viscosity, while we saw that the bulk viscosity necessitates mass changing processes (for example through propagating resonances, but not limited to them) to be present in order to be fully consistent. Interestingly, the conductivities show much less sensitivity to the treatment of resonances; it is shown that increasing the number of degrees of freedom leads to differences in the temperature dependence of the conductivities, such that future calculations of those quantities on the lattice could help constrain some properties of hadron transport approaches.

Although a significant step in the direction of better understanding the non-equilibrium properties of the hadron gas, these results can however still definitely be improved. The largest contributor to the uncertainty of the transport coefficients is in this case the exponential *ansatz* which we used throughout Chapter 4; this approximation is in many cases simply not valid anymore, for example in the high density systems found at very high temperature or chemical potential μ_B , or even at lower densities as we saw in the case of the bulk viscosity. Since the errors on the correlation function increase rapidly at large times, it is as of yet unclear how this calculation could be performed without such an *ansatz*. On the side of the hadron gas modeling, several improvements are also expected to have a significant impact on the calculation of the shear viscosity. In particular,

1. The inclusion of medium broadening on the spectral functions of resonances could most definitely have an impact on several of these coefficients. This has already been shown to increase the electric conductivity in simple systems [133], and a similar effect was theorized to partly explain the differences between our results and those obtained using PHSD, another transport approach in which those medium effects are modelled [119]. Interestingly, the same medium modifications

to the spectral functions would also effectively reduce the lifetime of resonances at high temperatures, which, according to our results, would instead decrease the shear viscosity; It will be interesting to see such a feature studied in detail, as different effects can be expected from its inclusion on calculation of the various coefficients.

2. All the interactions we used in our calculations were isotropic in order to preserve detailed balance. However, as briefly discussed in the case of the shear viscosity of a simple $\pi - \rho$ gas, the inclusion of anisotropies in such interactions can be expected to produce large effects (in this gas, we argued that the shear viscosity of such a p -wave would be $5/3$ larger than in the isotropic case), and it should also have an effect on other gases and coefficients.
3. At high temperatures and baryon chemical potential, as density rises, it should be expected that multiparticle interactions start to be relevant, as the *Stosszahlansatz* and thus the applicability of the Boltzmann equation start to break down. Although such interactions are expected to accelerate the reshuffling of momenta and thus to reduce the value of transport coefficients, the magnitude of the influence of these non-binary collisions on the linear response coefficients is as of yet not very well known.

To turn this around, when more precise values of these coefficients are extracted from experimental data, they can then also be used to impose some constraints on this modeling.

Finally, in our final chapter we accessed the hadron gas properties through a somewhat different approach by shooting high- p_T particles through a hadronic gas, in order to calculate for the first time a hadronic equivalent to the jet quenching parameters \hat{q} and \hat{e} . These hadronic transport coefficients are dubbed \tilde{q} and \tilde{e} , and their value is calculated to be approximately 3 to 4 times smaller than their QGP counterparts; while effects on jet observables from this should thus be more limited, this is by no means negligible, which we show by studying the angular distribution of momentum (or jet shape) of a high- p_T particle flying through an expanding sphere. While this is beyond the scope of this initial study, the logical next step to verifying whether hadronic considerations are relevant to the jet quenching framework could also be to be performed in full heavy ion simulations, complete with jets that first go through a QGP phase and then move on to cross a hadronic afterburner, for example within the JETSCAPE framework [209]. We finally comment that although there is a heuristic connection between the shear viscosity η and transverse parameter \hat{q} in the QGP, this appears not to be the case in the lower temperatures corresponding to the hadron gas, although a different relationship still might exist.

Bibliography

- [1] M. Srednicki, *Quantum Field Theory*. Cambridge University Press, 2006.
- [2] A. Deur, S. J. Brodsky, and G. F. de Teramond, “The QCD Running Coupling,” *Prog. Part. Nucl. Phys.*, vol. 90, pp. 1–74, 2016.
- [3] Y. Aoki, G. Endrodi, Z. Fodor, S. D. Katz, and K. K. Szabo, “The Order of the quantum chromodynamics transition predicted by the standard model of particle physics,” *Nature*, vol. 443, pp. 675–678, 2006.
- [4] J. D. Edelstein, J. P. Shock, and D. Zoakos, “The AdS/CFT Correspondence and Non-perturbative QCD,” *AIP Conf. Proc.*, vol. 1116, no. 1, pp. 265–284, 2009.
- [5] I. Arsene *et al.*, “Quark gluon plasma and color glass condensate at RHIC? The Perspective from the BRAHMS experiment,” *Nucl.Phys.*, vol. A757, pp. 1–27, 2005.
- [6] B. Back, M. Baker, M. Ballintijn, D. Barton, B. Becker, *et al.*, “The PHOBOS perspective on discoveries at RHIC,” *Nucl.Phys.*, vol. A757, pp. 28–101, 2005.
- [7] J. Adams *et al.*, “Experimental and theoretical challenges in the search for the quark gluon plasma: The STAR Collaboration’s critical assessment of the evidence from RHIC collisions,” *Nucl.Phys.*, vol. A757, pp. 102–183, 2005.
- [8] K. Adcox *et al.*, “Formation of dense partonic matter in relativistic nucleus-nucleus collisions at RHIC: Experimental evaluation by the PHENIX collaboration,” *Nucl.Phys.*, vol. A757, pp. 184–283, 2005.
- [9] K. Aamodt *et al.*, “Elliptic flow of charged particles in Pb-Pb collisions at 2.76 TeV,” *Phys. Rev. Lett.*, vol. 105, p. 252302, 2010.
- [10] S. Chatrchyan *et al.*, “Multiplicity and Transverse Momentum Dependence of Two- and Four-Particle Correlations in pPb and PbPb Collisions,” *Phys. Lett.*, vol. B724, pp. 213–240, 2013.

- [11] G. Aad *et al.*, “Measurement of the pseudorapidity and transverse momentum dependence of the elliptic flow of charged particles in lead-lead collisions at $\sqrt{s_{NN}} = 2.76$ TeV with the ATLAS detector,” *Phys. Lett.*, vol. B707, pp. 330–348, 2012.
- [12] P. F. Kolb and U. W. Heinz, “Hydrodynamic description of ultrarelativistic heavy ion collisions,” 2003.
- [13] T. Schafer and D. Teaney, “Nearly Perfect Fluidity: From Cold Atomic Gases to Hot Quark Gluon Plasmas,” *Rept.Prog.Phys.*, vol. 72, p. 126001, 2009.
- [14] S. Borsanyi, Z. Fodor, C. Hoelbling, S. D. Katz, S. Krieg, and K. K. Szabo, “Full result for the QCD equation of state with 2+1 flavors,” *Phys. Lett.*, vol. B730, pp. 99–104, 2014.
- [15] A. Bazavov *et al.*, “Equation of state in (2+1)-flavor QCD,” *Phys. Rev.*, vol. D90, p. 094503, 2014.
- [16] A. Bazavov *et al.*, “The QCD Equation of State to $\mathcal{O}(\mu_B^6)$ from Lattice QCD,” *Phys. Rev.*, vol. D95, no. 5, p. 054504, 2017.
- [17] A. Bashir, L. Chang, I. C. Cloet, B. El-Bennich, Y.-X. Liu, C. D. Roberts, and P. C. Tandy, “Collective perspective on advances in Dyson-Schwinger Equation QCD,” *Commun. Theor. Phys.*, vol. 58, pp. 79–134, 2012.
- [18] A. V. Manohar, “Effective field theories,” *Lect. Notes Phys.*, vol. 479, pp. 311–362, 1997.
- [19] F. Gelis, E. Iancu, J. Jalilian-Marian, and R. Venugopalan, “The Color Glass Condensate,” *Ann. Rev. Nucl. Part. Sci.*, vol. 60, pp. 463–489, 2010.
- [20] J. M. Maldacena, “The Large N limit of superconformal field theories and supergravity,” *Int. J. Theor. Phys.*, vol. 38, pp. 1113–1133, 1999. [Adv. Theor. Math. Phys.2,231(1998)].
- [21] M. Luzum and P. Romatschke, “Conformal Relativistic Viscous Hydrodynamics: Applications to RHIC results at $s(NN)^{1/2} = 200$ GeV,” *Phys.Rev.*, vol. C78, p. 034915, 2008.
- [22] D. Teaney, “The Effects of viscosity on spectra, elliptic flow, and HBT radii,” *Phys. Rev.*, vol. C68, p. 034913, 2003.
- [23] V. Khachatryan *et al.*, “Observation of Long-Range Near-Side Angular Correlations in Proton-Proton Collisions at the LHC,” *JHEP*, vol. 09, p. 091, 2010.

- [24] G. Aad *et al.*, “Observation of Long-Range Elliptic Azimuthal Anisotropies in $\sqrt{s} = 13$ and 2.76 TeV pp Collisions with the ATLAS Detector,” *Phys. Rev. Lett.*, vol. 116, no. 17, p. 172301, 2016.
- [25] V. Khachatryan *et al.*, “Evidence for collectivity in pp collisions at the LHC,” *Phys. Lett.*, vol. B765, pp. 193–220, 2017.
- [26] P. Romatschke and U. Romatschke, “Viscosity Information from Relativistic Nuclear Collisions: How Perfect is the Fluid Observed at RHIC?,” *Phys. Rev. Lett.*, vol. 99, p. 172301, 2007.
- [27] K. Dusling and D. Teaney, “Simulating elliptic flow with viscous hydrodynamics,” *Phys. Rev.*, vol. C77, p. 034905, 2008.
- [28] P. Bozek, “Collective flow in p-Pb and d-Pd collisions at TeV energies,” *Phys. Rev.*, vol. C85, p. 014911, 2012.
- [29] I. Kozlov, M. Luzum, G. Denicol, S. Jeon, and C. Gale, “Transverse momentum structure of pair correlations as a signature of collective behavior in small collision systems,” 2014.
- [30] R. D. Weller and P. Romatschke, “One fluid to rule them all: viscous hydrodynamic description of event-by-event central p+p, p+Pb and Pb+Pb collisions at $\sqrt{s} = 5.02$ TeV,” *Phys. Lett.*, vol. B774, pp. 351–356, 2017.
- [31] J. Casalderrey-Solana, N. I. Gushterov, and B. Meiring, “Resurgence and Hydrodynamic Attractors in Gauss-Bonnet Holography,” *JHEP*, vol. 04, p. 042, 2018.
- [32] J. Casalderrey-Solana, N. I. Gushterov, and B. Meiring, “Hydrodynamization and Attractors at Intermediate Coupling,” *Nucl. Phys.*, vol. A982, pp. 907–910, 2019.
- [33] G. S. Denicol, C. Gale, and S. Jeon, “The domain of validity of fluid dynamics and the onset of cavitation in ultrarelativistic heavy ion collisions,” *PoS*, vol. CPOD2014, p. 033, 2015.
- [34] M. L. Miller, K. Reygers, S. J. Sanders, and P. Steinberg, “Glauber modeling in high energy nuclear collisions,” *Ann.Rev.Nucl.Part.Sci.*, vol. 57, pp. 205–243, 2007.
- [35] B. Alver, M. Baker, C. Loizides, and P. Steinberg, “The PHOBOS Glauber Monte Carlo,” 2008.

- [36] E. Avsar, G. Gustafson, and L. Lonnblad, “Energy conservation and saturation in small-x evolution,” *JHEP*, vol. 0507, p. 062, 2005.
- [37] D. Kharzeev and M. Nardi, “Hadron production in nuclear collisions at RHIC and high density QCD,” *Phys.Lett.*, vol. B507, pp. 121–128, 2001.
- [38] D. Kharzeev and E. Levin, “Manifestations of high density QCD in the first RHIC data,” *Phys.Lett.*, vol. B523, pp. 79–87, 2001.
- [39] B. Schenke, P. Tribedy, and R. Venugopalan, “Fluctuating Glasma initial conditions and flow in heavy ion collisions,” *Phys.Rev.Lett.*, vol. 108, p. 252301, 2012.
- [40] F. Cooper and G. Frye, “Comment on the Single Particle Distribution in the Hydrodynamic and Statistical Thermodynamic Models of Multiparticle Production,” *Phys.Rev.*, vol. D10, p. 186, 1974.
- [41] C. Gale, S. Jeon, and B. Schenke, “Hydrodynamic Modeling of Heavy-Ion Collisions,” *Int.J.Mod.Phys.*, vol. A28, p. 1340011, 2013.
- [42] U. W. Heinz, “Early collective expansion: Relativistic hydrodynamics and the transport properties of QCD matter,” 2009.
- [43] S.R. De Groot, W.A. van Leeuwen, and C.G. van Weert, *Relativistic kinetic theory: principles and applications*. North-Holland Publishing Company, 1980.
- [44] S. A. Bass *et al.*, “Microscopic models for ultrarelativistic heavy ion collisions,” *Prog. Part. Nucl. Phys.*, vol. 41, pp. 255–369, 1998. [Prog. Part. Nucl. Phys.41,225(1998)].
- [45] O. Buss, T. Gaitanos, K. Gallmeister, H. van Hees, M. Kaskulov, O. Lalakulich, A. B. Larionov, T. Leitner, J. Weil, and U. Mosel, “Transport-theoretical Description of Nuclear Reactions,” *Phys. Rept.*, vol. 512, pp. 1–124, 2012.
- [46] W. Cassing and E. L. Bratkovskaya, “Parton transport and hadronization from the dynamical quasiparticle point of view,” *Phys. Rev.*, vol. C78, p. 034919, 2008.
- [47] Z. Xu and C. Greiner, “Thermalization of gluons in ultrarelativistic heavy ion collisions by including three-body interactions in a parton cascade,” *Phys. Rev.*, vol. C71, p. 064901, 2005.
- [48] J. Weil *et al.*, “Particle production and equilibrium properties within a new hadron transport approach for heavy-ion collisions,” *Phys. Rev.*, vol. C94, no. 5, p. 054905, 2016.

- [49] E .M. Lifschitz and L. P. Pitaevskii, *Course of Theoretical Physics. Vol. 10: Physical Kinetics*. Pergamon Press, 1981.
- [50] P. Huovinen, P. Kolb, U. W. Heinz, P. Ruuskanen, and S. Voloshin, “Radial and elliptic flow at RHIC: Further predictions,” *Phys.Lett.*, vol. B503, pp. 58–64, 2001.
- [51] P. Kovtun, D. T. Son, and A. O. Starinets, “Viscosity in strongly interacting quantum field theories from black hole physics,” *Phys.Rev.Lett.*, vol. 94, p. 111601, 2005.
- [52] P. Danielewicz and M. Gyulassy, “Dissipative Phenomena in Quark Gluon Plasmas,” *Phys. Rev.*, vol. D31, pp. 53–62, 1985.
- [53] M. Luzum and J.-Y. Ollitrault, “Extracting the shear viscosity of the quark-gluon plasma from flow in ultra-central heavy-ion collisions,” *Nucl.Phys.*, vol. A904-905, pp. 377c–380c, 2013.
- [54] C. Gale, S. Jeon, B. Schenke, P. Tribedy, and R. Venugopalan, “Event-by-event anisotropic flow in heavy-ion collisions from combined Yang-Mills and viscous fluid dynamics,” *Phys.Rev.Lett.*, vol. 110, p. 012302, 2013.
- [55] G. S. Denicol, T. Kodama, and T. Koide, “The effect of shear and bulk viscosities on elliptic flow,” *J. Phys.*, vol. G37, p. 094040, 2010.
- [56] H. Niemi, G. S. Denicol, P. Huovinen, E. Molnar, and D. H. Rischke, “Influence of a temperature-dependent shear viscosity on the azimuthal asymmetries of transverse momentum spectra in ultrarelativistic heavy-ion collisions,” *Phys. Rev.*, vol. C86, p. 014909, 2012.
- [57] H. Song, S. A. Bass, and U. Heinz, “Viscous QCD matter in a hybrid hydrodynamic+Boltzmann approach,” *Phys. Rev.*, vol. C83, p. 024912, 2011.
- [58] H. Song, S. A. Bass, and U. Heinz, “Elliptic flow in 200 A GeV Au+Au collisions and 2.76 A TeV Pb+Pb collisions: insights from viscous hydrodynamics + hadron cascade hybrid model,” *Phys. Rev.*, vol. C83, p. 054912, 2011. [Erratum: *Phys. Rev.*C87,no.1,019902(2013)].
- [59] H. Niemi, K. J. Eskola, and R. Paatelainen, “Event-by-event fluctuations in a perturbative QCD + saturation + hydrodynamics model: Determining QCD matter shear viscosity in ultrarelativistic heavy-ion collisions,” *Phys. Rev.*, vol. C93, no. 2, p. 024907, 2016.
- [60] G. Denicol, A. Monnai, and B. Schenke, “Moving forward to constrain the shear viscosity of QCD matter,” *Phys. Rev. Lett.*, vol. 116, no. 21, p. 212301, 2016.

- [61] G. Denicol, A. Monnai, S. Ryu, and B. Schenke, “New insights from 3D simulations of heavy ion collisions,” *Nucl. Phys.*, vol. A956, pp. 288–291, 2016.
- [62] J. E. Bernhard, J. S. Moreland, S. A. Bass, J. Liu, and U. Heinz, “Applying Bayesian parameter estimation to relativistic heavy-ion collisions: simultaneous characterization of the initial state and quark-gluon plasma medium,” *Phys. Rev.*, vol. C94, no. 2, p. 024907, 2016.
- [63] J. Auvinen, J. E. Bernhard, S. A. Bass, and I. Karpenko, “Investigating the collision energy dependence of η/s in the beam energy scan at the BNL Relativistic Heavy Ion Collider using Bayesian statistics,” *Phys. Rev.*, vol. C97, no. 4, p. 044905, 2018.
- [64] J. E. Bernhard, *Bayesian parameter estimation for relativistic heavy-ion collisions*. PhD thesis, Duke U., 2018-04-19.
- [65] A. Adams, L. D. Carr, T. Schaefer, P. Steinberg, and J. E. Thomas, “Focus on strongly correlated quantum fluids: From ultracold quantum gases to QCD plasmas,” *New J. Phys.*, vol. 15, p. 045022, 2013.
- [66] M. Prakash, M. Prakash, R. Venugopalan, and G. Welke, “Nonequilibrium properties of hadronic mixtures,” *Phys. Rept.*, vol. 227, pp. 321–366, 1993.
- [67] D. Davesne, “Transport coefficients of a hot pion gas,” *Phys. Rev.*, vol. C53, pp. 3069–3084, 1996.
- [68] A. Dobado and F. J. Llanes-Estrada, “The Viscosity of meson matter,” *Phys. Rev.*, vol. D69, p. 116004, 2004.
- [69] S. Muroya and N. Sasaki, “A Calculation of the viscosity over entropy ratio of a hadronic gas,” *Prog. Theor. Phys.*, vol. 113, pp. 457–462, 2005.
- [70] J.-W. Chen and E. Nakano, “Shear viscosity to entropy density ratio of QCD below the deconfinement temperature,” *Phys. Lett.*, vol. B647, pp. 371–375, 2007.
- [71] K. Itakura, O. Morimatsu, and H. Otomo, “Shear viscosity of a hadronic gas mixture,” *Phys. Rev.*, vol. D77, p. 014014, 2008.
- [72] M. I. Gorenstein, M. Hauer, and O. N. Moroz, “Viscosity in the excluded volume hadron gas model,” *Phys. Rev.*, vol. C77, p. 024911, 2008. [[214\(2007\)](#)].
- [73] A. Dobado, F. J. Llanes-Estrada, and J. M. Torres-Rincon, “ η/s and phase transitions,” *Phys. Rev.*, vol. D79, p. 014002, 2009.

- [74] D. Fernandez-Fraile and A. Gomez Nicola, “Transport coefficients and resonances for a meson gas in Chiral Perturbation Theory,” *Eur. Phys. J.*, vol. C62, pp. 37–54, 2009.
- [75] J. M. Torres-Rincon, *Hadronic Transport Coefficients from Effective Field Theories*. PhD thesis, UCM, Somosaguas, New York, 2012.
- [76] O. N. Moroz, “Analytical formulas, general properties and calculation of transport coefficients in the hadron gas: shear and bulk viscosities,” 2013.
- [77] A. Muronga, “Shear viscosity coefficient from microscopic models,” *Phys. Rev.*, vol. C69, p. 044901, 2004.
- [78] N. Demir and S. A. Bass, “Shear-Viscosity to Entropy-Density Ratio of a Relativistic Hadron Gas,” *Phys. Rev. Lett.*, vol. 102, p. 172302, 2009.
- [79] C. Wesp, A. El, F. Reining, Z. Xu, I. Bouras, and C. Greiner, “Calculation of shear viscosity using Green-Kubo relations within a parton cascade,” *Phys. Rev.*, vol. C84, p. 054911, 2011.
- [80] S. Plumari, A. Puglisi, F. Scardina, and V. Greco, “Shear Viscosity of a strongly interacting system: Green-Kubo vs. Chapman-Enskog and Relaxation Time Approximation,” *Phys. Rev.*, vol. C86, p. 054902, 2012.
- [81] V. Ozvenchuk, O. Linnyk, M. I. Gorenstein, E. L. Bratkovskaya, and W. Cassing, “Shear and bulk viscosities of strongly interacting “infinite” parton-hadron matter within the parton-hadron-string dynamics transport approach,” *Phys. Rev.*, vol. C87, no. 6, p. 064903, 2013.
- [82] S. Pratt, A. Baez, and J. Kim, “Determining Transport Coefficients for a Microscopic Simulation of a Hadron Gas,” *Phys. Rev.*, vol. C95, no. 2, p. 024901, 2017.
- [83] M. Greif, I. Bouras, Z. Xu, and C. Greiner, “Electric conductivity of the quark-gluon plasma investigated using Boltzmann transport theory,” *J. Phys. Conf. Ser.*, vol. 612, no. 1, p. 012056, 2015.
- [84] H. B. Meyer, “A Calculation of the shear viscosity in SU(3) gluodynamics,” *Phys. Rev.*, vol. D76, p. 101701, 2007.
- [85] H. B. Meyer, “Transport properties of the quark-gluon plasma from lattice QCD,” *Nucl. Phys.*, vol. A830, pp. 641C–648C, 2009.
- [86] S. W. Mages, S. Borsányi, Z. Fodor, A. Schäfer, and K. Szabó, “Shear Viscosity from Lattice QCD,” *PoS*, vol. LATTICE2014, p. 232, 2015.

- [87] N. Astrakhantsev, V. Braguta, and A. Kotov, “Temperature dependence of shear viscosity of $SU(3)$ -gluodynamics within lattice simulation,” *JHEP*, vol. 04, p. 101, 2017.
- [88] R. Rougemont, R. Critelli, J. Noronha-Hostler, J. Noronha, and C. Ratti, “Dynamical versus equilibrium properties of the QCD phase transition: A holographic perspective,” *Phys. Rev.*, vol. D96, no. 1, p. 014032, 2017.
- [89] L. P. Csernai, J. Kapusta, and L. D. McLerran, “On the Strongly-Interacting Low-Viscosity Matter Created in Relativistic Nuclear Collisions,” *Phys. Rev. Lett.*, vol. 97, p. 152303, 2006.
- [90] J.-W. Chen, M. Huang, Y.-H. Li, E. Nakano, and D.-L. Yang, “Phase Transitions and the Perfectness of Fluids,” *Phys. Lett.*, vol. B670, pp. 18–21, 2008.
- [91] C. Sasaki and K. Redlich, “Transport coefficients near chiral phase transition,” *Nucl. Phys.*, vol. A832, pp. 62–75, 2010.
- [92] A. Dobado, F. J. Llanes-Estrada, and J. M. Torres-Rincon, “Minimum of η/s and the phase transition of the Linear Sigma Model in the large- N limit,” *Phys. Rev.*, vol. D80, p. 114015, 2009.
- [93] M. Bluhm, B. Kampfer, and K. Redlich, “Bulk and shear viscosities of the gluon plasma in a quasiparticle description,” *Phys. Rev.*, vol. C84, p. 025201, 2011.
- [94] P. Romatschke and S. Pratt, “Extracting the shear viscosity of a high temperature hadron gas,” 2014.
- [95] F. Karsch, D. Kharzeev, and K. Tuchin, “Universal properties of bulk viscosity near the QCD phase transition,” *Phys. Lett.*, vol. B663, pp. 217–221, 2008.
- [96] S. Aoki, S. Ejiri, T. Hatsuda, N. Ishii, K. Kanaya, Y. Maezawa, N. Ukita, and T. Umeda, “Equation of state at finite density in two-flavor QCD with improved Wilson quarks,” *PoS*, vol. LATTICE2008, p. 189, 2008.
- [97] G. Denicol, T. Kodama, T. Koide, and P. Mota, “Bulk viscosity effects on elliptic flow,” *Nucl.Phys.*, vol. A830, pp. 729C–732C, 2009.
- [98] G. S. Denicol, T. Kodama, T. Koide, and P. Mota, “Effect of bulk viscosity on Elliptic Flow near QCD phase transition,” *Phys. Rev.*, vol. C80, p. 064901, 2009.
- [99] A. Monnai and T. Hirano, “Effects of Bulk Viscosity at Freezeout,” *Phys.Rev.*, vol. C80, p. 054906, 2009.

- [100] G. S. Denicol, S. Jeon, and C. Gale, “Transport Coefficients of Bulk Viscous Pressure in the 14-moment approximation,” *Phys. Rev.*, vol. C90, no. 2, p. 024912, 2014.
- [101] S. Ryu, J. F. Paquet, C. Shen, G. S. Denicol, B. Schenke, S. Jeon, and C. Gale, “Importance of the Bulk Viscosity of QCD in Ultrarelativistic Heavy-Ion Collisions,” *Phys. Rev. Lett.*, vol. 115, no. 13, p. 132301, 2015.
- [102] S. Ryu, J.-F. Paquet, C. Shen, G. Denicol, B. Schenke, S. Jeon, and C. Gale, “Effects of bulk viscosity and hadronic rescattering in heavy ion collisions at energies available at the BNL Relativistic Heavy Ion Collider and at the CERN Large Hadron Collider,” *Phys. Rev.*, vol. C97, no. 3, p. 034910, 2018.
- [103] J. Noronha-Hostler, J. Noronha, and C. Greiner, “Transport Coefficients of Hadronic Matter near $T(c)$,” *Phys. Rev. Lett.*, vol. 103, p. 172302, 2009.
- [104] D. Fernandez-Fraile and A. Gomez Nicola, “Bulk viscosity and the conformal anomaly in the pion gas,” *Phys. Rev. Lett.*, vol. 102, p. 121601, 2009.
- [105] E. Lu and G. D. Moore, “The Bulk Viscosity of a Pion Gas,” *Phys. Rev.*, vol. C83, p. 044901, 2011.
- [106] A. Dobado, F. J. Llanes-Estrada, and J. M. Torres-Rincon, “Bulk viscosity of low-temperature strongly interacting matter,” *Phys. Lett.*, vol. B702, pp. 43–48, 2011.
- [107] H.-T. Ding, O. Kaczmarek, and F. Meyer, “Thermal dilepton rates and electrical conductivity of the QGP from the lattice,” *Phys. Rev.*, vol. D94, no. 3, p. 034504, 2016.
- [108] J. Ghiglieri, O. Kaczmarek, M. Laine, and F. Meyer, “Lattice constraints on the thermal photon rate,” *Phys. Rev.*, vol. D94, no. 1, p. 016005, 2016.
- [109] G. Baym and H. Heiselberg, “The Electrical conductivity in the early universe,” *Phys. Rev.*, vol. D56, pp. 5254–5259, 1997.
- [110] K. Tuchin, “Particle production in strong electromagnetic fields in relativistic heavy-ion collisions,” *Adv. High Energy Phys.*, vol. 2013, p. 490495, 2013.
- [111] D. Fernandez-Fraile and A. Gomez Nicola, “The Electrical conductivity of a pion gas,” *Phys. Rev.*, vol. D73, p. 045025, 2006.
- [112] V. Roy, S. Pu, L. Rezzolla, and D. H. Rischke, “Effect of intense magnetic fields on reduced-MHD evolution in $\sqrt{s_{NN}} = 200$ GeV Au+Au collisions,” *Phys. Rev.*, vol. C96, no. 5, p. 054909, 2017.

- [113] G. Inghirami, L. Del Zanna, A. Beraudo, M. H. Moghaddam, F. Becattini, and M. Bleicher, “Numerical magneto-hydrodynamics for relativistic nuclear collisions,” *Eur. Phys. J.*, vol. C76, no. 12, p. 659, 2016.
- [114] V. Roy, S. Pu, L. Rezzolla, and D. Rischke, “Analytic Bjorken flow in one-dimensional relativistic magnetohydrodynamics,” *Phys. Lett.*, vol. B750, pp. 45–52, 2015.
- [115] M. Greif, C. Greiner, and G. S. Denicol, “Electric conductivity of a hot hadron gas from a kinetic approach,” *Phys. Rev.*, vol. D93, no. 9, p. 096012, 2016. [Erratum: *Phys. Rev.*D96,no.5,059902(2017)].
- [116] M. Greif, I. Bouras, C. Greiner, and Z. Xu, “Electric conductivity of the quark-gluon plasma investigated using a perturbative QCD based parton cascade,” *Phys. Rev.*, vol. D90, no. 9, p. 094014, 2014.
- [117] A. Puglisi, S. Plumari, and V. Greco, “Electric Conductivity from the solution of the Relativistic Boltzmann Equation,” *Phys. Rev.*, vol. D90, p. 114009, 2014.
- [118] W. Cassing, O. Linnyk, T. Steinert, and V. Ozvenchuk, “Electrical Conductivity of Hot QCD Matter,” *Phys. Rev. Lett.*, vol. 110, no. 18, p. 182301, 2013.
- [119] T. Steinert and W. Cassing, “Electric and magnetic response of hot QCD matter,” *Phys. Rev.*, vol. C89, no. 3, p. 035203, 2014.
- [120] R. Marty, E. Bratkovskaya, W. Cassing, J. Aichelin, and H. Berrehrhah, “Transport coefficients from the Nambu-Jona-Lasinio model for $SU(3)_f$,” *Phys. Rev.*, vol. C88, p. 045204, 2013.
- [121] H. Berrehrhah, W. Cassing, E. Bratkovskaya, and T. Steinert, “Quark susceptibility in a generalized dynamical quasiparticle model,” *Phys. Rev.*, vol. C93, no. 4, p. 044914, 2016.
- [122] S. I. Finazzo and J. Noronha, “Holographic calculation of the electric conductivity of the strongly coupled quark-gluon plasma near the deconfinement transition,” *Phys. Rev.*, vol. D89, no. 10, p. 106008, 2014.
- [123] S. I. Finazzo, R. Rougemont, H. Marrochio, and J. Noronha, “Hydrodynamic transport coefficients for the non-conformal quark-gluon plasma from holography,” *JHEP*, vol. 02, p. 051, 2015.
- [124] A. Amato, G. Aarts, C. Allton, P. Giudice, S. Hands, and J.-I. Skullerud, “Electrical conductivity of the quark-gluon plasma across the deconfinement transition,” *Phys. Rev. Lett.*, vol. 111, no. 17, p. 172001, 2013.

- [125] G. Aarts, C. Allton, A. Amato, P. Giudice, S. Hands, and J.-I. Skullerud, “Electrical conductivity and charge diffusion in thermal QCD from the lattice,” *JHEP*, vol. 02, p. 186, 2015.
- [126] B. B. Brandt, A. Francis, B. Jäger, and H. B. Meyer, “Charge transport and vector meson dissociation across the thermal phase transition in lattice QCD with two light quark flavors,” *Phys. Rev.*, vol. D93, no. 5, p. 054510, 2016.
- [127] S.-x. Qin, “A divergence-free method to extract observables from correlation functions,” *Phys. Lett.*, vol. B742, pp. 358–362, 2015.
- [128] P. B. Arnold, G. D. Moore, and L. G. Yaffe, “Transport coefficients in high temperature gauge theories. 1. Leading log results,” *JHEP*, vol. 11, p. 001, 2000.
- [129] P. B. Arnold, G. D. Moore, and L. G. Yaffe, “Transport coefficients in high temperature gauge theories. 2. Beyond leading log,” *JHEP*, vol. 05, p. 051, 2003.
- [130] S. Mitra and V. Chandra, “Thermal relaxation, electrical conductivity, and charge diffusion in a hot QCD medium,” *Phys. Rev.*, vol. D94, no. 3, p. 034025, 2016.
- [131] K. Hattori and D. Satow, “Electrical Conductivity of Quark-Gluon Plasma in Strong Magnetic Fields,” *Phys. Rev.*, vol. D94, no. 11, p. 114032, 2016.
- [132] K. Fukushima and Y. Hidaka, “Electric conductivity of hot and dense quark matter in a magnetic field with Landau level resummation via kinetic equations,” *Phys. Rev. Lett.*, vol. 120, no. 16, p. 162301, 2018.
- [133] S. Ghosh, S. Mitra, and S. Sarkar, “Medium effects on the electrical conductivity of a hot pion gas,” *Nucl. Phys.*, vol. A969, pp. 237–253, 2018.
- [134] S. Ghosh, “Electrical conductivity of hadronic matter from different possible mesonic and baryonic loops,” *Phys. Rev.*, vol. D95, no. 3, p. 036018, 2017.
- [135] V. Koch, A. Majumder, and J. Randrup, “Baryon-strangeness correlations: A Diagnostic of strongly interacting matter,” *Phys. Rev. Lett.*, vol. 95, p. 182301, 2005.
- [136] S. Haussler, S. Scherer, and M. Bleicher, “The Effect of Dynamical Parton Recombination on Event-by-Event Observables,” *Phys. Lett.*, vol. B660, pp. 197–201, 2008.
- [137] Y. Mehtar-Tani, J. G. Milhano, and K. Tywoniuk, “Jet physics in heavy-ion collisions,” *Int. J. Mod. Phys.*, vol. A28, p. 1340013, 2013.

- [138] G.-Y. Qin and X.-N. Wang, “Jet quenching in high-energy heavy-ion collisions,” *Int. J. Mod. Phys.*, vol. E24, no. 11, p. 1530014, 2015. [,309(2016)].
- [139] R. Baier, Y. L. Dokshitzer, A. H. Mueller, S. Peigne, and D. Schiff, “Radiative energy loss of high-energy quarks and gluons in a finite volume quark - gluon plasma,” *Nucl. Phys.*, vol. B483, pp. 291–320, 1997.
- [140] B. G. Zakharov, “Fully quantum treatment of the Landau-Pomeranchuk-Migdal effect in QED and QCD,” *JETP Lett.*, vol. 63, pp. 952–957, 1996.
- [141] R. Baier, Y. L. Dokshitzer, A. H. Mueller, and D. Schiff, “Medium induced radiative energy loss: Equivalence between the BDMPS and Zakharov formalisms,” *Nucl. Phys.*, vol. B531, pp. 403–425, 1998.
- [142] M. Gyulassy, P. Levai, and I. Vitev, “Reaction operator approach to nonAbelian energy loss,” *Nucl. Phys.*, vol. B594, pp. 371–419, 2001.
- [143] U. A. Wiedemann, “Gluon radiation off hard quarks in a nuclear environment: Opacity expansion,” *Nucl. Phys.*, vol. B588, pp. 303–344, 2000.
- [144] X.-N. Wang and X.-f. Guo, “Multiple parton scattering in nuclei: Parton energy loss,” *Nucl. Phys.*, vol. A696, pp. 788–832, 2001.
- [145] P. B. Arnold, G. D. Moore, and L. G. Yaffe, “Photon and gluon emission in relativistic plasmas,” *JHEP*, vol. 06, p. 030, 2002.
- [146] C. A. Salgado and U. A. Wiedemann, “Calculating quenching weights,” *Phys. Rev.*, vol. D68, p. 014008, 2003.
- [147] S. Jeon and G. D. Moore, “Energy loss of leading partons in a thermal QCD medium,” *Phys. Rev.*, vol. C71, p. 034901, 2005.
- [148] P. Jacobs and X.-N. Wang, “Matter in extremis: Ultrarelativistic nuclear collisions at RHIC,” *Prog. Part. Nucl. Phys.*, vol. 54, pp. 443–534, 2005.
- [149] I. P. Lokhtin and A. M. Snigirev, “A Model of jet quenching in ultrarelativistic heavy ion collisions and high-p(T) hadron spectra at RHIC,” *Eur. Phys. J.*, vol. C45, pp. 211–217, 2006.
- [150] J. Casalderrey-Solana and C. A. Salgado, “Introductory lectures on jet quenching in heavy ion collisions,” *Acta Phys. Polon.*, vol. B38, pp. 3731–3794, 2007.
- [151] K. Zapp, J. Stachel, and U. A. Wiedemann, “A Local Monte Carlo implementation of the non-abelian Landau-Pomerantschuk-Migdal effect,” *Phys. Rev. Lett.*, vol. 103, p. 152302, 2009.

- [152] K. Zapp, G. Ingelman, J. Rathsman, J. Stachel, and U. A. Wiedemann, “A Monte Carlo Model for ‘Jet Quenching’,” *Eur. Phys. J.*, vol. C60, pp. 617–632, 2009.
- [153] N. Armesto, L. Cunqueiro, and C. A. Salgado, “Q-PYTHIA: A Medium-modified implementation of final state radiation,” *Eur. Phys. J.*, vol. C63, pp. 679–690, 2009.
- [154] B. Schenke, C. Gale, and S. Jeon, “MARTINI: An Event generator for relativistic heavy-ion collisions,” *Phys. Rev.*, vol. C80, p. 054913, 2009.
- [155] A. Majumder and M. Van Leeuwen, “The Theory and Phenomenology of Perturbative QCD Based Jet Quenching,” *Prog. Part. Nucl. Phys.*, vol. 66, pp. 41–92, 2011.
- [156] J. Casalderrey-Solana, J. G. Milhano, and U. A. Wiedemann, “Jet Quenching via Jet Collimation,” *J. Phys.*, vol. G38, p. 035006, 2011.
- [157] F. D’Eramo, M. Lekaveckas, H. Liu, and K. Rajagopal, “Momentum Broadening in Weakly Coupled Quark-Gluon Plasma (with a view to finding the quasiparticles within liquid quark-gluon plasma),” *JHEP*, vol. 05, p. 031, 2013.
- [158] X.-N. Wang and Y. Zhu, “Medium Modification of γ -jets in High-energy Heavy-ion Collisions,” *Phys. Rev. Lett.*, vol. 111, no. 6, p. 062301, 2013.
- [159] K. C. Zapp, “JEWEL 2.0.0: directions for use,” *Eur. Phys. J.*, vol. C74, no. 2, p. 2762, 2014.
- [160] J. Ghiglieri and D. Teaney, “Parton energy loss and momentum broadening at NLO in high temperature QCD plasmas,” *Int. J. Mod. Phys.*, vol. E24, no. 11, p. 1530013, 2015. [271(2016)].
- [161] Y. He, T. Luo, X.-N. Wang, and Y. Zhu, “Linear Boltzmann Transport for Jet Propagation in the Quark-Gluon Plasma: Elastic Processes and Medium Recoil,” *Phys. Rev.*, vol. C91, p. 054908, 2015. [Erratum: *Phys. Rev.*C97,no.1,019902(2018)].
- [162] J.-P. Blaizot and Y. Mehtar-Tani, “Jet Structure in Heavy Ion Collisions,” *Int. J. Mod. Phys.*, vol. E24, no. 11, p. 1530012, 2015.
- [163] Y.-T. Chien and I. Vitev, “Towards the understanding of jet shapes and cross sections in heavy ion collisions using soft-collinear effective theory,” *JHEP*, vol. 05, p. 023, 2016.

- [164] S. Cao *et al.*, “Multistage Monte-Carlo simulation of jet modification in a static medium,” *Phys. Rev.*, vol. C96, no. 2, p. 024909, 2017.
- [165] F. Arleo, “Quenching of Hadron Spectra in Heavy Ion Collisions at the LHC,” *Phys. Rev. Lett.*, vol. 119, no. 6, p. 062302, 2017.
- [166] F. D’Eramo, K. Rajagopal, and Y. Yin, “Molière scattering in quark-gluon plasma: finding point-like scatterers in a liquid,” *JHEP*, vol. 01, p. 172, 2019.
- [167] P. Caucal, E. Iancu, and G. Soyez, “Deciphering the z_g distribution in ultrarelativistic heavy ion collisions,” 2019.
- [168] J. Casalderrey-Solana, H. Liu, D. Mateos, K. Rajagopal, and U. A. Wiedemann, “Gauge/String Duality, Hot QCD and Heavy Ion Collisions,” 2011.
- [169] A. Ficnar, S. S. Gubser, and M. Gyulassy, “Shooting String Holography of Jet Quenching at RHIC and LHC,” *Phys. Lett.*, vol. B738, pp. 464–471, 2014.
- [170] P. M. Chesler and K. Rajagopal, “Jet quenching in strongly coupled plasma,” *Phys. Rev.*, vol. D90, no. 2, p. 025033, 2014.
- [171] P. M. Chesler and K. Rajagopal, “On the Evolution of Jet Energy and Opening Angle in Strongly Coupled Plasma,” *JHEP*, vol. 05, p. 098, 2016.
- [172] R. Morad and W. A. Horowitz, “Strong-coupling Jet Energy Loss from AdS/CFT,” *JHEP*, vol. 11, p. 017, 2014.
- [173] W. A. Horowitz, “Fluctuating heavy quark energy loss in a strongly coupled quark-gluon plasma,” *Phys. Rev.*, vol. D91, no. 8, p. 085019, 2015.
- [174] P. Arnold and D. Vaman, “Jet quenching in hot strongly coupled gauge theories simplified,” *JHEP*, vol. 04, p. 027, 2011.
- [175] J. Casalderrey-Solana, D. C. Gulhan, J. G. Milhano, D. Pablos, and K. Rajagopal, “A Hybrid Strong/Weak Coupling Approach to Jet Quenching,” *JHEP*, vol. 10, p. 019, 2014. [Erratum: JHEP09,175(2015)].
- [176] J. Casalderrey-Solana, D. C. Gulhan, J. G. Milhano, D. Pablos, and K. Rajagopal, “Predictions for Boson-Jet Observables and Fragmentation Function Ratios from a Hybrid Strong/Weak Coupling Model for Jet Quenching,” *JHEP*, vol. 03, p. 053, 2016.
- [177] J. Casalderrey-Solana, D. Gulhan, G. Milhano, D. Pablos, and K. Rajagopal, “Angular Structure of Jet Quenching Within a Hybrid Strong/Weak Coupling Model,” *JHEP*, vol. 03, p. 135, 2017.

- [178] J. Casalderrey-Solana, Z. Hulcher, G. Milhano, D. Pablos, and K. Rajagopal, “Simultaneous description of hadron and jet suppression in heavy-ion collisions,” *Phys. Rev.*, vol. C99, no. 5, p. 051901, 2019.
- [179] J. Casalderrey-Solana, G. Milhano, D. Pablos, and K. Rajagopal, “Modification of Jet Substructure in Heavy Ion Collisions as a Probe of the Resolution Length of Quark-Gluon Plasma,” 2019.
- [180] D. Pablos, “Jet suppression from small to intermediate to large radius,” 2019.
- [181] K. Rajagopal, A. V. Sadofyev, and W. van der Schee, “Evolution of the jet opening angle distribution in holographic plasma,” *Phys. Rev. Lett.*, vol. 116, no. 21, p. 211603, 2016.
- [182] J. Brewer, K. Rajagopal, A. Sadofyev, and W. Van Der Schee, “Evolution of the Mean Jet Shape and Dijet Asymmetry Distribution of an Ensemble of Holographic Jets in Strongly Coupled Plasma,” *JHEP*, vol. 02, p. 015, 2018.
- [183] W. Cassing, K. Gallmeister, and C. Greiner, “Suppression of high transverse momentum hadrons at RHIC by prehadronic final state interactions,” *Nucl. Phys.*, vol. A735, pp. 277–299, 2004.
- [184] C. Bierlich, G. Gustafson, L. Lönnblad, and H. Shah, “The Angantyr model for Heavy-Ion Collisions in PYTHIA8,” *JHEP*, vol. 10, p. 134, 2018.
- [185] K. Werner, I. Karpenko, M. Bleicher, T. Pierog, and S. Porteboeuf-Houssais, “Jets, Bulk Matter, and their Interaction in Heavy Ion Collisions at Several TeV,” *Phys. Rev.*, vol. C85, p. 064907, 2012.
- [186] K. Werner, “Lambda-to-Kaon Ratio Enhancement in Heavy Ion Collisions at Several TeV,” *Phys. Rev. Lett.*, vol. 109, p. 102301, 2012.
- [187] K. M. Burke *et al.*, “Extracting the jet transport coefficient from jet quenching in high-energy heavy-ion collisions,” *Phys. Rev.*, vol. C90, no. 1, p. 014909, 2014.
- [188] A. Majumder, B. Muller, and X.-N. Wang, “Small shear viscosity of a quark-gluon plasma implies strong jet quenching,” *Phys. Rev. Lett.*, vol. 99, p. 192301, 2007.
- [189] S. Chatrchyan *et al.*, “Modification of jet shapes in PbPb collisions at $\sqrt{s_{NN}} = 2.76$ TeV,” *Phys. Lett.*, vol. B730, pp. 243–263, 2014.
- [190] G. Aad *et al.*, “Measurement of angular and momentum distributions of charged particles within and around jets in Pb+Pb and *pp* collisions at $\sqrt{s_{NN}} = 5.02$ TeV with the ATLAS detector,” 2019.

- [191] S. Acharya *et al.*, “Measurement of jet radial profiles in Pb–Pb collisions at $\sqrt{s_{\text{NN}}} = 2.76$ TeV,” *Phys. Lett.*, vol. B796, pp. 204–219, 2019.
- [192] P. Langevin, “Sur la théorie du mouvement brownien,” *C. R. Acad. Sci. Paris.*, vol. 146, p. 530–533, 1908.
- [193] A. Einstein, “Über die von der molekularkinetischen Theorie der Wärme geforderte Bewegung von in ruhenden Flüssigkeiten suspendierten Teilchen,” *Annalen der Physik, (ser. 4)*, vol. 17, p. 549–560, 1905.
- [194] D. N. Zubarev, *Nonequilibrium statistical thermodynamics*. Consultants Bureau, New-York-London, 1974.
- [195] A. Hosoya, M.-a. Sakagami, and M. Takao, “Nonequilibrium Thermodynamics in Field Theory: Transport Coefficients,” *Annals Phys.*, vol. 154, p. 229, 1984.
- [196] J. Tindall, J. M. Torres-Rincon, J. B. Rose, and H. Petersen, “Equilibration and freeze-out of an expanding gas in a transport approach in a Friedmann–Robertson–Walker metric,” *Phys. Lett.*, vol. B770, pp. 532–538, 2017.
- [197] J. B. Rose, J. M. Torres-Rincon, A. Schäfer, D. R. Oliinychenko, and H. Petersen, “Shear viscosity of a hadron gas and influence of resonance lifetimes on relaxation time,” *Phys. Rev.*, vol. C97, no. 5, p. 055204, 2018.
- [198] J. Staudenmaier, J. Weil, V. Steinberg, S. Endres, and H. Petersen, “Dilepton production and resonance properties within a new hadronic transport approach in the context of the GSI-HADES experimental data,” *Phys. Rev.*, vol. C98, no. 5, p. 054908, 2018.
- [199] D. Oliinychenko, L.-G. Pang, H. Elfner, and V. Koch, “Microscopic study of deuteron production in PbPb collisions at $\sqrt{s} = 2.76\text{TeV}$ via hydrodynamics and a hadronic afterburner,” *Phys. Rev.*, vol. C99, no. 4, p. 044907, 2019.
- [200] V. Steinberg, J. Staudenmaier, D. Oliinychenko, F. Li, Ö. Erkiner, and H. Elfner, “Strangeness production via resonances in heavy-ion collisions at energies available at the GSI Schwerionensynchrotron,” *Phys. Rev.*, vol. C99, no. 6, p. 064908, 2019.
- [201] A. Schäfer, J. M. Torres-Rincon, J. Rothermel, N. Ehlert, C. Gale, and H. Elfner, “Benchmarking a nonequilibrium approach to photon emission in relativistic heavy-ion collisions,” *Phys. Rev.*, vol. D99, no. 11, p. 114021, 2019.
- [202] J. Hammelmann, A. Soto-Ontoso, M. Alvioli, H. Elfner, and M. Strikmann, “Influence of the neutron-skin effect on nuclear isobar collisions at RHIC,” 2019.

- [203] J. Mohs, S. Ryu, and H. Elfner, “Particle Production via Strings and Baryon Stopping within a Hadronic Transport Approach,” 2019.
- [204] S. D. Team, “Simulating Many Accelerated Strongly-interacting Hadrons,” 2018.
- [205] T. Kodama, S. B. Duarte, K. C. Chung, R. Donangelo, and R. A. M. S. Nazareth, “Causality and relativistic effects in intranuclear cascade calculations,” *Phys. Rev.*, vol. C29, pp. 2146–2152, 1984.
- [206] P. Danielewicz and G. F. Bertsch, “Production of deuterons and pions in a transport model of energetic heavy ion reactions,” *Nucl. Phys.*, vol. A533, pp. 712–748, 1991.
- [207] W. Cassing, “Anti-baryon production in hot and dense nuclear matter,” *Nucl. Phys.*, vol. A700, pp. 618–646, 2002.
- [208] A. Lang, W. Cassing, U. Mosel, and K. Weber, “Covariant calculation of K⁺ production in nucleus-nucleus collisions at SIS energies,” *Nucl. Phys.*, vol. A541, pp. 507–524, 1992.
- [209] J. H. Putschke *et al.*, “The JETSCAPE framework,” 2019.
- [210] S. Ryu, J. Staudenmaier, and H. Elfner, “Bulk Observables within a Hybrid Approach for Heavy Ion Collisions with SMASH Afterburner,” *MDPI Proc.*, vol. 10, no. 1, p. 44, 2019.
- [211] D. Bazow, G. S. Denicol, U. Heinz, M. Martinez, and J. Noronha, “Analytic solution of the Boltzmann equation in an expanding system,” *Phys. Rev. Lett.*, vol. 116, no. 2, p. 022301, 2016.
- [212] D. Bazow, G. S. Denicol, U. Heinz, M. Martinez, and J. Noronha, “Nonlinear dynamics from the relativistic Boltzmann equation in the Friedmann-Lemaître-Robertson-Walker spacetime,” *Phys. Rev.*, vol. D94, no. 12, p. 125006, 2016.
- [213] M. Tanabashi *et al.*, “Review of Particle Physics,” *Phys. Rev.*, vol. D98, no. 3, p. 030001, 2018.
- [214] D. M. Manley and E. M. Saleski, “Multichannel resonance parametrization of pi N scattering amplitudes,” *Phys. Rev.*, vol. D45, pp. 4002–4033, 1992.
- [215] J. M. Blatt and V. F. Weisskopf, *Theoretical Nuclear Physics*. Wiley, 1958.
- [216] S. U. Chung, “Formulas for Angular-Momentum Barrier Factors - Version II,” 2015.

- [217] J. Weil, *Vector Mesons in Medium in a Transport Approach*. PhD thesis, Giessen U., 2013.
- [218] Y. Oh, Z.-W. Lin, and C. M. Ko, “Deuteron production and elliptic flow in relativistic heavy ion collisions,” *Phys. Rev.*, vol. C80, p. 064902, 2009.
- [219] V. Dmitriev, O. Sushkov, and C. Gaarde, “ Δ Formation in the ^1H (^3He , ^3H) Δ^{++} Reaction at Intermediate-energies,” *Nucl. Phys.*, vol. A459, pp. 503–524, 1986.
- [220] S. Teis, W. Cassing, M. Effenberger, A. Hombach, U. Mosel, and G. Wolf, “Pion production in heavy ion collisions at SIS energies,” *Z. Phys.*, vol. A356, pp. 421–435, 1997.
- [221] G. Graef, J. Steinheimer, F. Li, and M. Bleicher, “Deep sub-threshold Ξ and Λ production in nuclear collisions with the UrQMD transport model,” *Phys. Rev.*, vol. C90, p. 064909, 2014.
- [222] V. Flaminio, W. G. Moorhead, D. R. O. Morrison, and N. Rivoire, “COMPI- LATION OF CROSS-SECTIONS. 2. K+ AND K- INDUCED REACTIONS,” 1983.
- [223] W. Ehehalt and W. Cassing, “Relativistic transport approach for nucleus nucleus collisions from SIS to SPS energies,” *Nucl. Phys.*, vol. A602, pp. 449–486, 1996.
- [224] Y. Nara, N. Otuka, A. Ohnishi, K. Niita, and S. Chiba, “Study of relativistic nuclear collisions at AGS energies from p + Be to Au + Au with hadronic cascade model,” *Phys. Rev.*, vol. C61, p. 024901, 2000.
- [225] W. Cassing and E. L. Bratkovskaya, “Parton-Hadron-String Dynamics: an off-shell transport approach for relativistic energies,” *Nucl. Phys.*, vol. A831, pp. 215–242, 2009.
- [226] J. Novak, K. Novak, S. Pratt, J. Vredevoogd, C. Coleman-Smith, and R. Wolpert, “Determining Fundamental Properties of Matter Created in Ultrarelativistic Heavy-Ion Collisions,” *Phys. Rev.*, vol. C89, no. 3, p. 034917, 2014.
- [227] N. S. Demir, *Extraction of Hot QCD Matter Transport Coefficients Utilizing Microscopic Transport Theory*. PhD thesis, Duke University, 2010.
- [228] J. Cugnon, J. Vandermeulen, and D. L’Hote, “Simple parametrization of cross-sections for nuclear transport studies up to the GeV range,” *Nucl. Instrum. Meth.*, vol. B111, pp. 215–220, 1996.

- [229] B. Andersson, G. Gustafson, G. Ingelman, and T. Sjostrand, “Parton Fragmentation and String Dynamics,” *Phys. Rept.*, vol. 97, pp. 31–145, 1983.
- [230] T. Sjöstrand, S. Ask, J. R. Christiansen, R. Corke, N. Desai, P. Ilten, S. Mrenna, S. Prestel, C. O. Rasmussen, and P. Z. Skands, “An Introduction to PYTHIA 8.2,” *Comput. Phys. Commun.*, vol. 191, pp. 159–177, 2015.
- [231] R. Corke and T. Sjostrand, “Multiparton Interactions and Rescattering,” *JHEP*, vol. 01, p. 035, 2010.
- [232] M. Bleicher *et al.*, “Relativistic hadron hadron collisions in the ultrarelativistic quantum molecular dynamics model,” *J. Phys.*, vol. G25, pp. 1859–1896, 1999.
- [233] G. A. Schuler and T. Sjostrand, “Hadronic diffractive cross-sections and the rise of the total cross-section,” *Phys. Rev.*, vol. D49, pp. 2257–2267, 1994.
- [234] K. A. Goulianos, “Diffractive Interactions of Hadrons at High-Energies,” *Phys. Rept.*, vol. 101, p. 169, 1983.
- [235] D. Oliinychenko, V. Steinberg, J. Weil, M. Kretz, H. E. (Petersen), J. Staudenmaier, S. Ryu, A. Schäfer, J. Rothermel, J. Mohs, F. Li, L. Pang, D. Mitrovic, A. Goldschmidt, L. Geiger, L. Prinz, J.-B. Rose, and J. Hammelmann, “smash-transport/smash: Smash-1.6,” May 2019.
- [236] K. A. Olive *et al.*, “Review of Particle Physics,” *Chin. Phys.*, vol. C38, p. 090001, 2014.
- [237] G. S. Denicol, C. Gale, S. Jeon, and J. Noronha, “Fluid behavior of a baryon-rich hadron resonance gas,” *Phys. Rev.*, vol. C88, no. 6, p. 064901, 2013.
- [238] S. Cheng, S. Pratt, P. Csizmadia, Y. Nara, D. Molnar, M. Gyulassy, S. E. Vance, and B. Zhang, “The Effect of finite range interactions in classical transport theory,” *Phys. Rev.*, vol. C65, p. 024901, 2002.
- [239] J. C. Maxwell, “On the viscosity or internal friction of air and other gases,” *Phil. Trans. R. Soc. Lond.*, vol. 156, pp. 249–268, 1866.
- [240] A. Wiranata, V. Koch, M. Prakash, and X. N. Wang, “Shear viscosity of hadrons with K-matrix cross sections,” *Phys. Rev.*, vol. C88, no. 4, p. 044917, 2013.
- [241] D. J. Evans and G. P. Morriss, *Statistical Mechanics of Nonequilibrium Liquids*. Academic, London, 1990.
- [242] J. B. Rose, J. M. Torres-Rincon, D. Oliinychenko, A. Schäfer, and H. Petersen, “Systematic errors in transport calculations of shear viscosity using the Green-Kubo formalism,” *J. Phys. Conf. Ser.*, vol. 1024, no. 1, p. 012028, 2018.

- [243] J. Gasser and H. Leutwyler, “Chiral Perturbation Theory to One Loop,” *Annals Phys.*, vol. 158, p. 142, 1984.
- [244] S. Scherer, “Introduction to chiral perturbation theory,” *Adv. Nucl. Phys.*, vol. 27, p. 277, 2003. [,277(2002)].
- [245] R. Horsley and W. Schoenmaker, “Quantum Field Theories Out of Thermal Equilibrium. 1. General Considerations,” *Nucl. Phys.*, vol. B280, pp. 716–734, 1987.
- [246] A. Czajka, K. Dasgupta, C. Gale, S. Jeon, A. Misra, M. Richard, and K. Sil, “Bulk Viscosity at Extreme Limits: From Kinetic Theory to Strings,” *JHEP*, vol. 07, p. 145, 2019.
- [247] L. V. Bravina *et al.*, “Microscopic models and effective equation of state in nuclear collisions at FAIR energies,” *Phys. Rev.*, vol. C78, p. 014907, 2008.
- [248] J. Hammelmann, J. M. Torres-Rincon, J.-B. Rose, M. Greif, and H. Elfner, “Electrical conductivity and relaxation via colored noise in a hadronic gas,” *Phys. Rev.*, vol. D99, no. 7, p. 076015, 2019.
- [249] M. Greif, J. A. Fotakis, G. S. Denicol, and C. Greiner, “Diffusion of conserved charges in relativistic heavy ion collisions,” *Phys. Rev. Lett.*, vol. 120, no. 24, p. 242301, 2018.
- [250] R. Baier and Y. Mehtar-Tani, “Jet quenching and broadening: The Transport coefficient q -hat in an anisotropic plasma,” *Phys. Rev.*, vol. C78, p. 064906, 2008.
- [251] H. Petersen, J. Steinheimer, Q. Li, G. Bureau, and M. Bleicher, “A Fully integrated Boltzmann + hydrodynamics approach: Multiplicities, transverse dynamics and HBT,” in *24th Winter Workshop on Nuclear Dynamics (WWND 2008) South Padre Island, Texas, April 5-12, 2008*, 2008.
- [252] Y. Tachibana, N.-B. Chang, and G.-Y. Qin, “Full jet in quark-gluon plasma with hydrodynamic medium response,” *Phys. Rev.*, vol. C95, no. 4, p. 044909, 2017.
- [253] R. Kunnawalkam Elayavalli and K. C. Zapp, “Medium response in JEWEL and its impact on jet shape observables in heavy ion collisions,” *JHEP*, vol. 07, p. 141, 2017.
- [254] C. Park, S. Jeon, and C. Gale, “Jet modification with medium recoil in quark-gluon plasma,” *Nucl. Phys.*, vol. A982, pp. 643–646, 2019.
- [255] Y. Tachibana *et al.*, “Jet substructure modifications in a QGP from multi-scale description of jet evolution with JETSCAPE,” *PoS*, vol. HardProbes2018, p. 099, 2018.

Acknowledgements

As I am coming to the end of this thesis and hopefully shortly to that of my doctoral studies, my thoughts go to many people who helped me undertake this project and supported me in one way or the other during its realization.

The first of these is without a doubt my supervisor Hannah, who still gave me a chance and invited me to Frankfurt five years ago after seeing a CV which essentially told her how good a sailing coach I would be. Thanks for all our talks, physics-related or not, all the support through the years, and first of all for the opportunity to pursue research in a new city, a new country and even a new continent.

Second are all the people with which I interacted and collaborated in the various projects that culminated in this thesis. In no particular order, here it goes. Thanks to Juan for all the discussions, the Chapman-Enskog calculations and for helping plough through the differences between the microscopic treatments of our models; to Marcus, for sitting on my PhD committee, agreeing to read this fine 150-page prose and answering many AQM and UrQMD questions throughout the years; to Moritz and Gabriel for always supplying two new ideas for my to-do list whenever I was going to finish the previous one; to Charles and Sangyong for welcoming me twice into their group in McGill. Thanks also to all the Smashies, present and past, who helped create such a positive, productive and welcoming working group atmosphere, with a special thought to my proofreaders Philip, Anna, Jan, Justin and Oscar.

Last but not least come all the people I met outside of the scientific world, with whom I spent much of my free time and who made my time in Frankfurt special. My thoughts go here first to Bettina, for supporting me all the way through my writing reclusion, and reminding me to have fun once in a while (or maybe twice); to Theresa, for all the climbing Mondays (auf Deutsch!), and introducing me to many of the others; to Imi, Nessa, Salvi, Lotti, Jonas, Olga, Chris, Jamie, to my favourite couchsurfer Pierre, as well as all the rest for the memorable Apfelwein nights, BBQs and other dinners, boardgame evenings and parties (also the ones that I don't remember quite so well); to my roommates Tom, Felix, Puschmann and Moritz for taking me into their homes and introducing me to a whole other bunch of their own friends. And finally, thanks to all the karaoke bars in Frankfurt for being there when we needed them, which was a bit more often than I'm ready to admit.

Jean-Bernard Rose

rose@fias.uni-frankfurt.de
Born on 29/08/1988 in Montreal, Canada

Summary

- Master of Science, Physics (McGill University, Montréal)
- Certificate in higher education teaching (UQAM, Montréal)
- Strong computing and coding skills (C++, Python, Redmine, Github, Fortran)
- Fluent in French and English, intermediate German, basic Spanish

Education History

- **B. Sc Physics** 2008 – 2011
Laval University, Quebec City (Canada); average of A-
- **Certificate in higher education pedagogy** 2011 – 2012
University of Québec in Montreal, Montreal (Québec)
- **M. Sc Physics** 2012 – 2015
Supervisor : Charles Gale, McGill University, Montreal (Canada)
Fluid-dynamical modelling of heavy ion collisions. Thesis title: Extracting Shear and Bulk Viscosity from Ultra-Central Pb-Pb Collision at the LHC, excellent mention
- **Ph.D. Physics** 2015 –
Supervisor : Hannah Elfner, Goethe University, Frankfurt am Main (Germany)
Hadron gas modelling of heavy ion collisions for transport properties extraction.
Expected thesis title: Transport coefficients in the hadron gas; finishing in 2019
Member of the SMASH transport approach development team

Teaching Experience

- **Teaching Assistant**
 - McGill University, Montreal (Canada) 2012 – 2014
Grading and tutorials for “Modern physics and relativity” (1 semester)
Grading and laboratory supervision “Experimental Methods 1&2” (3 semesters)
 - Goethe University, Frankfurt am Main (Germany) 2016 – 2018
Tutorials for “Theoretical nuclear and particle physics 1&2” (3 semesters)
- **Bachelor student co-supervision** 2016 – 2018
 - Goethe University, Frankfurt am Main (Germany)
Co-supervision of 2 bachelor theses and one summer exchange student

Publication List

- J.-B. Rose, J.-F. Paquet, G. S. Denicol, M. Luzum, B. Schenke, S. Jeon, C. Gale, *Extracting the bulk viscosity of the quark-gluon plasma*, Nucl. Phys. A931 (2014) 926-930

- J. Tindall, J. M. Torres-Rincon, J.-B. Rose H. Petersen, *Equilibration and freeze-out of an expanding gas in a transport approach in a Friedmann-Robertson-Walker metric*, Phys. Lett. B770 (2017) 532-538
- J. M. Torres-Rincon, J. Aichelin, H. Petersen, J.-B. Rose, J. Tindall, *Melting and freeze-out conditions of hadrons in a thermal medium*, EPJ Web Conf. 17 (2018) 14007
- J.-B. Rose, J. M. Torres-Rincon, D. Oliinychenko, A. Schäfer, H. Petersen, *Systematic errors in transport calculations of shear viscosity using the Green-Kubo formalism*, J. Phys. Conf. Ser. 1024 (2018) no.1, 012028
- J.-B. Rose, J. M. Torres-Rincon, A. Schäfer, D. Oliinychenko, H. Petersen, *Shear viscosity of a hadron gas and influence of resonance lifetimes on relaxation time*, Phys. Rev. C97 (2018) no.5, 055204
- J. Hammelmann, J. M. Torres-Rincon, J.-B. Rose, M. Greif, H. Elfner, *Electrical conductivity and relaxation via colored noise in a hadronic gas*, Phys.Rev. D99 (2019) no.7, 076015
- J.-B. Rose, J. M. Torres-Rincon, A. Schäfer, D. R. Oliinychenko, H. Petersen, *Shear viscosity and resonance lifetimes in the hadron gas*, Nucl. Phys. A982 (2019) 807-810
- Philipp Dorau, Jean-Bernard Rose, Daniel Pablos, Hannah Elfner. *Jet quenching in the hadron gas: an exploratory study*, e-Print: arXiv:1910.07027 [nucl-th]

Conferences, workshops and lecture weeks

- **Doctoral training program for Heavy Ion Collisions** 2014
ECT*, Trento (Italy)
- **Hard Probes 2015** 2015
McGill University, Montréal (Québec)
- **Quark Matter 2017, contributed a poster** 2017
"Shear viscosity and entropy of a hadron gas"
Chicago (United States)
- **FAIRness 2017, contributed a plenary talk** 2017
"Shear viscosity and entropy of a hadron gas"
Sitges (Spain)
- **Quark Matter 2018, contributed a parallel talk** 2018
"Shear Viscosity and resonance lifetimes in the hadron gas"
Venice (Italy)
- **CPOD 2018, contributed a plenary talk** 2018
"Shear Viscosity and resonance lifetimes in the hadron gas"
Corfu (Greece)
- **"Matter and the Universe" Symposium, contributed a poster** 2019
"Transport coefficients of a hadron gas"
Hamburg (Germany)
- **Seminars : "Shear viscosity and resonance lifetimes in the hadron gas"**
McGill University, Montreal (Canada) 2017
HotLHC Seminar, Santiago de Compostela (Spain) 2017

CRC Transport Meeting, Frankfurt am Main (Germany) 2018

Awards

- Giersch Excellence Grant for outstanding scientific work from Giersch Stiftung, HGS-HiRe 2017

Professional Engagement and Memberships

- Student representative for physics, Laval University 2009 – 2011
- Organizing committee of the Physics Games in McGill University 2014 – 2015
- Helmholtz Graduate School for Hadron and Ion Research 2015 –
- Student representative in Frankfurt Institute for Advanced Studies 2016 – 2018
- German Association of Physicists (DPG) 2016 –

Interests

- Improvisation theater (both playing and watching)
- Video games (strategy; both playing and developing)
- Sailing (instructor and racing coach from 2004-2012)
- Reading: novels, newspapers
- Traveling

Jean-Bernard Rose
23/10/2019

